THE EFFECTS OF SURFACE ROUGHNESS ON STAGNATION-POINT HEAT TRANSFER DURING IMPINGEMENT OF TURBULENT LIQUID JETS

by

LAURETTE A. GABOUR

S. B., Mechanical Engineering

Massachusetts Institute of Technology, 1991

Submitted to the Department of Mechanical Engineering

in Partial Fulfillment of the Requirements for the Degree of

MASTER OF SCIENCE IN MECHANICAL ENGINEERING

at the

Massachusetts Institute of Technology

February 1993

Signature of Author_____

Department of Mechanical Engineering

January 15, 1993

Certified by_____

John H. Lienhard V

Associate Professor of Mechanical Engineering

Thesis Supervisor

Accepted by_____

Ain A. Sonin

Chairman, Department Committee

THE EFFECTS OF SURFACE ROUGHNESS ON

STAGNATION-POINT HEAT TRANSFER DURING

IMPINGEMENT OF TURBULENT LIQUID JETS

by

LAURETTE A. GABOUR

Submitted to the Department of Mechanical Engineering
on January 15, 1993 in partial fulfillment of the
requirements for the degree of
Master of Science in Mechanical Engineering

ABSTRACT

Jet impingement cooling applications often involve rough surfaces, yet few studies have examined the role of wall roughness. Surface protrusions can pierce the thermal sublayer in the stagnation region and increase the heat transfer. Here, the effect of surface roughness on the stagnation-point heat transfer of an impinging unsubmerged liquid jet is investigated. Experiments were performed in which a fully-developed turbulent water jet struck a uniformly heated rough surface. Heat transfer measurements were made for jets of diameters 4.4 - 9.0 mm over a Reynolds number range of 20,000 - 84,000. Results are presented for nine well-characterized rough surfaces with root-mean-square average roughness heights ranging from 4.7 - 28.2 microns. Measured values of the local Nusselt number for the rough plates are compared with those for a smooth wall and increases as high as 50 percent are obtained. Heat transfer in the stagnation zone is scaled with Reynolds number and a roughness parameter. For a given roughness height and jet diameter, the minimum Reynolds number required to increase heat transfer above that of a smooth plate is established. The effect of nozzle-to-target spacing is also investigated.

Thesis Supervisor: John H. Lienhard V

Title: Associate Professor of Mechanical Engineering

ACKNOWLEDGEMENTS

I am extremely grateful to the many people who have offered their support, encouragement, and advice throughout this work, without whom none of this would have been possible.

First and foremost I would like to express my deepest thanks, appreciation, and respect to my advisor, John H. Lienhard V, for his tremendous insight, patience, and invaluable advice. Most importantly, I am indebted to him for sparking my interest once again in research by showing me how enjoyable and rewarding it can be, despite the frustrations.

Thanks to Tiny Caloggero, Norm Mac Askill, and Bob Nuttall in the machine shop for solving my endless problems and helping with my extreme lack of machining skills. I don't know what I would have done without them. I also appreciate the help from Bob Samuel and I thank him for providing me with many enjoyable breaks from my research.

I am especially grateful to Tony DiCristiforo at Industrial Equipment for the use of the DEKTAK, as well as to Richard Perilli and Tim Mc Clure in the Microelectronics Lab for their help and advice on the surface measurements.

Thanks are due to my friends in the Heat Transfer Lab for making my time here pass more quickly. I would also like to express my appreciation to my former officemate, Dr. Xin Liu, for his helpful suggestions during the initial stages of this work.

A special thank you goes to my parents for their love, support, and encouragement. Words can not express how much I appreciate all that they have done for me.

This work was supported by the National Science Foundation under grant No. CBT-8858288 and the A. P. Sloan Foundation. The material is based upon work supported under a National Science Foundation Graduate Research Fellowship.

TABLE OF CONTENTS

NOMENCLATURE

Roman Letters

B radial velocity gradient, $2\partial U / \partial r$

B^* dimensionless radial velocity gradient, $2\left(d_j / u_f\right)\left(\partial U / \partial r\right)$

C_f skin friction coefficient

c_p heat capacity

d nozzle or pipe inner diameter

d_j jet diameter

f friction factor

g gravitational body force

gh_L Bernoulli energy loss

H distance between top of plenum and nozzle outlet

h heat transfer coefficient

I current supplied by generator

K loss coefficient

K_a acceleration parameter

k roughness element height

k^+ roughness Reynolds number, $k_s u^* / \nu$

k^* nondimensional roughness height, k / d_j

k_f thermal conductivity of the impinging liquid

k_s sand grain roughness size

k_w thermal conductivity of the heater material

L length of nozzle

l distance between nozzle outlet and target plate

l_h heated length of heater sheet

l_o nozzle-to-target separation for onset of splattering

l_v viscous length scale

Nu_d Nusselt number based on jet diameter, $q_w d_j / k_f (T_w - T_f)$

Nu_m measured Nusselt number based on temperature at back of heater, $q_w d_j / k_f (T_m - T_f)$

Pr Prandtl number

Pr_t turbulent Prandtl number

p_g gauge pressure

Q volume flow rate of jet

Q_b measured flow rate of jet used to calibrate rotameters

Q_m flow rate of jet as read on rotameters

q_w wall heat flux

R resistance of heater sheet

R_f friction Reynolds number, $\sqrt{f}\mathrm{Re}_d$

Re_d Reynolds number of jet, $u_f d_j / \nu$

r radial coordinate

St Stanton number

St_h sublayer Stanton number

T_{PRT} platinum resistance thermometer temperature

T_{TC} thermocouple temperature

T_{TH} mercury-in-glass thermometer temperature

T_f incoming jet temperature

T_{film} film temperature, $(T_f + T_w)/2$

T_m measured temperature at back of heater

T_w wall temperature

t heater sheet thickness

U radial velocity just outside boundary layer

u^* friction velocity, $\sqrt{\tau_w / \rho}$

u_f bulk velocity of impinging jet, $4Q / \pi d_j^2$

u_h^+ roughness function

w_h width of heater sheet

We_d jet Weber number, $\rho u_f^2 d_j / \sigma$

x thermocouple voltage

z distance normal to the wall

Greek Letters

δ_t thermal boundary layer thickness

δ_v viscous boundary layer thickness

μ dynamic viscosity

ν kinematic viscosity, μ / ρ

ρ liquid density

σ surface tension

τ_w shear stress at wall

ω dimensionless group used to scale jet splatter, $\mathrm{We}_d \exp\left(0.971 / \sqrt{\mathrm{We}_d} \cdot l / d\right)$

ζ heater sheet conduction correction factor relating Biot number to Nusselt number, $t k_f / k_w d_j$

LIST OF FIGURES

LIST OF TABLES

CHAPTER 1

INTRODUCTION

Liquid jet impingement is an attractive method for cooling surfaces owing to its high heat transfer coefficients. Among its numerous industrial applications are the hardening and quenching of metals, tempering of glass, and cooling of turbine blades and electronic components. Surface roughness of these materials can play a significant role in the heat transfer, and thus should not be neglected. Hot rolled steel has an average roughness height of 12.5 - 25 μm, (Kalpakjian, 1985) while turbine blades can have roughness protrusions ranging from 1.5 - 11 μm (Taylor, 1989). Wall roughness on the order of only a few microns in height, such as those mentioned, can significantly increase the heat transfer by disrupting the thin thermal boundary layer at the stagnation point. Numerous investigations of the fluid flow and heat transfer beneath an impinging jet can be found in the literature, yet the effect of wall roughness has received little or no attention.

1.1 PREVIOUS ROUGHNESS STUDIES

The first experimental investigation of the effects of surface roughness on fluid flow was that of Nikuradse (1933), who measured pressure drop and velocity profiles for water flowing in pipes roughened by sand grains. He defined three regimes of fully developed flow in terms of a roughness Reynolds number:

hydrodynamically smooth, transitionally rough, and fully rough. The roughness Reynolds number is defined as a dimensionless roughness height, k^+:

$$k^+ = \frac{u^* k_s}{\nu} \tag{1}$$

where u^* is the friction velocity, k_s is the size of the sand grains, and ν is the kinematic viscosity. In the hydrodynamically smooth region, the roughness elements lie within the viscous sublayer and the surface behaves as if it were smooth, with the friction factor only dependent on the Reynolds number. In the transitionally rough region, the roughness elements protrude through the sublayer and the friction factor depends on both the roughness and the Reynolds number. Fully rough flow occurs when the roughness elements protrude into the turbulent core, essentially destroying the viscous sublayer, and the friction factor depends only on the roughness, independent of the Reynolds number. The limits of these regimes are defined by:

Hydrodynamically smooth:	$k^+ < 5$
Transitionally rough:	$5 < k^+ < 70$
Fully rough:	$k^+ > 70$

Based on Nikuradse's work, Schlichting (1936) introduced an equivalent sand grain roughness defined as the 'Nikuradse' sand grain size producing the measured friction factor at a given Reynolds number in the fully rough regime. He determined this value for a

variety of surfaces by conducting experiments on fully developed flow in a channel with a well-defined rough upper wall. He specifically investigated the effects of roughness shape, height, and density.

Numerous studies of heat transfer in rough pipes, channels, and boundary layers have been carried out, but only a few investigations will be touched upon here. Experimental investigations on the heat transfer characteristics of rough surfaces began with the pipe flow experiments of Cope (1941) and Nunner (1956). Dipprey and Sabersky (1963) studied the heat transfer and friction characteristics of distilled water flowing in rough tubes at various Prandtl numbers. They conducted experiments on one smooth and three rough pipes with three dimensional roughness elements resembling closely-packed sand grains. Roughness-induced increases in the heat transfer coefficient of up to 270% were reported. Studies conducted at Stanford by Healzer (1974), Pimenta (1975), Coleman (1976), and Ligrani (1979) concentrated on air flow over a single rough surface consisting of hemispheres in a staggered, dense array. Their main focus was on heat transfer in the transitionally rough and fully rough turbulent boundary layer. Hosni, Coleman, and Taylor (1990) also investigated boundary layer heat transfer in the transitionally rough and fully rough regimes. They presented Stanton number and skin friction coefficients for air flow over one smooth and three rough surfaces composed of hemispheres in a staggered array.

In another context, Taylor (1989) reported that the turbine blades on the Space Shuttle Main Engine have an RMS roughness of 15μm,

which causes the Stanton number to double over that for the smooth case where the boundary layer thickness is about 0.5 mm.

Literature on impingement heat transfer to rough surfaces is almost nonexistent. The first known study is that of Trabold and Obot (1987) who examined the effects of crossflow on impingement heat transfer of multiple air jets to rough surfaces composed of repeated ribs. They found that roughness elements had an adverse effect on the heat transfer coefficient with intermediate crossflow, but for maximum crossflow they noticed an improvement in the downstream section, dependent on the open area and jet to target spacing. More recently, Sullivan, Ramadhyani, and Incropera (1992) investigated the use of extended surfaces to augment heat transfer for the cooling of electronic chips. Submerged FC-77 jets of various diameters were used to cool one smooth and two roughened spreader plates attached to simulated electronic circuit chips under the full range of hydrodynamically smooth to fully rough conditions. Since the local heat transfer coefficient varies along the impingement plate, often exhibiting a secondary peak downstream which fell outside the range of the unaugmented surface for the larger diameter jets, smooth spreader plates that were large enough to encompass this peak increased the heat transfer. However, since the spreader plates were 2mm thick, there is some ambiguity as to the true value for the local heat transfer coefficient. A unit thermal resistance, which accounted for conduction through the plate as well as convection at the surface, was shown to decrease by as much as 50% for the smooth plates and 80% for the roughened plates. For the rough surfaces, heat transfer enhancement increased with increasing

jet diameter, which led to their conclusion that Reynolds number, as opposed to the flow rate, was the parameter that had the strongest influence on heat transfer, with the resistance data for all nozzles nearly collapsing when plotted as a function of Reynolds number for a given surface (Sullivan, 1991).

The shape, height, and spacing of roughness elements can influence the effectiveness of the roughness. Gowen and Smith (1968) examined the friction factor and Stanton number in eight tubes with different roughness shapes. Roughness was produced by gluing or soldering a wire mesh, a screen, and copper balls to the surface. In the fully rough regime, increases in the friction factor as large as 355% over that of a smooth plate were obtained, while differences as large as 106% were noticed between the different roughnesses. For ethylene glycol at Pr = 14.3, increases in the Stanton number reached a maximum of 100% over that for a smooth wall, while differences of up to 61% were obtained between the rough tubes. A study by Scaggs, Taylor, and Coleman (1988) concentrated on the effects of roughness size, spacing, and shape on the friction factor. They investigated nine uniformly rough surfaces made up of large hemispherical, small hemispherical, and conical roughness elements, each at three distinct element spacings. By comparing data for the large and small hemispherical elements at the same spacing, they found that doubling the size of the elements increased the friction factor by 150%. They also obtained the unexpected result that for the same roughness diameter to height ratio, the friction factors for the conical and large hemispherical

elements were essentially identical, with differences falling within the experimental uncertainty.

1.2 THEORETICAL BACKGROUND

Since most of these previous studies were concerned with roughness effects on friction factor and Stanton number, it is instructive to examine in more detail the effect of roughness on these variables. White (1974) gives the following relationship for the friction factor for turbulent pipe flow:

$$\frac{1}{\sqrt{f}} \approx 2.0 \log \frac{\mathrm{Re}_d \sqrt{f}}{1 + 0.1(k_s / d)\mathrm{Re}_d \sqrt{f}} - 0.8 \qquad (2)$$

where d is the pipe diameter. This expression shows the strong influence of k_s / d and is valid in the smooth, transitional, and fully rough regimes. For flow over a smooth wall the skin friction coefficient is defined as:

$$C_f = \frac{f}{4} = \frac{\tau_w}{\rho U^2 / 2} \qquad (3)$$

where τ_w is the wall shear stress, U is the radial velocity, and ρ is the liquid density.

White (1974) presents the following relationship for the stagnation-point wall shear stress:

$$\tau_w = 0.46384 \mu Br \sqrt{\frac{B}{\nu}} \qquad (4)$$

where μ is the dynamic viscosity, r is the radial coordinate, and $B = 2\partial U / \partial r$ is the radial velocity gradient.[1] This corresponds to a skin friction coefficient of:

$$C_f = 1.85536\sqrt{\frac{2\nu}{Ur}} \tag{5}$$

For turbulent flow over a smooth wall, the Stanton number is obtained from the law of the wall as:

$$\mathrm{St} = \frac{C_f / 2}{1.07 + 12.7(\mathrm{Pr}^{2/3} - 1)\sqrt{C_f / 2}} \tag{6}$$

The first term in the denominator is an outer layer thermal resistance, while the second is a sublayer resistance. For fully rough turbulent flow over a rough surface the expression becomes:

$$\mathrm{St} = \frac{C_f / 2}{\mathrm{Pr}_t + \sqrt{C_f / 2}\left[(1/\mathrm{St}_h) - \mathrm{Pr}_t u_h^+\right]} \tag{7}$$

where Pr_t is the turbulent Prandtl number, St_h is the sublayer Stanton number, and u_h^+ is a general roughness function determined for each roughness shape. The first term in the denominator is again an outer layer thermal resistance, while the second term resistance is

[1]Nakoryakov, Pokusaev, and Troyan (1978) left out the radial coordinate in this expression and present a dimensionally incorrect equation for the skin friction coefficient for turbulent flow at the stagnation point.

now controlled by the roughness. Taking $u_h^+ = 8.48$ for sand grains as obtained by Dipprey and Sabersky (1963) for the fully rough region, Wassel and Mills (1979) obtain the sublayer Stanton number as:

$$\mathrm{St}_h = \frac{1}{4.8} k^{+^{-0.2}} \mathrm{Pr}^{-0.44} \tag{8}$$

for $\mathrm{Pr}_t = 0.9$.

The present study concentrates on rough-wall stagnation-point heat transfer beneath an impinging turbulent liquid jet. Consequently, standard rough wall theory can not be applied directly. As previously mentioned, typical roughness scaling depends on the friction velocity, u^*, which is defined as

$$u^* = \sqrt{\frac{\tau_w}{\rho}} \tag{9}$$

Nakoryakov, Pokusaev, and Troyan (1978) made friction measurements beneath an impinging jet and found the wall shear stress in the stagnation zone to be linearly proportional to r, the radial distance from the point of jet impact, reaching a maximum at $2r/d_j \approx 1.6$ where d_j is the jet diameter. With the shear stress approaching zero at the stagnation point, the scaling in Equation (9) becomes ineffective. Since the stagnation zone flow field is characterized by the strain rate or the radial velocity gradient, $B = 2\partial U / \partial r$, we choose a viscous length scale:

$$l_v \sim \sqrt{\frac{\nu}{B}} \tag{10}$$

and new velocity scale:

$$u \sim \sqrt{\nu B} \tag{11}$$

to compensate for the zero shear stress. Taking $B = 1.832 u_f / d_j$ where u_f is the incoming jet velocity (Liu, Gabour, and Lienhard, 1992) and rewriting Equation (10):

$$l_v \approx \sqrt{\frac{\nu}{2\partial U / \partial r}} \approx \sqrt{\frac{d_j^2}{1.832}\left(\frac{\nu}{d_j u_f}\right)} \approx 0.739 d_j \mathrm{Re}_d^{-0.5} \approx \delta_v \tag{12}$$

we see that the new viscous length scale is proportional to a viscous boundary layer thickness.

Another difficulty with this scaling lies in the structure of the rough wall boundary layer. Roughness elements can pierce the sublayer and lower the thermal resistance, thereby increasing the heat transfer. However, there is no guarantee of a turbulent outer layer; the role of free stream turbulence may simply be to disturb this thin sublayer. If roughness destroys the sublayer, the fully rough flow condition may be solely dependent on the wall material and roughness size, shape, and spacing, as opposed to being limited by an outer layer mixing process.

Other deviations from rough wall turbulent boundary layer theory are a result of the highly accelerated flow near the stagnation point. A nondimensional acceleration parameter, K_a, is normally defined as:

$$K_a = \frac{\nu}{U^2}\left(\frac{dU}{dr}\right) \tag{13}$$

For an impinging jet it is instructive to rewrite this expression as:

$$K_a = \left(\frac{\nu}{u_f d_j}\right)\left(\frac{d_j}{r}\right)\left(\frac{2}{B^*}\right) \tag{14}$$

where B^* is the nondimensional velocity gradient:

$$B^* = 2\frac{d_j}{u_f}\frac{\partial U}{\partial r} \tag{15}$$

For $K_a \geq 3 \times 10^{-6}$ the boundary layer tends to relaminarize (Moffat and Kays, 1984). Taking B^*=1.832 (Liu et al., 1992), Equation (14) suggests that the boundary layer will remain laminar for $r/d_j \leq 0.25$ if $\mathrm{Re}_d \leq 5.8 \times 10^6$. While this is valid for flow over a smooth wall, the addition of roughness still does guarantee a disturbed boundary layer at the stagnation point, even for an incoming turbulent jet.

1.3 SMOOTH WALL JET IMPINGEMENT STUDIES

Many previous investigations have dealt with the fluid flow and heat transfer characteristics at the stagnation point of an impinging liquid jet, but just a few will be mentioned here. For a laminar jet,

Liu et al. (1992) present the following correlation for the stagnation-point Nusselt number:

$$\mathrm{Nu}_d = 0.745\mathrm{Re}_d^{1/2}\mathrm{Pr}^{1/3} \tag{16}$$

to an accuracy of ±5%. They also found theoretically that

$$\mathrm{Nu}_d \approx 0.601(\mathrm{Re}_d B^*)^{1/2}\mathrm{Pr}^{1/3} \tag{17}$$

for Pr ≥ 3.0. For a turbulent jet, Lienhard, Liu, and Gabour (1992) suggest the following relationship:

$$\mathrm{Nu}_d = 1.24\mathrm{Re}_d^{1/2}\mathrm{Pr}^{1/3} \tag{18}$$

which was obtained over a Reynolds number range of 20,000 - 62,000 and has an accuracy of ±10%. Based on data over a Reynolds number range of 4000 - 52,000, Stevens and Webb (1991) present a dimensional equation:

$$\mathrm{Nu}_d = 2.67\mathrm{Re}_d^{0.567}\mathrm{Pr}^{0.4}(l/d)^{-0.0336}(u_f/d)^{-0.237} \tag{19}$$

where l is the nozzle-to-target spacing. They also present the dimensionless relation:

$$\mathrm{Nu}_d = 1.51\mathrm{Re}_d^{0.44}\mathrm{Pr}^{0.4}\left(\frac{l}{d}\right)^{-0.11} \tag{20}$$

Equation (19) fit their data with an average error of 5% while Equation (20) had an average error of 15%. Pan, Stevens, and Webb (1992) give a correlation of

$$\mathrm{Nu_d} = 0.69\left(\mathrm{Re}_d \frac{B^*}{2}\right)^{0.5} \mathrm{Pr}^{0.4} \tag{21}$$

where they measured $B^*/2$ to be 1.5 for a fully-developed nozzle configuration with L/d = 30 and l/d = 1 where L is the length of the nozzle. This expression was only verified over a Reynolds number range of 16,600 - 43,700.

Stevens, Pan, and Webb (1992) present data for the turbulence level in jets issuing from four different types of nozzles at a single nozzle-to-target spacing of l/d = 1. However, with the exception of the fully-developed pipe nozzle, turbulence was most likely established by the plenum's turbulence, rather than the nozzle. For the fully-developed pipe nozzles they found an essentially constant turbulence level of 5% for $z/d > 0.15$ where z is the distance normal to the wall. This value is taken as the amount of turbulence encountered in the jets employed in this study.

Lienhard et al. (1992) and Bhunia and Lienhard (1992) present data on splattering of turbulent impinging liquid jets. They both find that the amount of splatter is governed by the magnitude of surface disturbances to the incoming jet. Lienhard et al. (1992) scale their splattering data for a Weber number range of 1000 - 5000 and nozzle to target separations of l/d = 7.6 - 26.4 with a nondimensional group, ω:

$$\omega = \mathrm{We}_d \exp\left(\frac{0.971}{\sqrt{\mathrm{We}_d}}\frac{l}{d}\right) \tag{22}$$

where We_d is the jet Weber number:

$$\mathrm{We}_d = \frac{\rho u_f^2 d_j}{\sigma} \tag{23}$$

with σ the surface tension. The condition presented for onset of splatter is $\omega > 2120$ or $\mathrm{We}_d < 2120$ for any nozzle-to-target spacing. Heat transfer at the stagnation zone was found to be essentially independent of ω. Bhunia and Lienhard (1992) present the following correlation for the onset of splatter for a Weber number range of 130 - 31,000 and nozzle-to-target separations of l/d = 3 - 125:

$$\frac{l_o}{d} = \frac{100}{1+4\times10^{-9}\mathrm{We}_d^{2.5}} \tag{24}$$

where onset is defined as the point at which 5% of the incoming liquid is splattered.

1.4 PRESENT FOCUS

This investigation is concerned with the fact that many surfaces which require impingement cooling are rough, while the existing heat transfer correlations apply to flat, smooth surfaces. Experiments were performed to characterize wall roughness effects on heat

transfer beneath a turbulent free liquid jet impinging normally against a flat, constant heat flux surface. Stagnation-point Nusselt numbers were measured for various Reynolds numbers, jet diameters, and wall roughnesses. As a baseline for comparison, smooth wall data were also taken under the same conditions. A correlation is given for the boundary between the hydrodynamically smooth and transitionally rough regimes. The effect of nozzle-to-target separation on Nusselt number was also investigated.

CHAPTER 2

EXPERIMENTAL APPARATUS AND PROCEDURES

Experiments were performed to determine the local Nusselt number at the stagnation point of an impinging turbulent liquid jet for a variety of jet diameters, Reynolds numbers, and wall roughnesses. The experimental apparatus is illustrated schematically in Figure 1 and consists of a flow loop and an electrically heated target plate. A fully-developed, turbulent water jet impinges vertically downward and strikes a uniformly heated, flat, rough surface on which heat transfer temperature measurements are made. With the exception of a few experiments on the effect of nozzle-to-target spacing, the spacing is held constant at l/d = 10.8.

The water supply is maintained at a constant level in a 55 gallon insulated drum. The temperature is allowed to reach a steady value before any measurements are made. Cold water between 12 - 16°C is used in an attempt to raise the heat transfer and lower the experimental uncertainty in the Nusselt number, as well as to create a narrow Prandtl number range of 8.2 - 9.1.

A high pressure pump, capable of delivering 40 gpm at 70 psi directs the water through either of two carefully calibrated rotameters which are connected in parallel. The liquid flow rate was varied from 1.55 - 10.1 gpm, allowing experiments in a Reynolds number range of 20,000 - 84,000 where the Reynolds number is defined by:

$$\mathrm{Re}_d = \frac{u_f d_j}{\nu} \tag{25}$$

The jet velocity, u_f, is determined from the flow rate, Q, as:

$$u_f = \frac{4Q}{\pi d_j^2} \tag{26}$$

The water then enters the top of the plenum, passes out of a nozzle attached at the bottom, and issues into still air. A 76.2 cm long PVC pipe with an inner diameter of 15.24 cm is sealed with plates at both ends and functions as the plenum. To dampen disturbances from the incoming flow, the plenum contains an inlet momentum breakup plate, as well as honeycomb flow straighteners (for full details see Vasista, 1989). A Bourdon-type pressure gauge is attached to the top plate of the plenum, while the bottom plate has an opening to attach interchangeable nozzles. Pressure at the top of the plenum is converted to pressure at the nozzle exit, from which the jet velocity is calculated, as described in Appendix A. A platinum resistance thermometer is located in the plenum and is used to determine the inlet water temperature, T_f.

The nozzles used to produce the liquid jets were made from tubes of diameters 4.4, 6.0, and 9.0 mm which were soldered to threaded caps for easy attachment to the plenum. The insides of the tubes were carefully deburred to create smooth inner walls (k/d = 0) so that the highly disturbed surfaces of the jets can be attributed exclusively to turbulence. The tubes are 70 - 110 diameters long in order to ensure fully-developed turbulent flow at the outlet.

Contraction of these turbulent jets is less than 1.5 percent, so the mean jet diameters can be approximated by the nozzle diameters. The tube diameters were measured with precision calipers and have estimated uncertainties of ±0.2%, ±0.7%, and ±0.5% for the 4.4, 6.0, and 9.0 mm nozzles, respectively.

The jet impinges normally onto an electric heater which consists of a 0.1016 mm thick 1010 steel shim stretched over an insulation box and clamped firmly between copper bars which serve as electrodes. Details of the heater are shown in Figure 2. The jet strikes a 3.81 cm wide by 7.62 cm long section of the heater. The steel shim is held under tension by springs at both ends to ensure a flat target surface, free from vibration or deflection. Compressed air is directed into the insulation box to keep the back of the heater free from water. The water that flows off the heater is collected in a plexiglass box and directed to a drain since it is warmer than that obtained directly from the faucet.

A 3.4 cm^2 central portion of the steel shim was roughened by scoring the surface in four directions, as shown in Figure 3(a), in an attempt to simulate natural roughness. The ease of fabricating these surfaces contributed to the choice of this type of roughness. The distance between roughness troughs is less than 1 mm in all cases. Nine rough surfaces with RMS roughness heights ranging from 4.7 - 28.2 μm and one smooth surface with an RMS roughness of 0.3 μm are used as the target plates. Roughness measurements are described below.

The leads from a low voltage, high current (15V, 1200 amp) generator are attached to the copper bus bars of the heater to

produce a voltage across the shim. Current supplied by the generator was determined from the voltage drop across a shunt (which gives a drop of 50 mV for 1200 amps). Knowledge of the power supplied to the heater, together with the effective heater area are used to calculate the heat flux. Currents as large as 415 amps were supplied to the heater, corresponding to a maximum heat flux of 130 kW/m^2. Heat dissipation to the copper bars could be neglected due to the thinness of the sheet and the low temperature differences encountered.

The wall temperature is measured by three 0.076 mm iron-constantan (type J) thermocouples, all located at the stagnation point for greater accuracy, as shown in Figure 3(b). The thermocouples were attached to the back of the steel shim and electrically isolated from it by 0.06 mm thick Kapton tape. Radiative loss and convective backloss by natural convection for the heater were estimated to be negligible. Since the convective backloss is so small due to the low temperatures involved, the temperature drop through the Kapton tape is negligible.

During the experiments, ten voltage readings were taken for each thermocouple and averaged to reduce random error. The average of the voltages from the three thermocouples was used to calculate the wall temperature. The thermocouples were also calibrated with the heater power off before and after each run to reduce systematic errors. The incoming jet temperature obtained by the thermocouples under isothermal conditions was in agreement with that obtained from the platinum resistance thermometer in the plenum to within the reading errors of the instruments, verifying that the bulk

temperature change of the jet as it travels from the plenum to the target is negligible.

The temperature measurements are used to calculate a measured Nusselt number as:

$$\mathrm{Nu}_m = \frac{q_w d_j}{k_f (T_m - T_f)} \tag{27}$$

where q_w is the heat flux, k_f is the thermal conductivity of water, T_m is the temperature measured at the back of the heater, and T_f is the inlet water temperature. Since the thermocouples are located on the back of the steel shim, the vertical conductive temperature drop through the sheet, $T_w - T_m = q_w t / 2k_w$, must be taken into account when determining the true Nusselt number. This correction is quite important at the stagnation zone since the heat transfer coefficient is so large. Liu, Lienhard and Lombara (1991) relate the measured Nusselt number to the true Nusselt number by:

$$\mathrm{Nu}_d = \frac{\mathrm{Nu}_m}{(1 - \zeta \mathrm{Nu}_m / 2)} \tag{28}$$

where ζ relates the Biot number to the true Nusselt number:

$$\zeta = \frac{t k_f}{k_w d_j} \tag{29}$$

where t is the thickness of the heater sheet and k_w is the thermal conductivity of the steel shim. In reducing the data, corrections as

large as 10% were applied.

All liquid properties are evaluated at the film temperature, $T_{film} = (T_f + T_w)/2$ and obtained from Touloukian (1970). Uncertainties were calculated by a procedure described in detail in Appendix B. Nusselt number uncertainty ranged from ±7.5% to ±10%, while Reynolds number uncertainty was ±5%.

2.1 CALIBRATION PROCEDURES

The two rotameters were calibrated by measuring the time required for a given volume of water to pass through the flow loop. The same test was repeated three times at each flow rate to reduce precision uncertainty. Calibration curves can be found in Appendix A. As another check, the pressure read from the gauge at the top of the plenum was used to calculate the jet's velocity and corresponding flow rate, as described in Appendix A. Uncertainty in the volumetric flow rate reached a maximum of ±3.2%, corresponding to a maximum uncertainty in the jet velocity of ±3.5%.

The three thermocouples and the platinum resistance thermometer were calibrated by comparison to a mercury-in-glass thermometer which could be accurately read to ±0.05°C. These devices were placed in water baths of various temperatures in a Dewar in order to create an environment with a constant temperature, free from room air currents. Ice point was used as a final reference. The platinum resistance thermometer could be accurately read to ±0.1°C, while thermocouple voltages could be read

to ±0.001 mV, corresponding to ±0.02°C. After calibration, the three devices agreed to within the reading errors of each instrument.

As a check on the heat flux measurements, leads were placed directly inside the copper bus bars to measure the voltage drop while varying the current from 200 - 415 amps for flow rates from 1.4 - 10.6 gpm for each of the ten heater sheets. To ensure that the contact resistance of the leads was negligible, the leads were moved to the opposite side of the sheet and the voltage measurements were compared, agreeing to within ±0.5%. From the voltage and current measurements, the resistance of the heater sheet was determined for each run. An average resistance of 2.25 mΩ was established for all of the sheets, while individual measurements differed from this value by less than ±0.5%. Using this resistance, heat flux is calculated from:

$$q_w = \frac{I^2 R}{l_h w_h} \tag{30}$$

where I is the current supplied by the generator, R is the resistance of the steel shim, l_h is the length of the heater, and w_h is the width of the heater. Uncertainty in the heat flux was an average of ±4.2%.

2.2 SURFACE CHARACTERIZATION

The nine rough surfaces were characterized by a root-mean-square average roughness as obtained from profiles of the surfaces. A DEKTAK 3030ST with a 2.5μm radius stylus was used to make the

measurements. The DEKTAK is a surface texture measuring system that makes measurements electromechanically by moving the sample in a straight line beneath a diamond-tipped stylus. The DEKTAK was carefully calibrated by scanning a standard 1 micron step and making the necessary adjustments to obtain the correct reading. A scan length of 10 mm and a stylus force of 30mg was used. Ten profiles were generated for each surface at intervals of 0.5 mm across the length of the sheet. An RMS roughness height was calculated for each profile based on an average of 50 roughness peaks and troughs, and the ten squared RMS values were averaged. Due to the finite radius of the stylus, the path traced as it scans the surface is smoother than the actual roughness of the surface. However, since the blade used to score the surfaces was triangular with a maximum width of 160μm, we believe that the stylus was able to accurately resolve the roughness heights. Care was taken during the experiments to ensure that the jets were centered over the area that was used for the surface profiles. The roughness measurements were repeated after the experiments were completed to ensure that the steel shims had not sufficiently rusted to cause changes in their roughnesses. A few representative plots are shown in Figures 4 - 5.

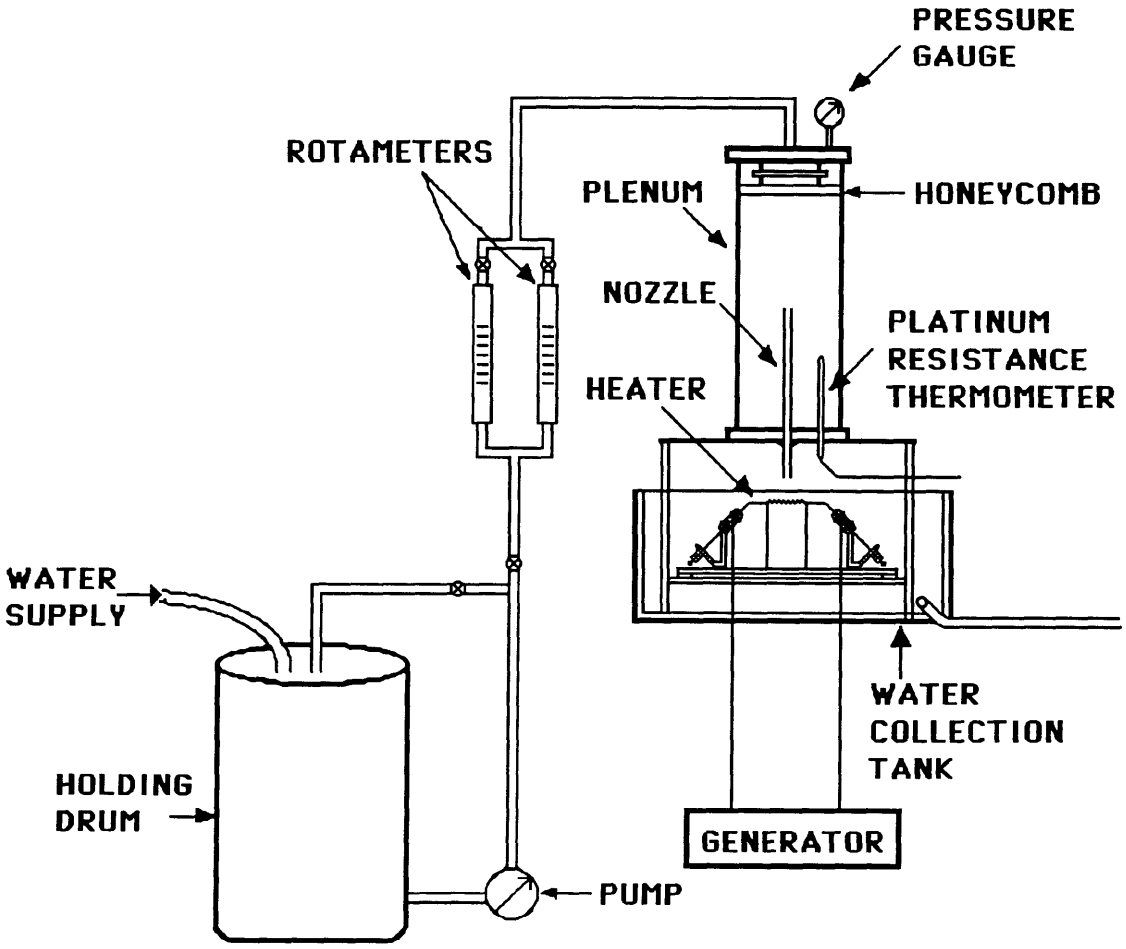

Figure 1: Experimental apparatus.

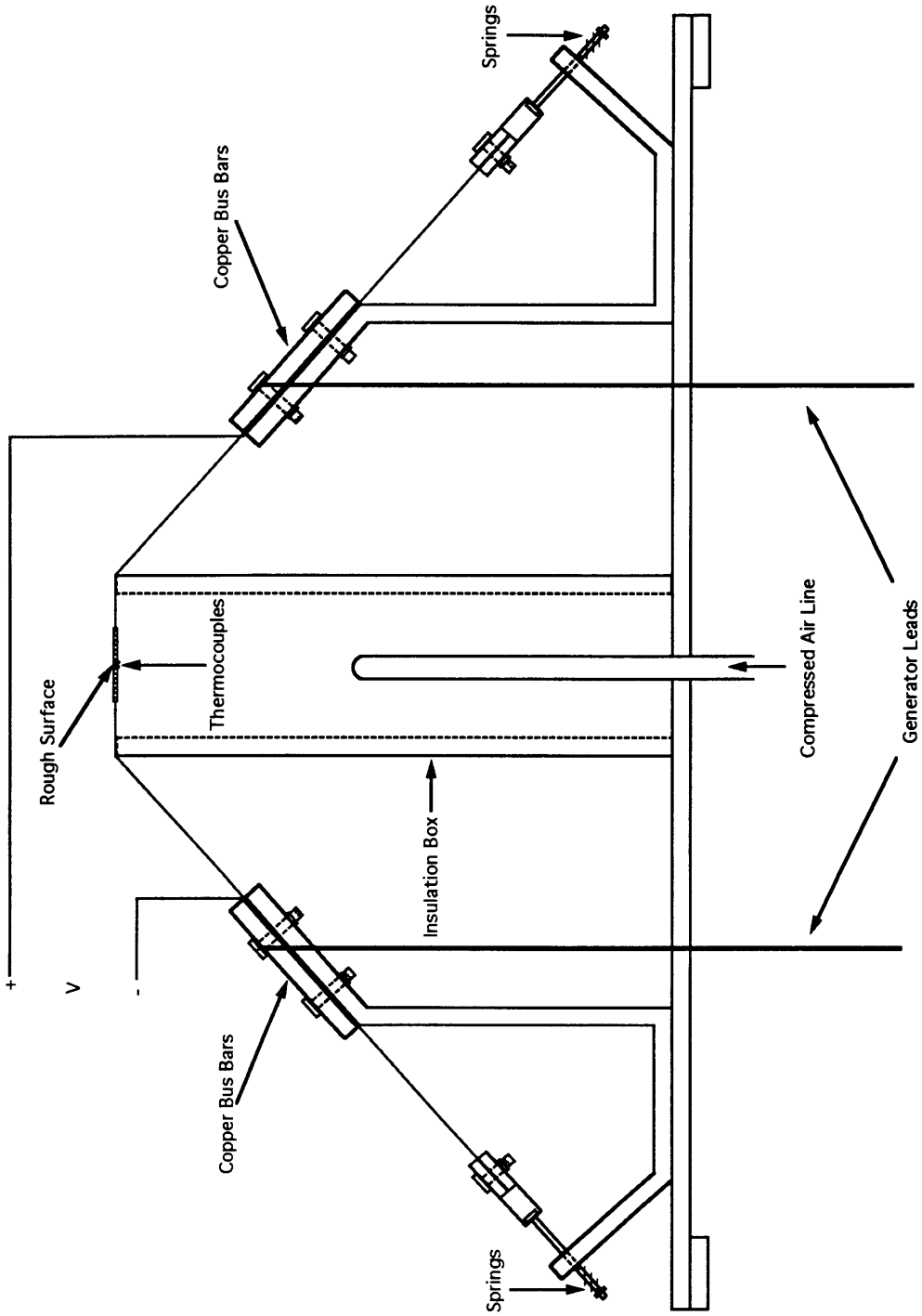

Figure 2: Schematic diagram of heater.

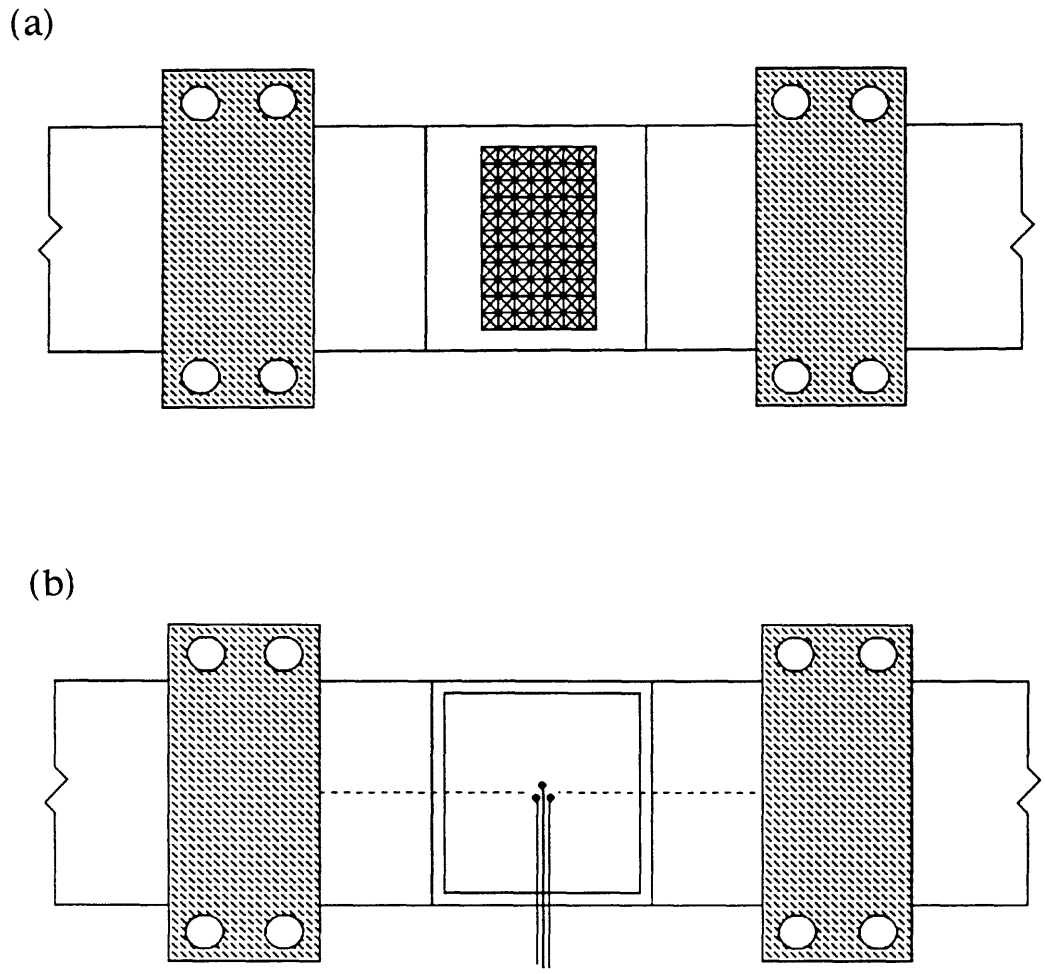

Figure 3: Heater surface: (a) Scoring pattern used to fabricate rough surfaces. (b) Thermocouple locations on the back of the heater sheet.

(a)

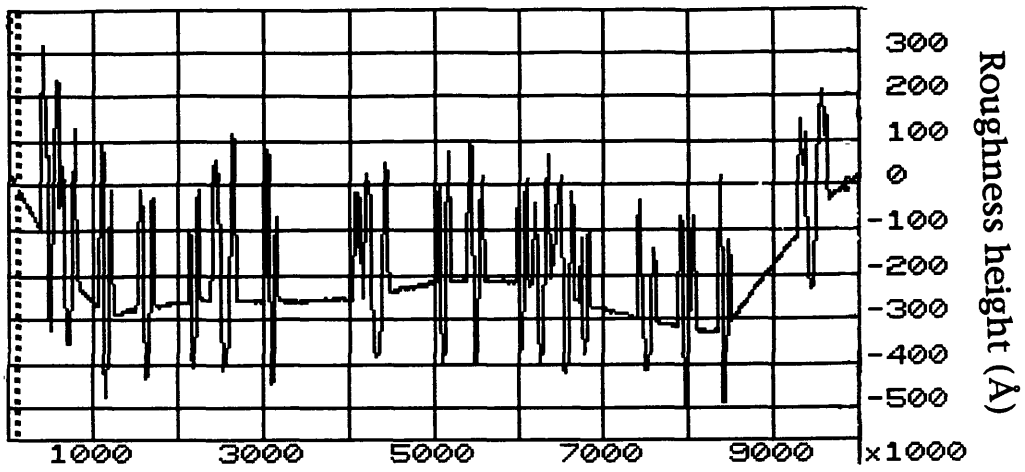

Distance along sheet (μm)

(b)

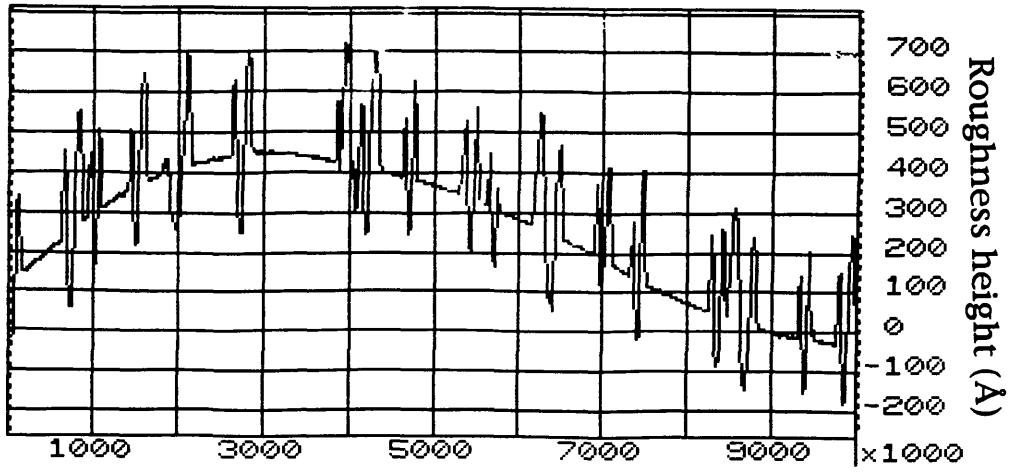

Distance along sheet (μm)

Figure 4: Surface profiles: (a) Surface S5, k = 13.1μm; (b) Surface S6, k = 14.1 μm.

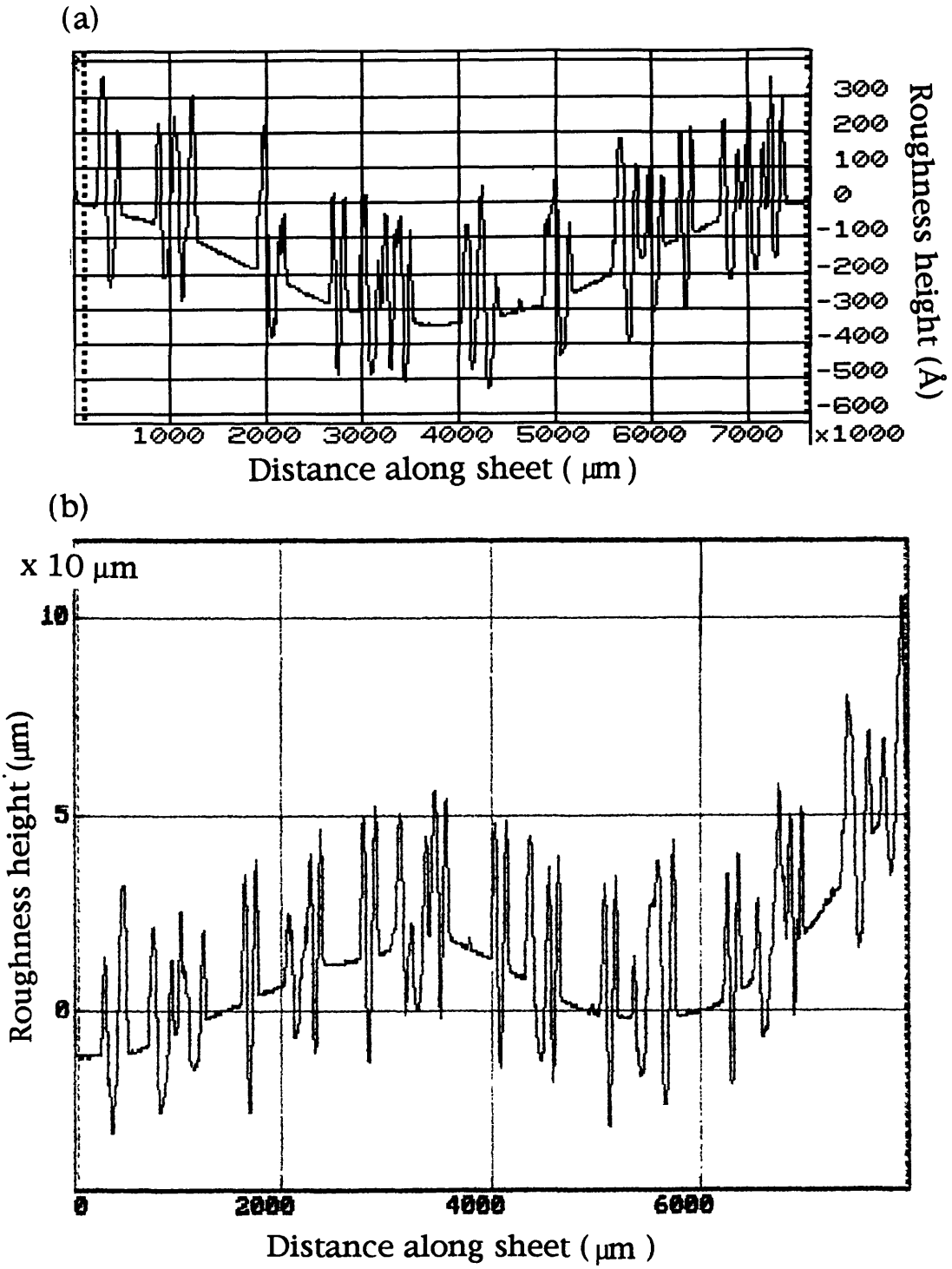

Figure 5: Surface profiles: (a) Surface S7, k = 20.1 μm; (b) Surface S8, k = 25.9μm (using a better printer).

CHAPTER 3

EXPERIMENTAL RESULTS

3.1 SMOOTH WALL RESULTS

The effect of nozzle-to-target spacing on the smooth wall stagnation-point Nusselt number is shown in Figure 6 for the 4.4 mm nozzle over an l/d range of 0.9 - 19.8. Over this range, the Nusselt number increases by 5% at a Reynolds number of 63,650, while it decreases by 8% at 27,300, and remains essentially constant at 48,250. However, these slight deviations fall within the uncertainty of the experimental data. Stevens et al. (1991) noticed a slight decrease in the stagnation-point Nusselt number with increasing nozzle-to-target spacing for low Reynolds numbers, as expressed in Equations (19) and (20). For a 4.1 mm nozzle they report a 12% decrease in the Nusselt number over essentially the same l/d range as employed in this study, but at a smaller Reynolds number of 10,600. However, since the Nusselt number was found to be essentially independent of l/d in this study, a single nozzle-to-target spacing of l/d = 10.8 was employed for the remainder of the experiments.

While splattering of these jets will not occur at the stagnation point, it is still interesting to examine the onset of splatter, which will lower the cooling efficiency of the jet further downstream. Using Bhunia and Lienhard's (1992) correlation for the onset of splatter (Equation (26)) , splattering will begin at l_o/d = 0.7, 2.6, and 31.1 for

the 4.4 mm diameter jet at Reynolds numbers of 63,650, 48,250, and 27,300, respectively. Based on this result, most of the data presented in Figure 6 for the higher Reynolds numbers are for splattering jets, while the lower Reynolds number data are for nonsplattering jets over the full l/d range investigated. For l/d = 10.8, splattering will begin at Reynolds numbers of 35,530, 41,490, and 50,815 for the 4.4, 6.0, and 9.0 mm diameter jets, respectively.

The smooth wall Nusselt number data for the three nozzles are plotted in Figure 7 and are well represented by:

$$\mathrm{Nu}_d = 0.278\mathrm{Re}_d^{0.633}\mathrm{Pr}^{1/3} \tag{31}$$

to an accuracy of about ±3%. While the Prandtl number was held constant at 8.3, the standard high Prandtl number exponent of 1/3 was adopted. Since the Reynolds number exponent is typically 1/2, the data can be fit by:

$$\mathrm{Nu}_d = 1.191\mathrm{Re}_d^{1/2}\mathrm{Pr}^{1/3} \tag{32}$$

to an accuracy of ±10% as shown in Figure 8. Figure 9 compares the 0.5 and 0.633 Reynolds number exponents by examining the slope on a log-log plot of Nusselt number vs. Reynolds number. While an exponent of 0.5 may work for Reynolds numbers less than 35,000, 0.633 clearly is the appropriate choice for the data. Since Equation (31) yields the best fit of the data, it will serve as the baseline for comparison to the rough wall results.

The present smooth wall correlation is compared to those of Lienhard et al. (1992) and Pan et al. (1992) in Figure 10 for a Prandtl number of 8.3, as used for all the smooth wall data in this study. The laminar jet prediction of Liu et al. (1992) is included for comparison. Lienhard et al.'s (1992) correlation was only verified over a Reynolds number range of 20,000 - 62,000; the present correlation differs by from it by a maximum of 20% at 20,000 and by only 3% at 62,000. Over Pan et al.'s (1992) narrower Reynolds number range of 16,600-43,700, the present correlation differs by 8% at 20,000, up to 20% at 43,700.

3.2 ROUGH WALL RESULTS

The RMS average roughness values for the ten surfaces are given in Table 1. For convenience the surfaces are labelled S1 - S10, with S1 being the smooth surface and S10 the roughest.

The Nusselt numbers for the ten surfaces are presented in Figures 11 - 13 as a function of jet Reynolds number for the 4.4, 6.0, and 9.0 mm diameter jets, respectively. Experimental values used to generate these plots can be found in Appendix C. As expected, the Nusselt number increases with increasing wall roughness for each diameter, with surface S10 producing the highest Nusselt number in all cases. The effect of roughness is clearly dependent on Reynolds number and jet diameter.

In general, the Nusselt number data for each surface tend to lie on distinct lines, with slope increasing as roughness increases, with the exception of surfaces S1, S2, and S3 in Figure 13. The data from the

latter surfaces lie on essentially the same line, implying that the roughnesses of S2 and S3 are ineffective for increasing heat transfer for the 9.0 mm nozzle. Apparently the roughness elements do not protrude through the thermal sublayer, causing the surfaces to behave as if they were smooth. At Reynolds numbers higher than examined for these surfaces, the transitionally rough regime may be reached, in which the roughness elements do pierce the sublayer, thereby causing the data to stray from this line.

SURFACE	RMS ROUGHNESS (μm)
S1	0.3
S2	4.7
S3	6.3
S4	8.6
S5	13.1
S6	14.1
S7	20.1
S8	25.9
S9	26.5
S10	28.2

Table 1: RMS average roughness heights for the ten heater surfaces. Uncertainties in the RMS roughness heights range from ±4.5 - ±9%

With the exception of surfaces S7 - S10 for the 4.4 mm nozzle, and surfaces S9 and S10 for the 6.0 mm nozzle, the Nusselt number data tend to collapse to the smooth wall curve at the lower Reynolds numbers. Presumably these few exceptions do collapse at a lower Reynolds number, but owing to the limited Reynolds number range employed in this study, this presumption can not be verified. Alternatively, these surfaces may have roughness elements that are greater in height than the thermal sublayer for all Reynolds numbers, thereby destroying the thermal sublayer and operating under fully rough conditions for all Reynolds number. However, this is not likely, as discussed below.

Differences between the smooth and rough wall data become more pronounced as jet diameter decreases, with results for the 4.4 mm nozzle in Figure 11 showing the largest roughness effects. For example, at a Reynolds number of 40,000 there is a 32% increase in the Nusselt number for S10 over S1 for the 4.4 mm nozzle, while at the same Reynolds number the increase is 27% and 14% for the 6.0 and 9.0 mm nozzles, respectively. At a Reynolds number of 66,000, the increases rise to 47%, 34%, and 23%, respectively. This effect can be explained by examining the thermal boundary layer thickness:

$$\delta_t \approx \frac{d_j}{\mathrm{Re}_d^{1/2}\mathrm{Pr}^{1/3}} \tag{33}$$

where the standard Reynolds number exponent of 1/2 is adopted. As jet diameter decreases, boundary layer thickness decreases.

Similarly, as Reynolds number increases, boundary layer thickness decreases. The heat transfer enhancement characteristics of a given roughness depend on how deeply the roughness elements protrude into the thermal sublayer. Thus, a thinner thermal boundary layer allows the roughness elements to protrude further, and increases their effect.

Figures 14 - 22 show the increase in the Nusselt number obtained by decreasing the jet diameter for each of the nine rough surfaces. The plots contain results for all three jet diameters and are presented in order of increasing roughness. As previously mentioned, for a given roughness height, the smaller diameter jets have a thinner thermal boundary layer and the roughness elements have a greater effect on the heat transfer, piercing deeper into the thermal sublayer. These differences in the Nusselt number for the different diameter jets become more pronounced as the roughness increases.

As discussed, heat transfer enhancement depends on the ratio of roughness height to thermal boundary layer height, k/δ_t. The measured thermal boundary layer height is determined from the smooth wall Nusselt number expression in Equation (31) by noting that $\mathrm{Nu}_d = d_j/\delta_t$, yielding:

$$\delta_t = \frac{3.60 d_j}{\mathrm{Re}_d^{0.633}\mathrm{Pr}^{1/3}} \tag{34}$$

Based on this thermal boundary layer height, k/δ_t ranges from 0.19 - 4.11 for this study. Since the roughness heights were never much

larger than the thermal boundary layer thickness, it is likely that fully rough conditions were not achieved.

The ratio between the rough wall and the smooth wall Nusselt number is plotted as a function of k/δ_t in Figures 23 - 25 for the 4.4, 6.0, and 9.0 mm nozzles, respectively. The data do not lie on the same curve for any diameter, and there is a distinct horizontal shift noticed between the diameters. As expected, this is not the correct scaling. Apparently roughness tends to displace the thermal boundary layer upward, creating an additional thermal resistance so that k/δ_t itself cannot scale the Nusselt number.

For the fixed wall material and roughness shape employed in this study, the dimensional equation for the heat transfer coefficient in the rough wall thermal boundary layer can be written as:

$$h = \mathrm{f}\left(k_f, d_j, \rho, c_p, \mu, u_f, k\right) \tag{35}$$

where c_p is the heat capacity. Dimensional analysis was performed, revealing four pi groups, from which we see:

$$\mathrm{Nu}_d = \mathrm{f}\left(\mathrm{Re}_d, \mathrm{Pr}, \frac{k}{d_j}\right) \tag{36}$$

where k/d_j is a roughness parameter we call k^*. Since the Prandtl number was held essentially constant in this study, we can focus on the two remaining parameters. The Nusselt number is plotted as a function of Reynolds number in Figures 26 - 37 for a given value of k^*. At a given Reynolds number, the Nusselt number is the same for

a given value of k^*, lending confidence that no other parameters are involved in the Nusselt number dependence. This also verifies that the nine rough surfaces are geometrically similar and differ from each other only by their roughness heights. Figures 38 - 40 compare the magnitude of the Nusselt number for a few values of k^*, while Figure 41 encompasses the full range of k^* investigated, with the individual data points left out for clarity. These figures clearly show that the Nusselt number increases with increasing values of k^*.

Figures 26 - 37 were compared to Figure 7 to determine the criterion for transition from hydrodynamically smooth to transitionally rough flow. Departure from smooth wall behavior was defined by the Reynolds number at which the rough wall Nusselt number became 10% larger than the corresponding smooth wall Nusselt number. Some of the constant k^* curves were extrapolated to lower Reynolds numbers to determine this value since they appeared to be in the transitionally rough regime for the entire Reynolds number range investigated. Figure 42 shows this transition Reynolds number as a function of k^*. Based on this figure, we estimate that the flow will remain in the hydrodynamically smooth regime for

$$\mathrm{Re}_d < 12.191 k^{*-1.402} \tag{37}$$

after which the flow may be considered transitionally rough.

Since the Prandtl number was held constant for the experiments, its role in the transition criterion is not clear from the data.

However, if we assume that Equation (37) is in the form of a k/δ_t threshold and $\delta_t \propto \mathrm{Pr}^{-1/3}$, we obtain:

$$k^* = \left(\frac{8.3}{\mathrm{Pr}}\right)^{1/3} k^*\Big|_{\mathrm{Pr}=8.3} \tag{38}$$

for other Prandtl numbers much greater than 1. This suggests that the flow will remain in the hydrodynamically (or at least thermally) smooth region for:

$$k^* \mathrm{Re}_d^{0.713} \mathrm{Pr}^{1/3} < 12.050 \tag{39}$$

Since the thermal boundary layer is so thin, if the flow is thermally smooth, it should also be hydrodynamically smooth. If we use the thermal boundary layer thickness obtained from our smooth wall correlation (Equation (34)) we can get a k/δ_t criterion for smooth wall behavior:

$$\frac{k}{\delta_t} < 3.35 \mathrm{Re}_d^{-0.08} \tag{40}$$

This corresponds to $k/\delta_t < 1.35$ - 1.52 for the Reynolds number range employed in this study. If instead we assume that Equation (37) is in the form of a k/δ_v threshold with $\delta_v = \delta_t \mathrm{Pr}^{1/3}$ we get:

$$\frac{k}{\delta_v} < 1.655 \mathrm{Re}_d^{-0.08} \tag{41}$$

which corresponds to k/δ_v < 0.67 - 0.75 for the present Reynolds number range. This is in contrast to the usual shear-layer sublayer result of

$$k^+ = \frac{k}{\delta_v} = \frac{u^* k}{\nu} < 5 \tag{42}$$

for smooth wall behavior. Differences between Equations (41) and (42) most likely lie in the definition of δ_v.

As a result of the limited scope of the data, an estimate for transition to fully rough conditions was not possible.

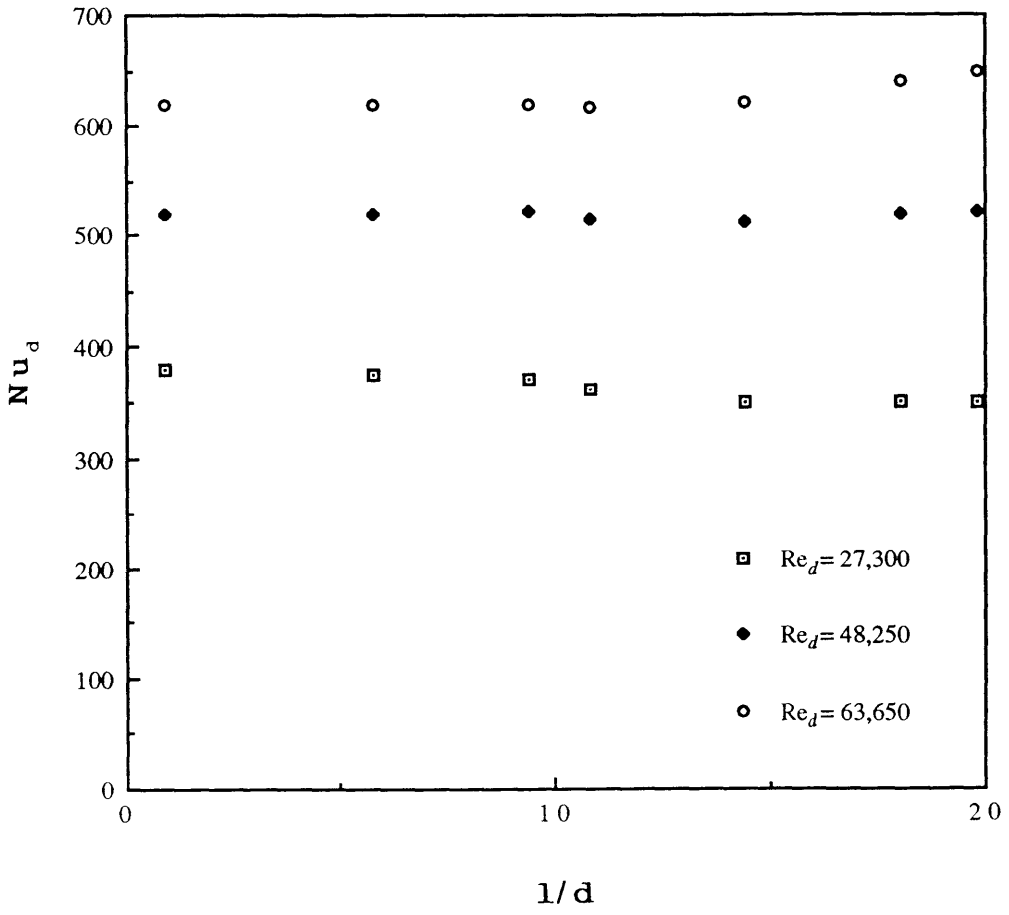

Figure 6: The effect of nozzle-to-target separation, l/d, on the stagnation-point Nusselt number.

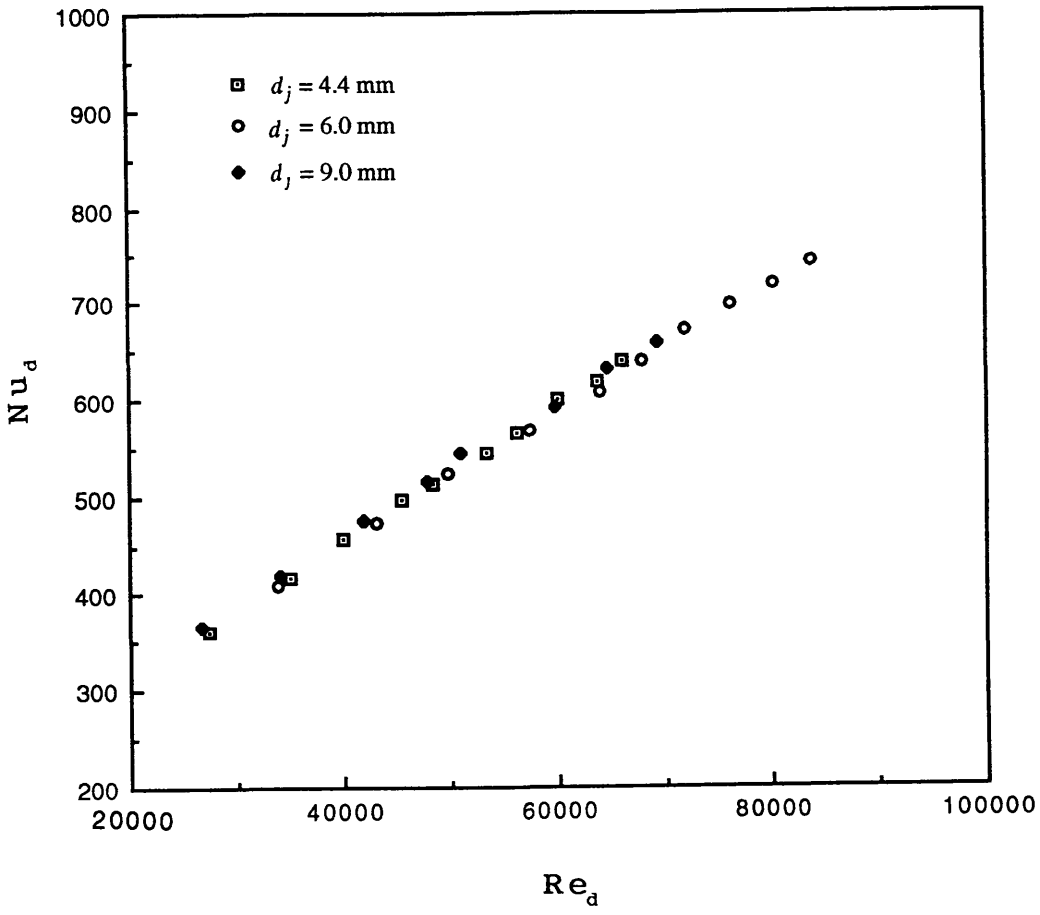

Figure 7: Smooth wall stagnation-point Nusselt number as a function of Reynolds number.

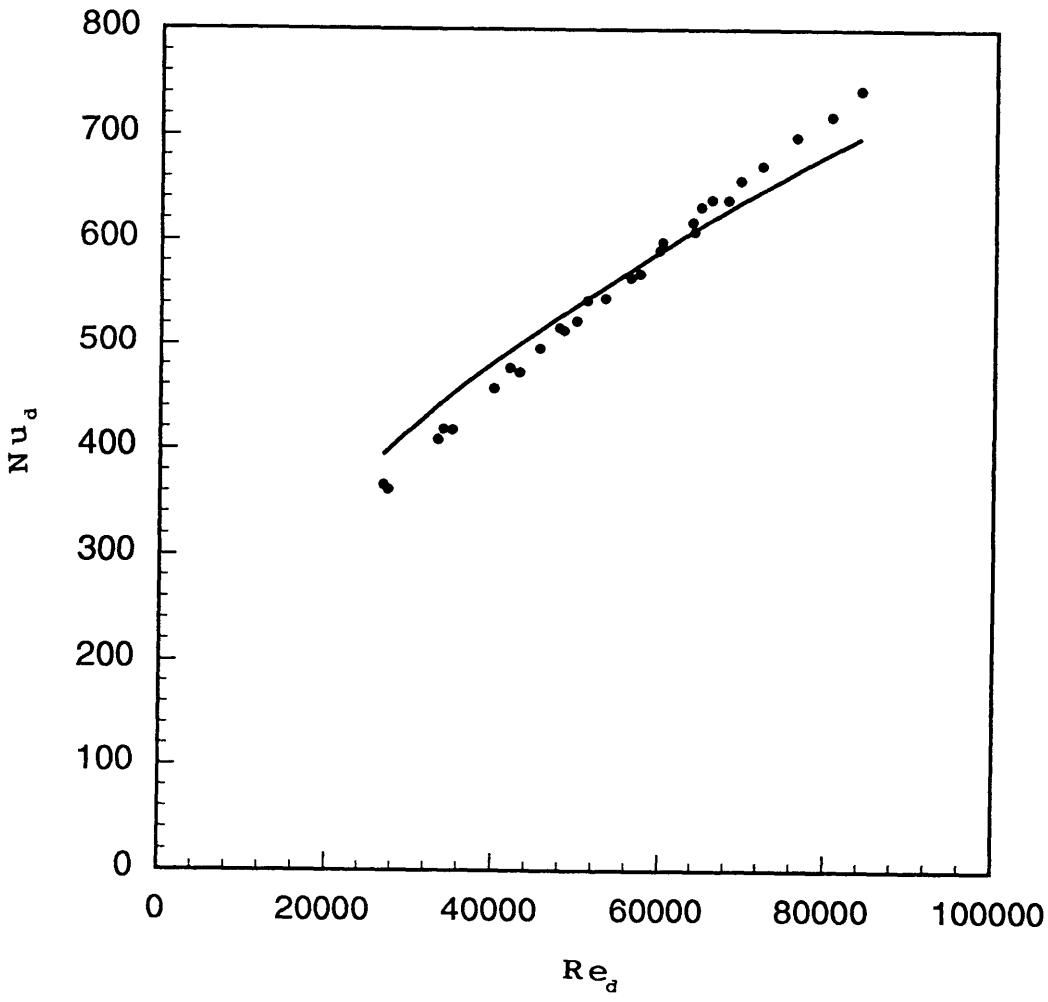

Figure 8: Best fit of smooth wall data using typical $Re_d^{1/2}$ scaling.

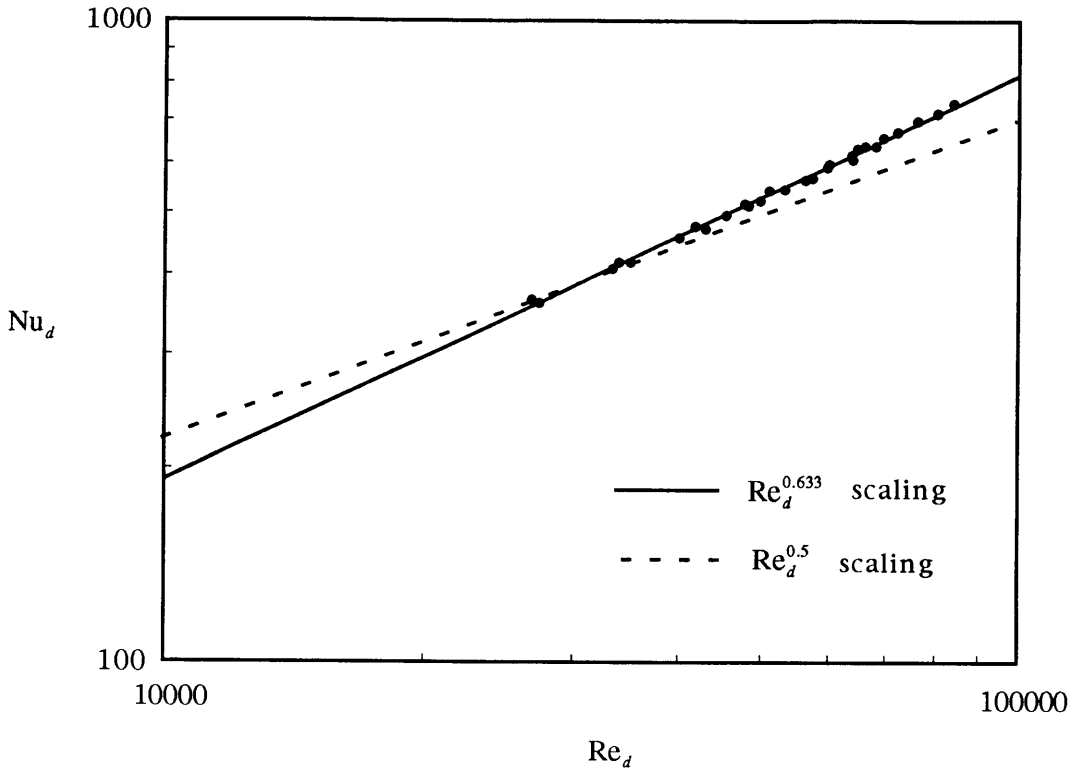

Figure 9: Comparison of smooth wall stagnation-point Nusselt number $Re_d^{0.633}$ and $Re_d^{0.5}$ scaling.

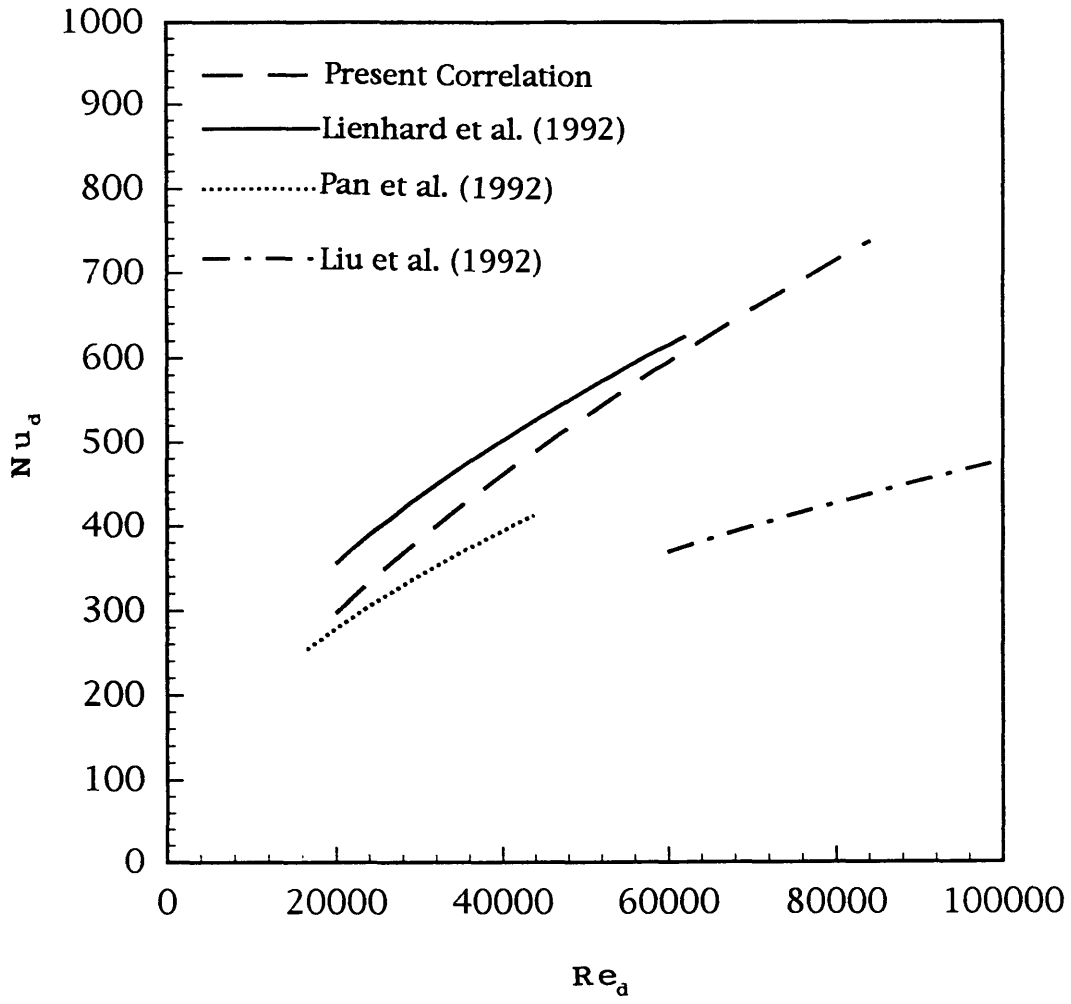

Figure 10: Comparison of smooth wall stagnation-point Nusselt number correlations.

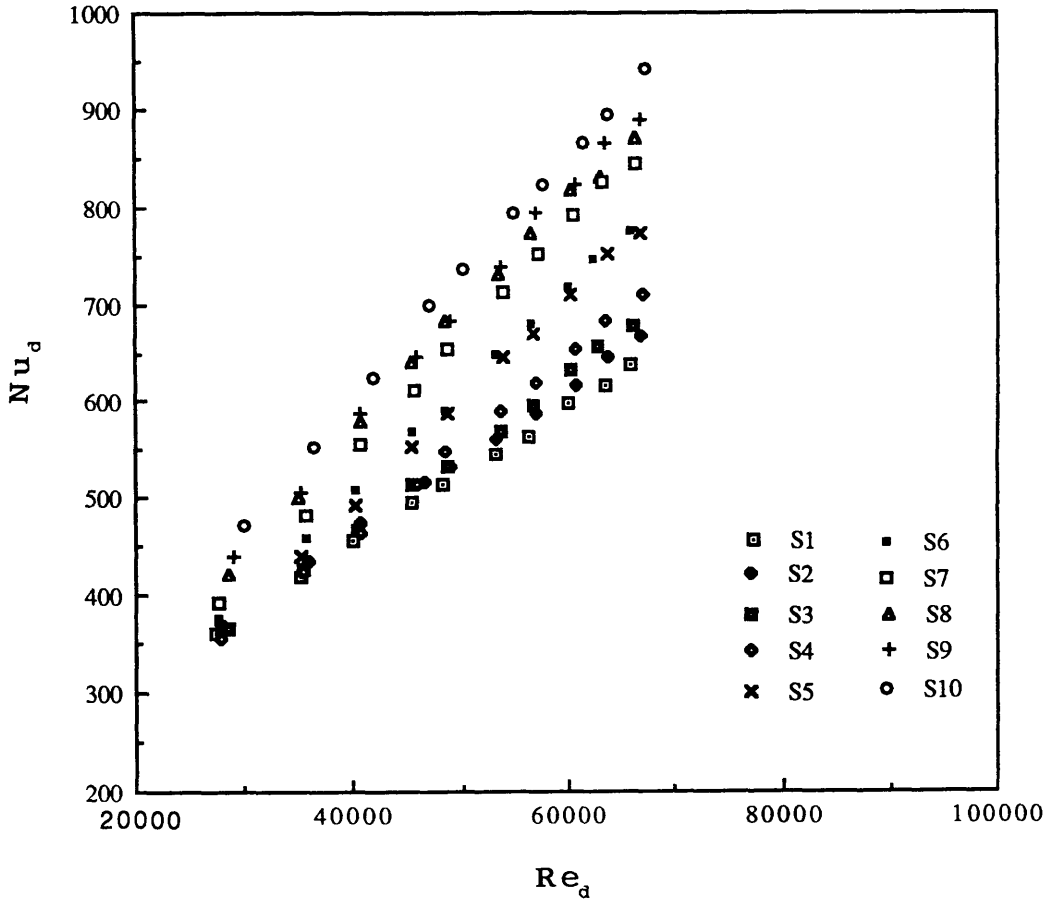

Figure 11: Stagnation-point Nusselt numbers for the ten surfaces as a function of Reynolds number for the 4.4 mm diameter jet.

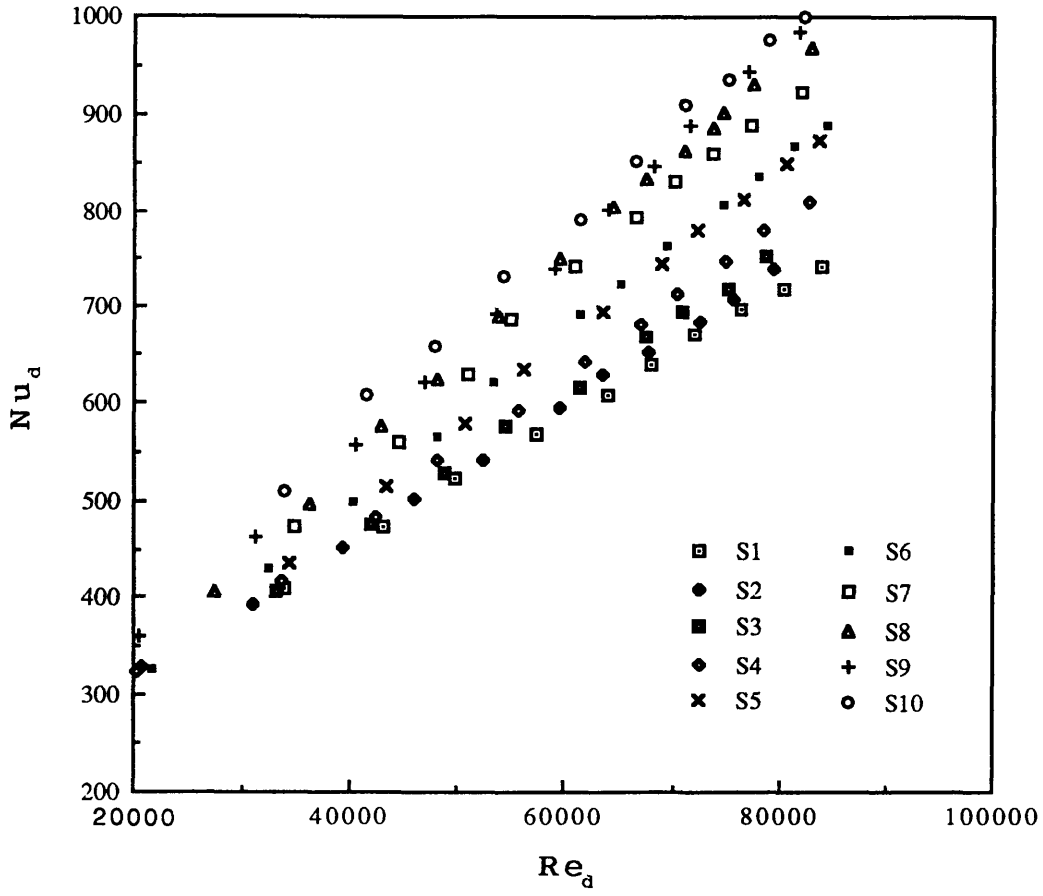

Figure 12: Stagnation-point Nusselt numbers for the ten surfaces as a function of Reynolds number for the 6.0 mm diameter jet.

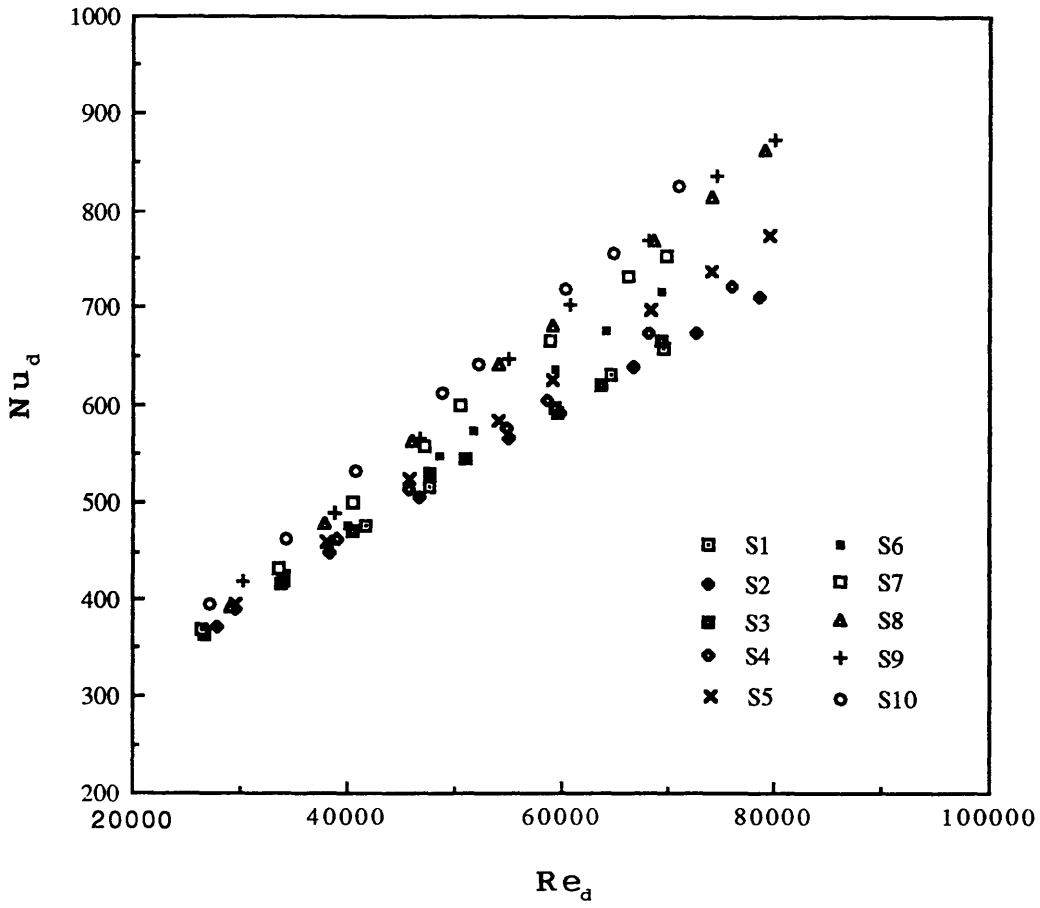

Figure 13: Stagnation-point Nusselt numbers for the ten surfaces as a function of Reynolds number for the 9.0 mm diameter jet.

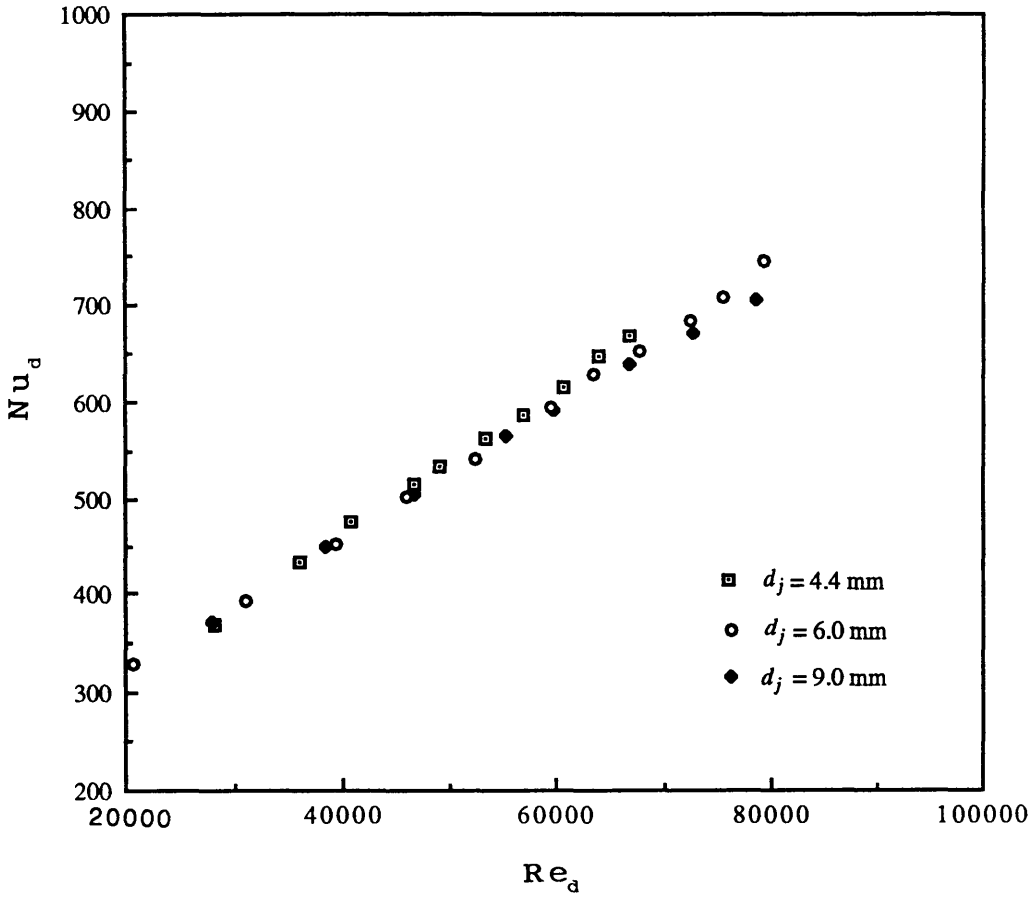

Figure 14: Stagnation-point Nusselt number as a function of Reynolds number for surface S2, k = 4.7 μm, for the three nozzles.

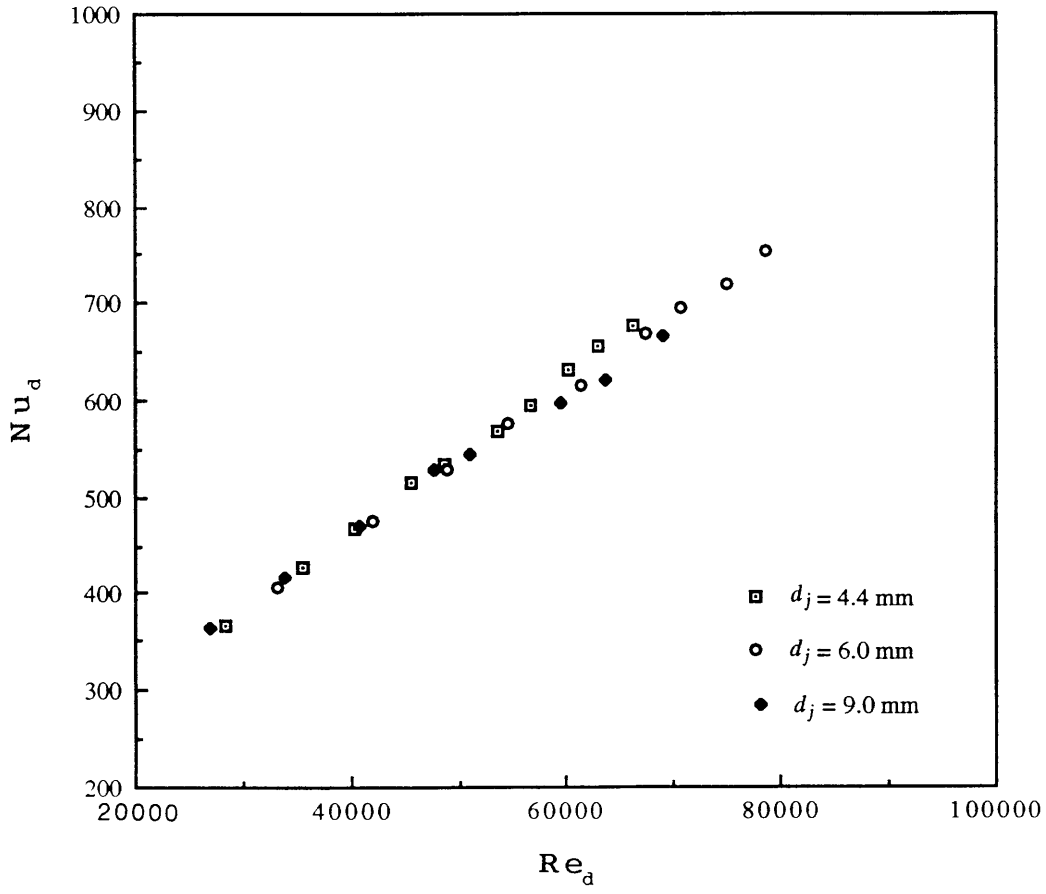

Figure 15: Stagnation-point Nusselt number as a function of Reynolds number for surface S3, k = 6.3 μm, for the three nozzles.

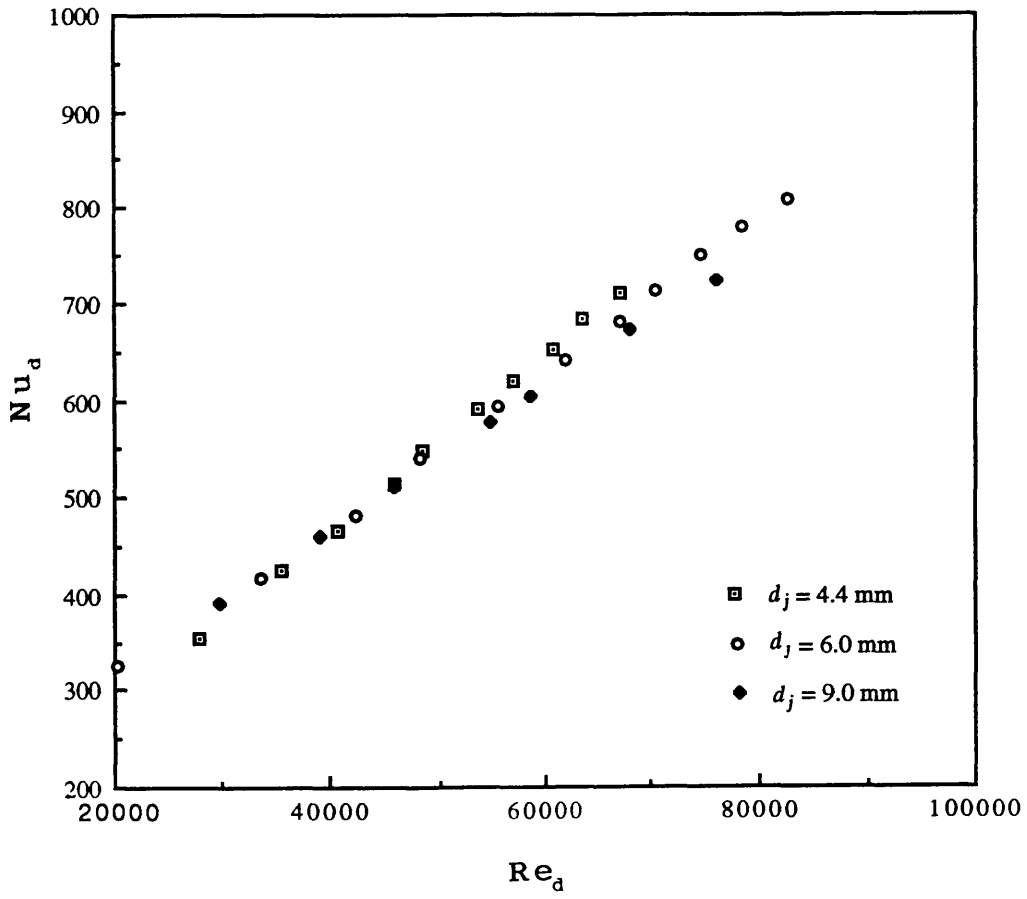

Figure 16: Stagnation-point Nusselt number as a function of Reynolds number for surface S4, k = 8.6 μm, for the three nozzles.

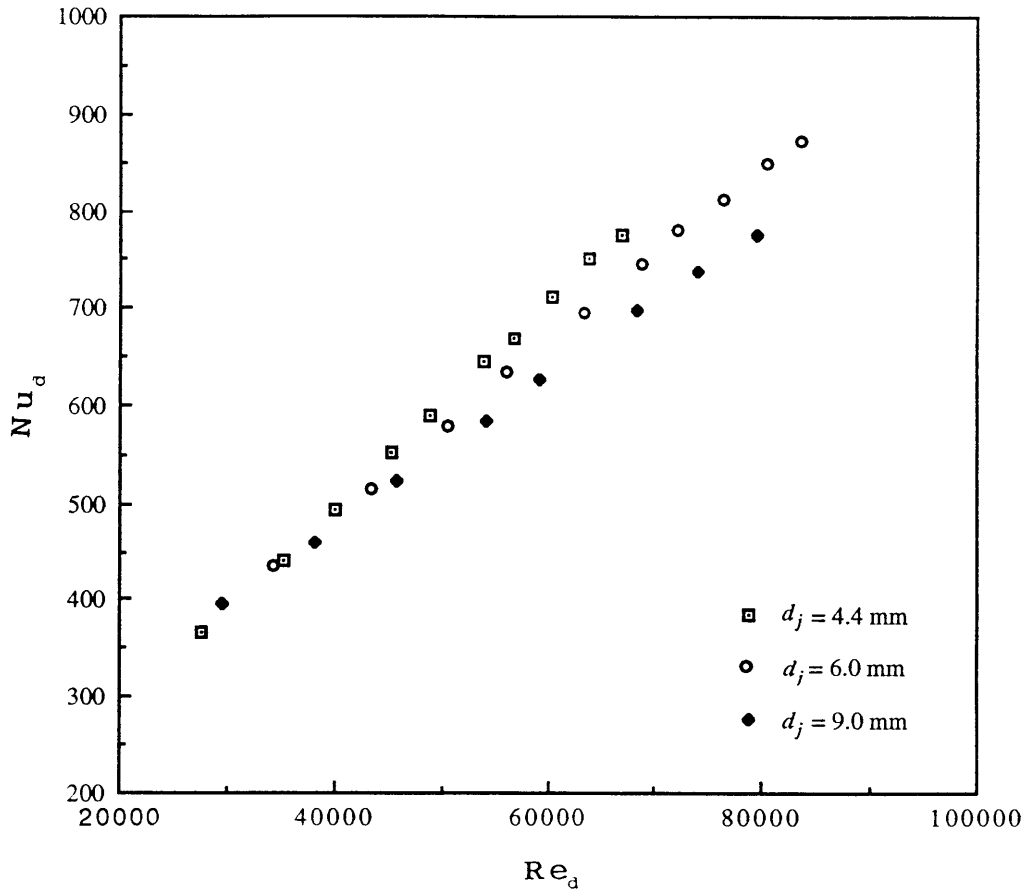

Figure 17: Stagnation-point Nusselt number as a function of Reynolds number for surface S5, k = 13.1 μm, for the three nozzles.

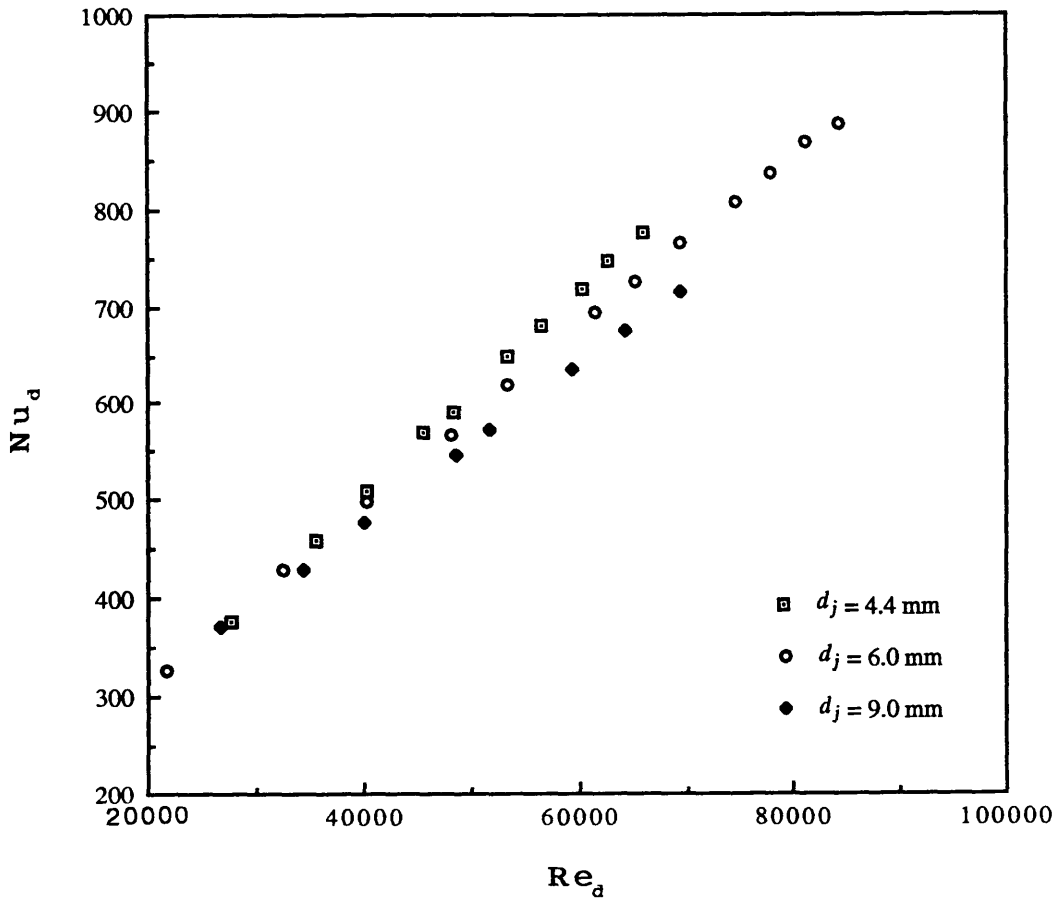

Figure 18: Stagnation-point Nusselt number as a function of Reynolds number for surface S6, k = 14.1 μm, for the three nozzles.

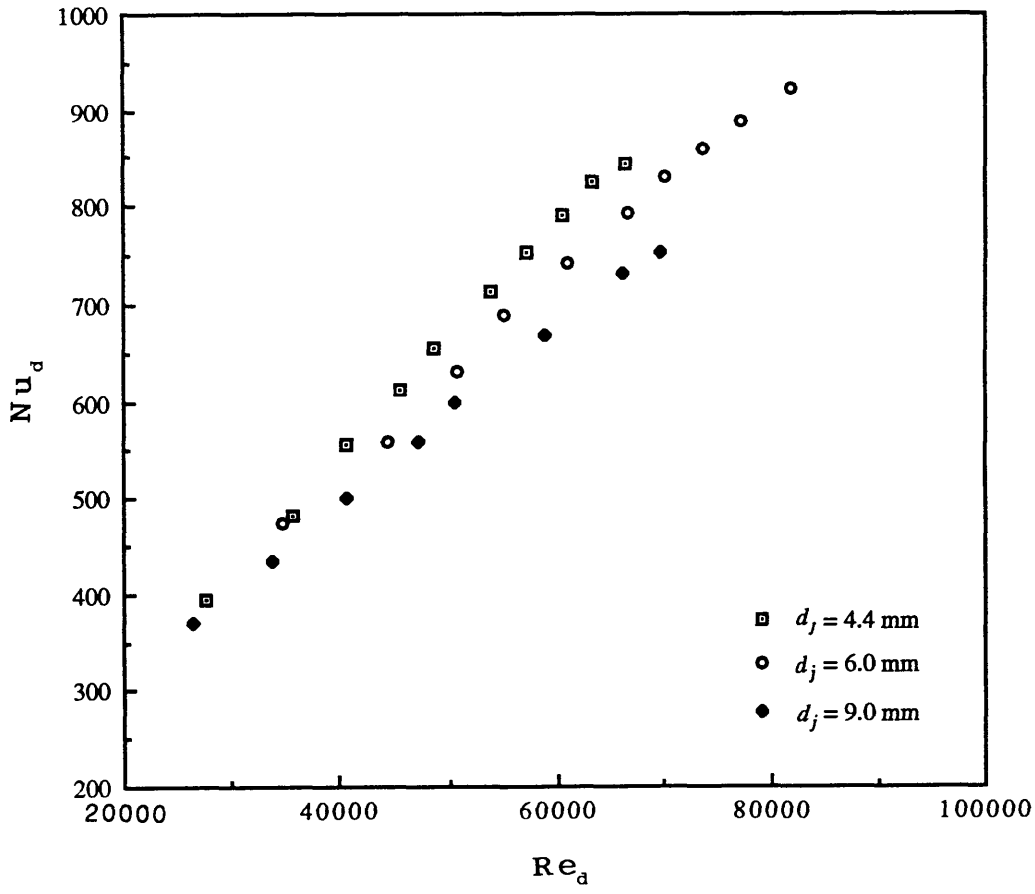

Figure 19: Stagnation-point Nusselt number as a function of Reynolds number for surface S7, k = 20.1 μm, for the three nozzles.

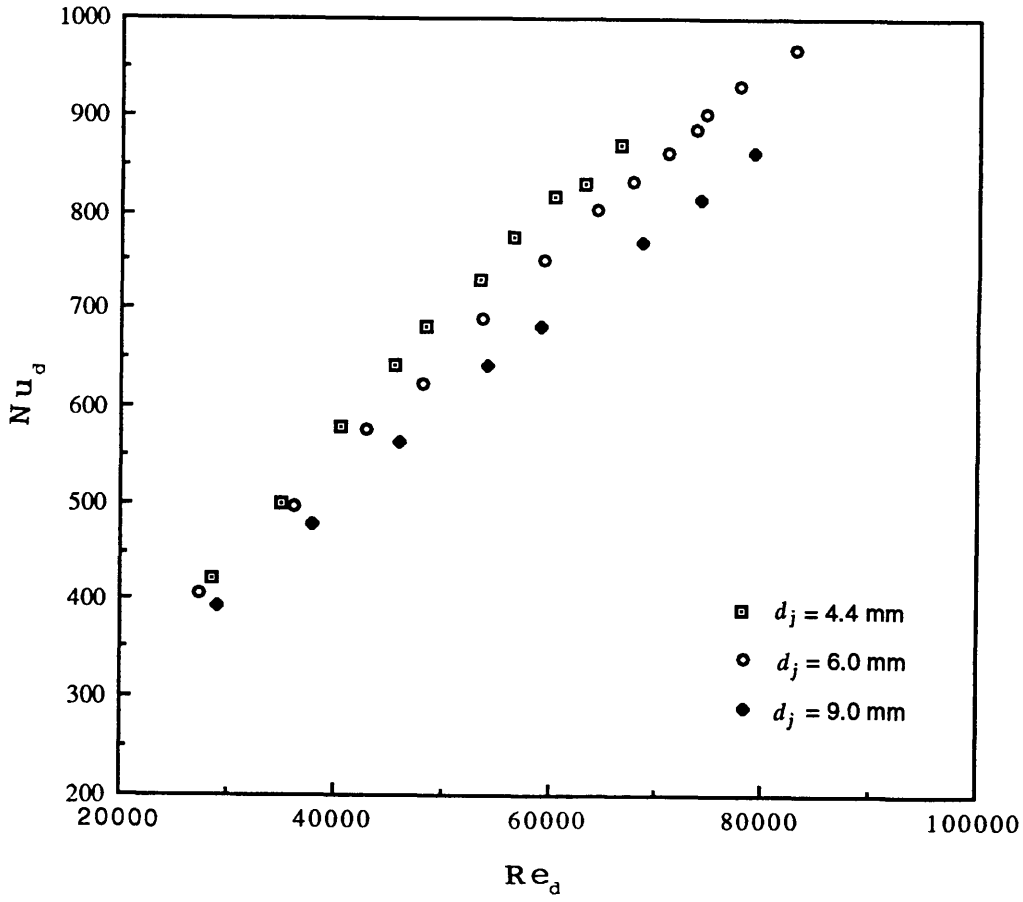

Figure 20: Stagnation-point Nusselt number as a function of Reynolds number for surface S8, k = 25.9 μm, for the three nozzles.

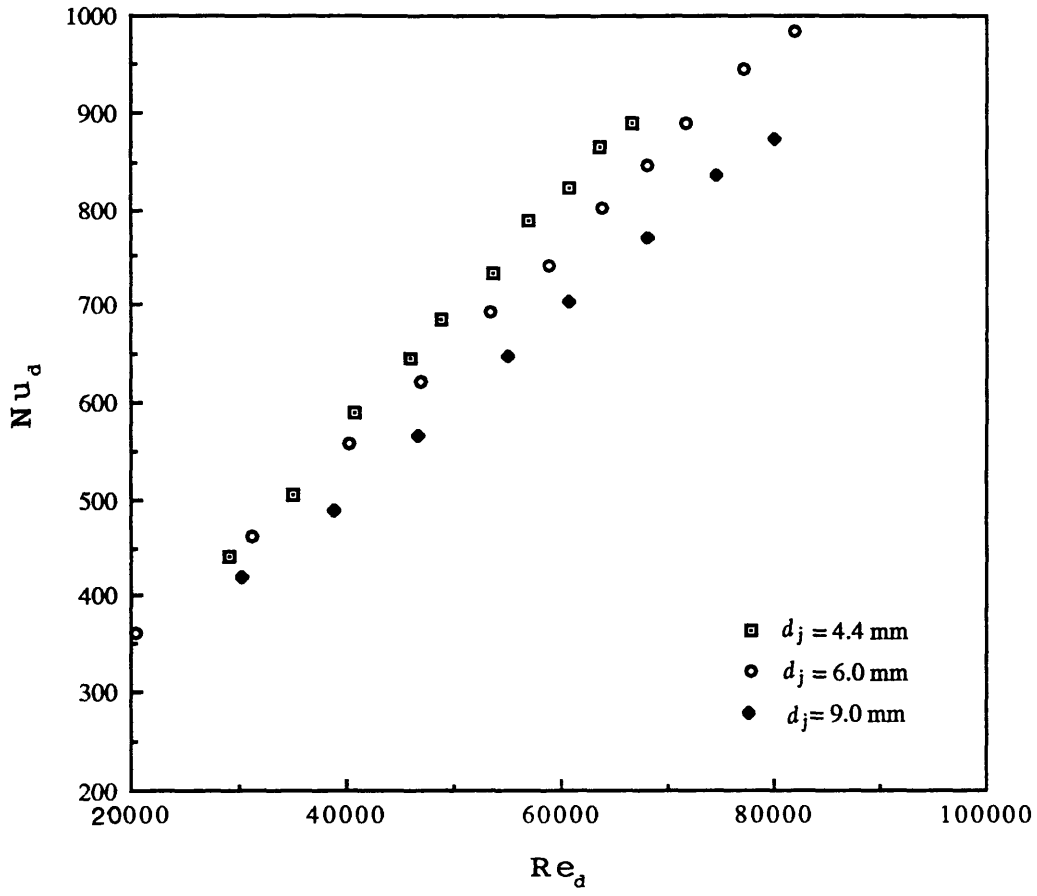

Figure 21: Stagnation-point Nusselt number as a function of Reynolds number for surface S9, k = 26.5 μm, for the three nozzles.

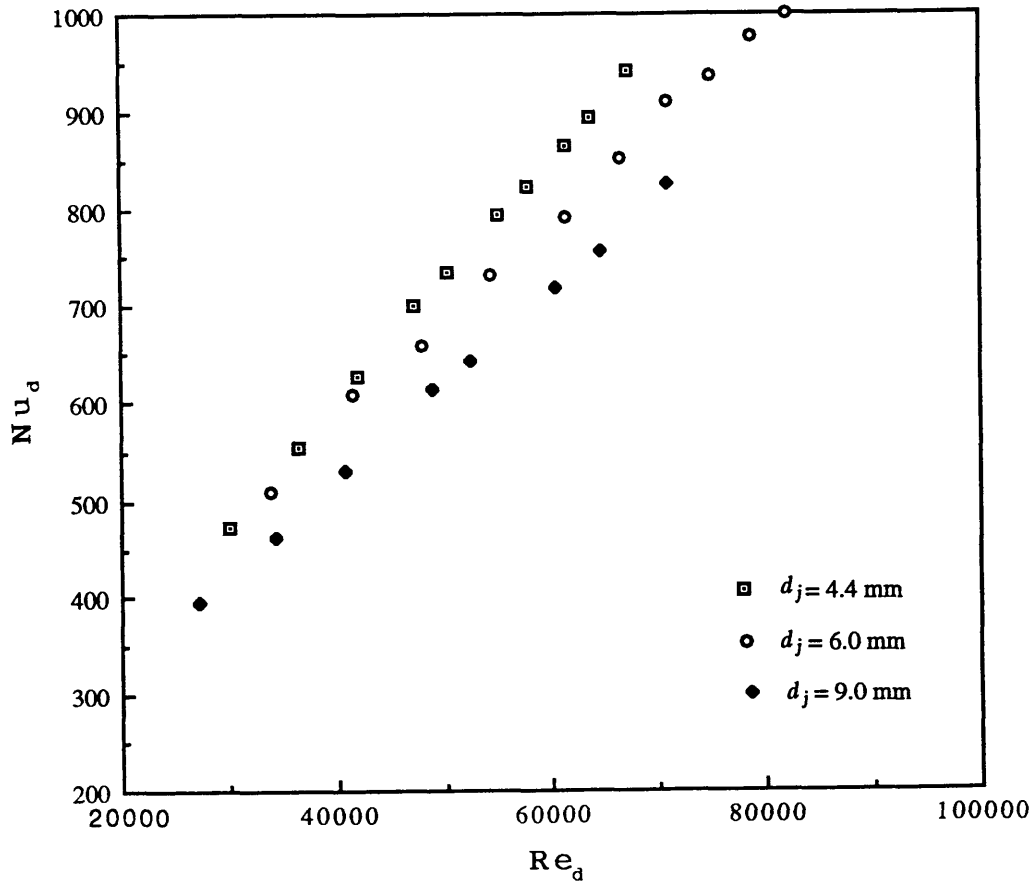

Figure 22: Stagnation-point Nusselt number as a function of Reynolds number for surface S10, k = 28.2 μm, for the three nozzles.

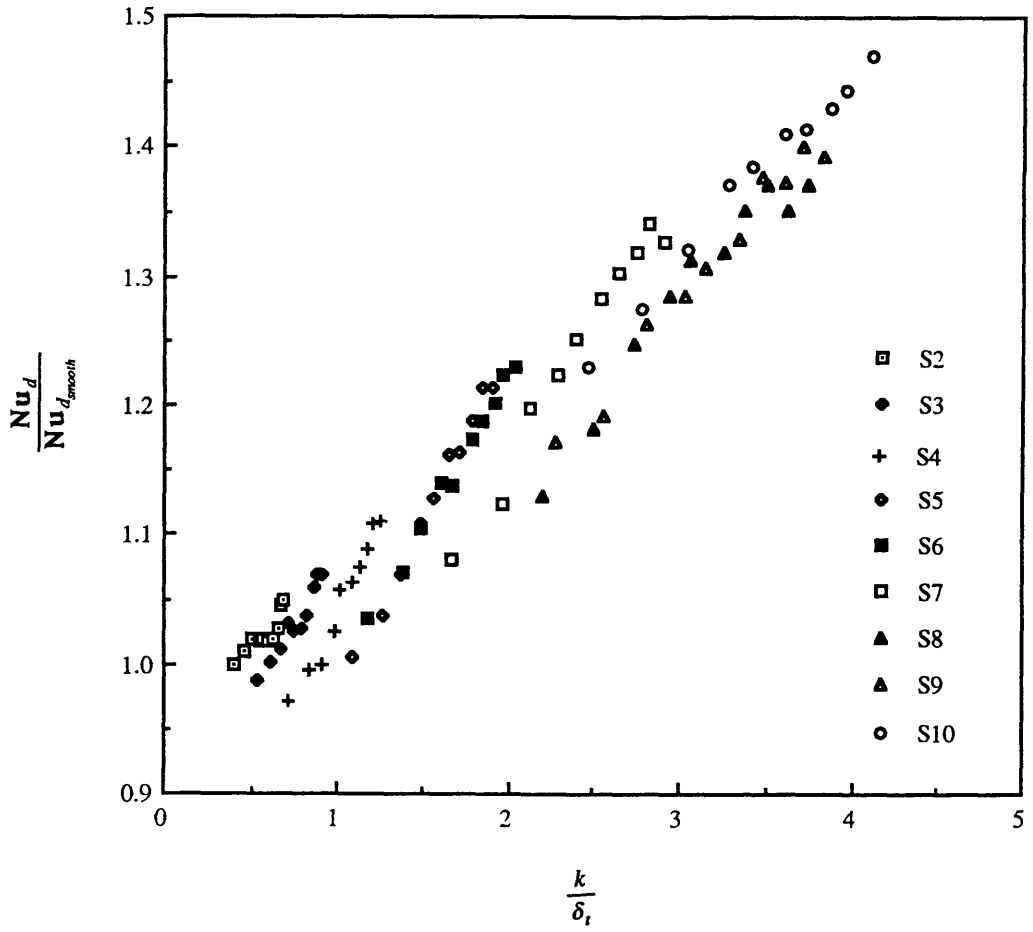

Figure 23: Proof that the rough wall Nusselt number relative to smooth wall Nusselt number does not scale solely with k / δ_t for the 4.4 mm diameter jet.

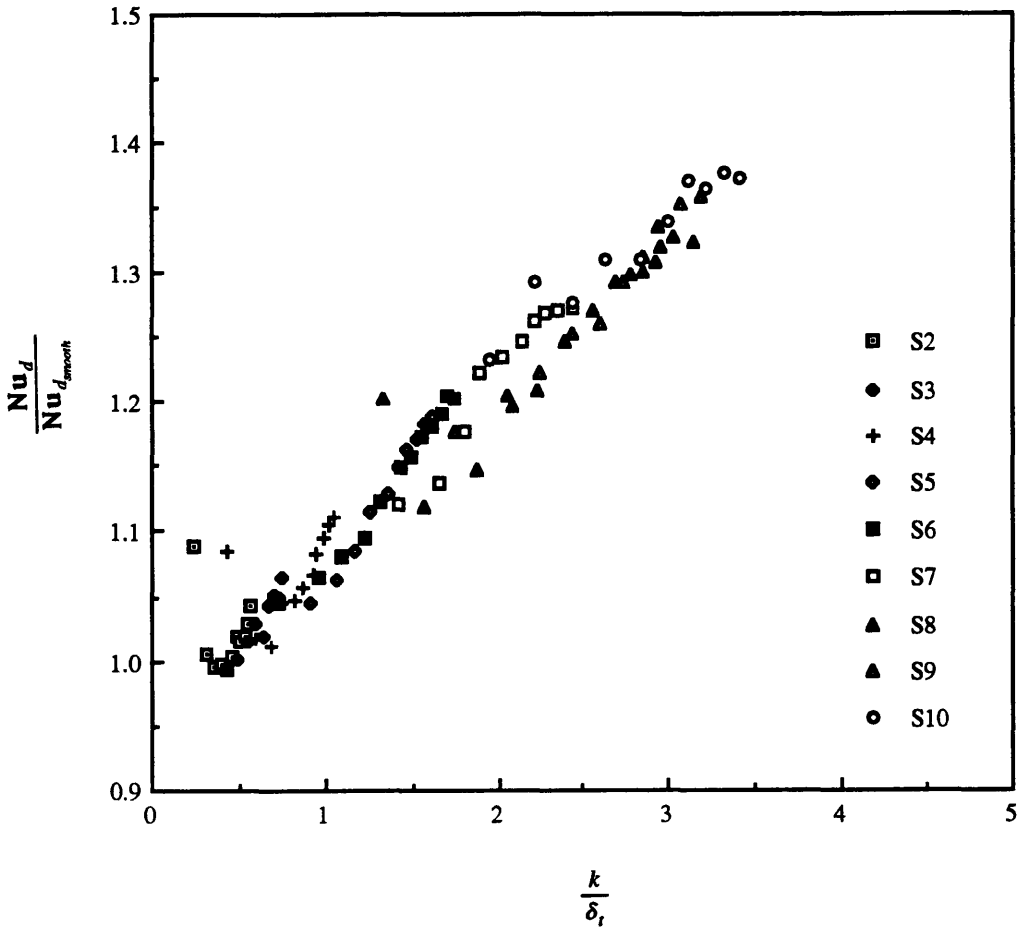

Figure 24: Proof that the rough wall Nusselt number relative to smooth wall Nusselt number does not scale solely with k / δ_t for the 6.0 mm diameter jet.

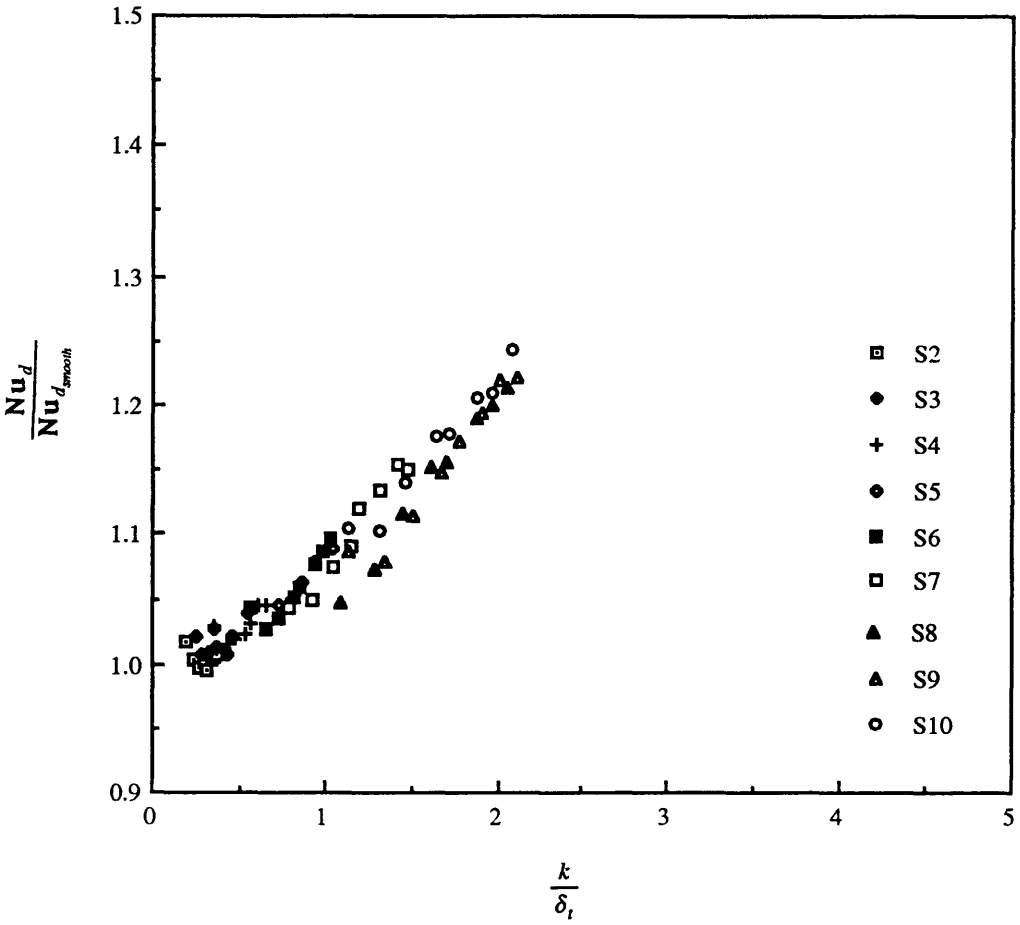

Figure 25: Proof that the rough wall Nusselt number relative to smooth wall Nusselt number does not scale solely with k / δ_t for the 9.0 mm diameter jet.

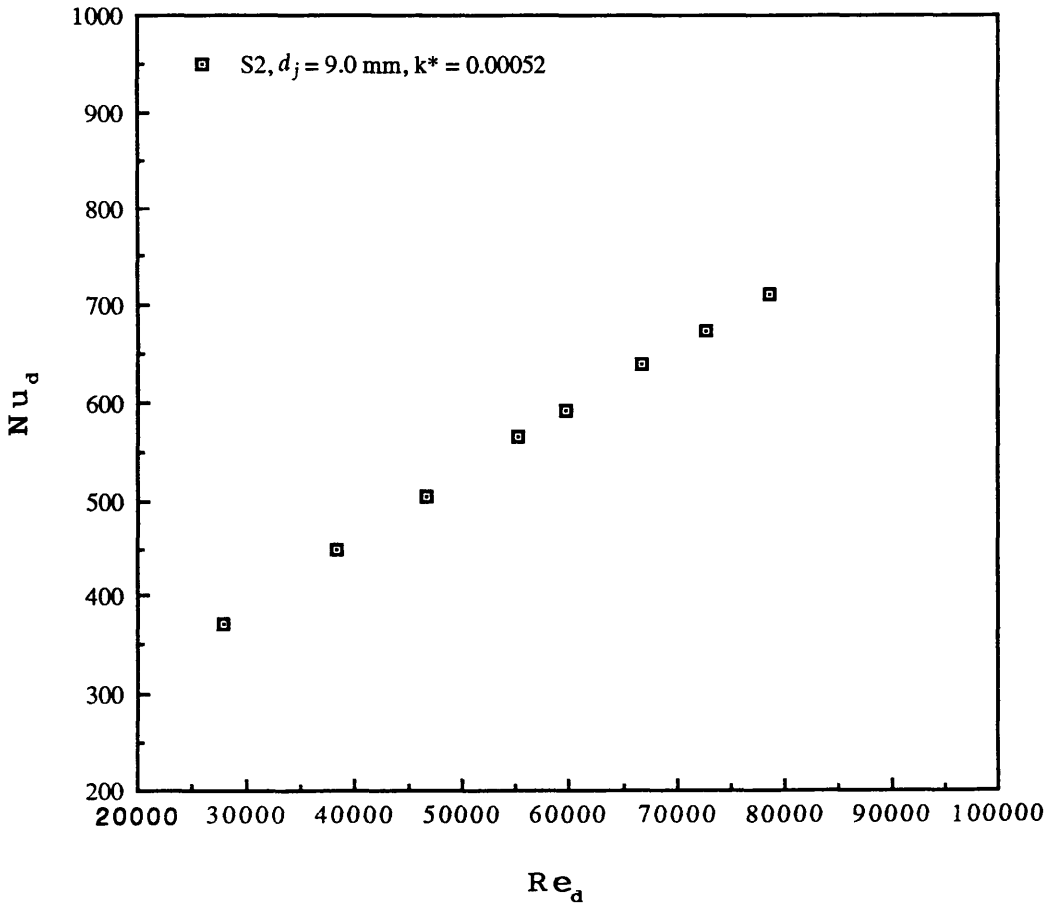

Figure 26: Stagnation-point Nusselt number for $k^* = 0.00052$.

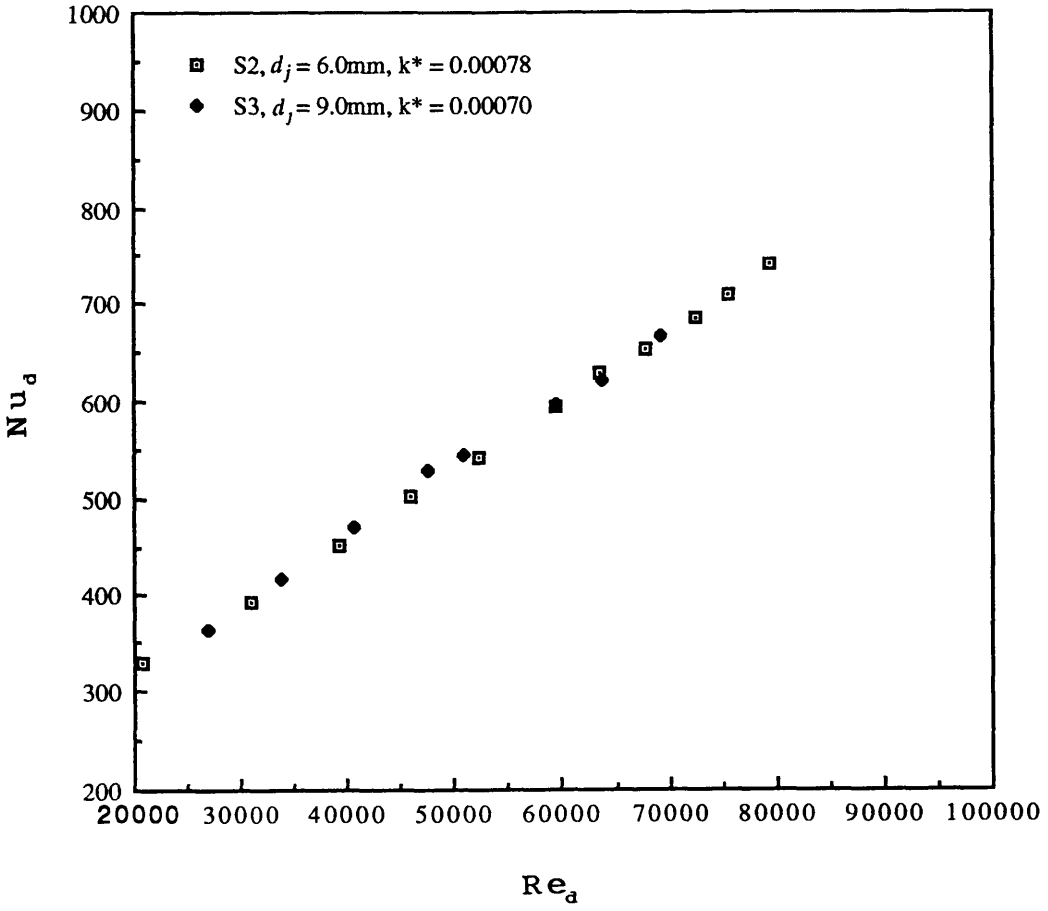

Figure 27: Stagnation-point Nusselt number for k^* = 0.00070 - 0.00078.

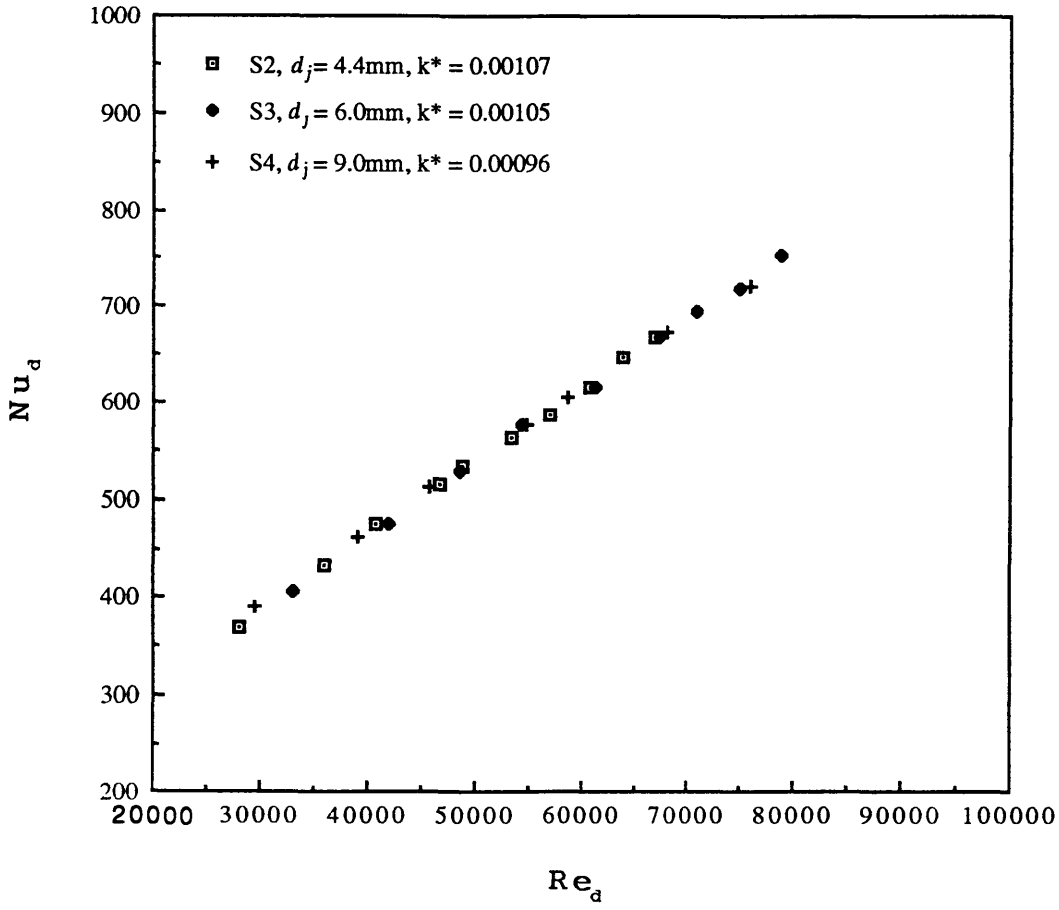

Figure 28: Stagnation-point Nusselt number for k^* = 0.00096 - 0.00107.

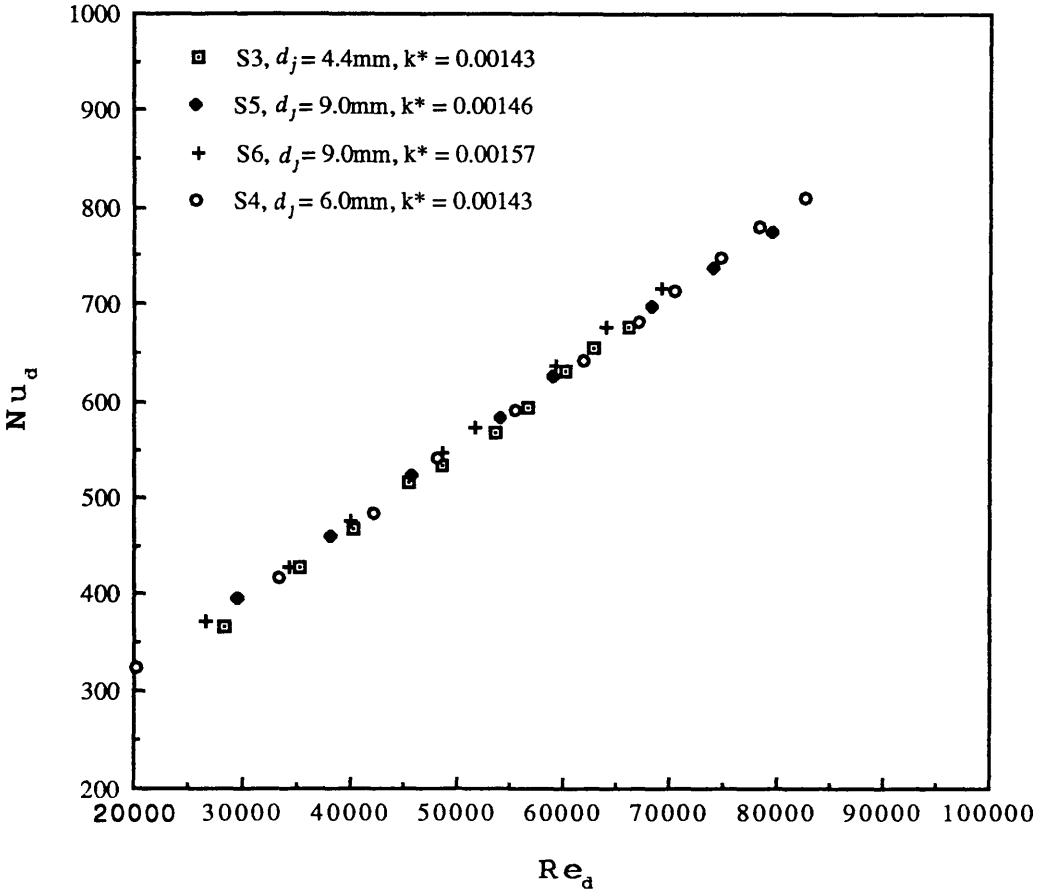

Figure 29: Stagnation-point Nusselt number for k^* = 0.00143 - 0.00157.

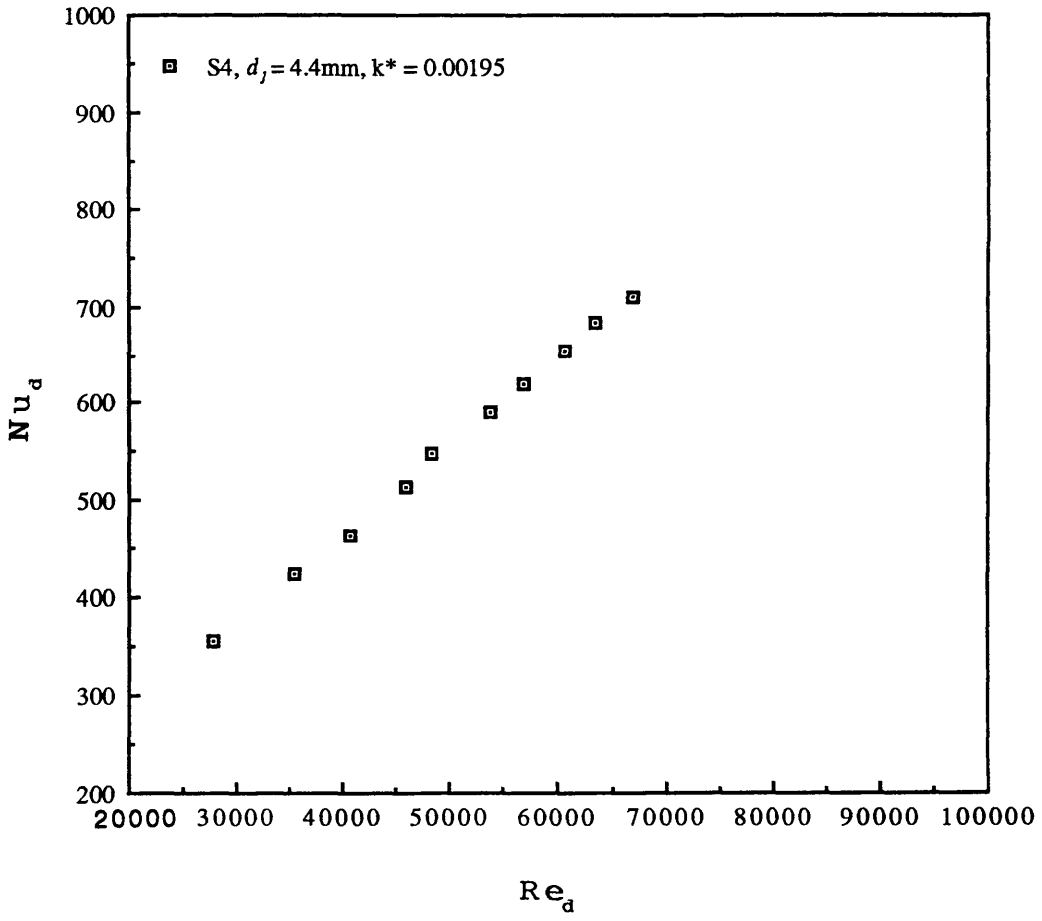

Figure 30: Stagnation-point Nusselt number for $k^* = 0.00195$.

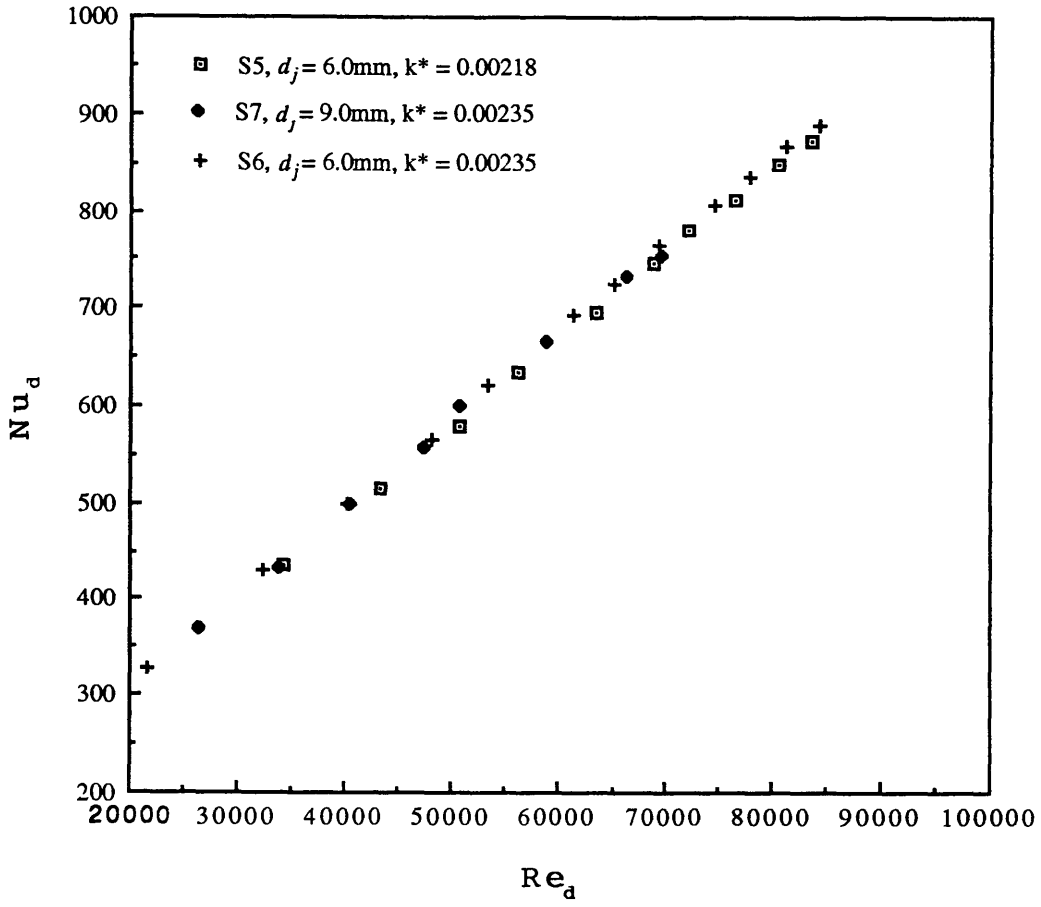

Figure 31: Stagnation-point Nusselt number for k^* = 0.00218 - 0.00235.

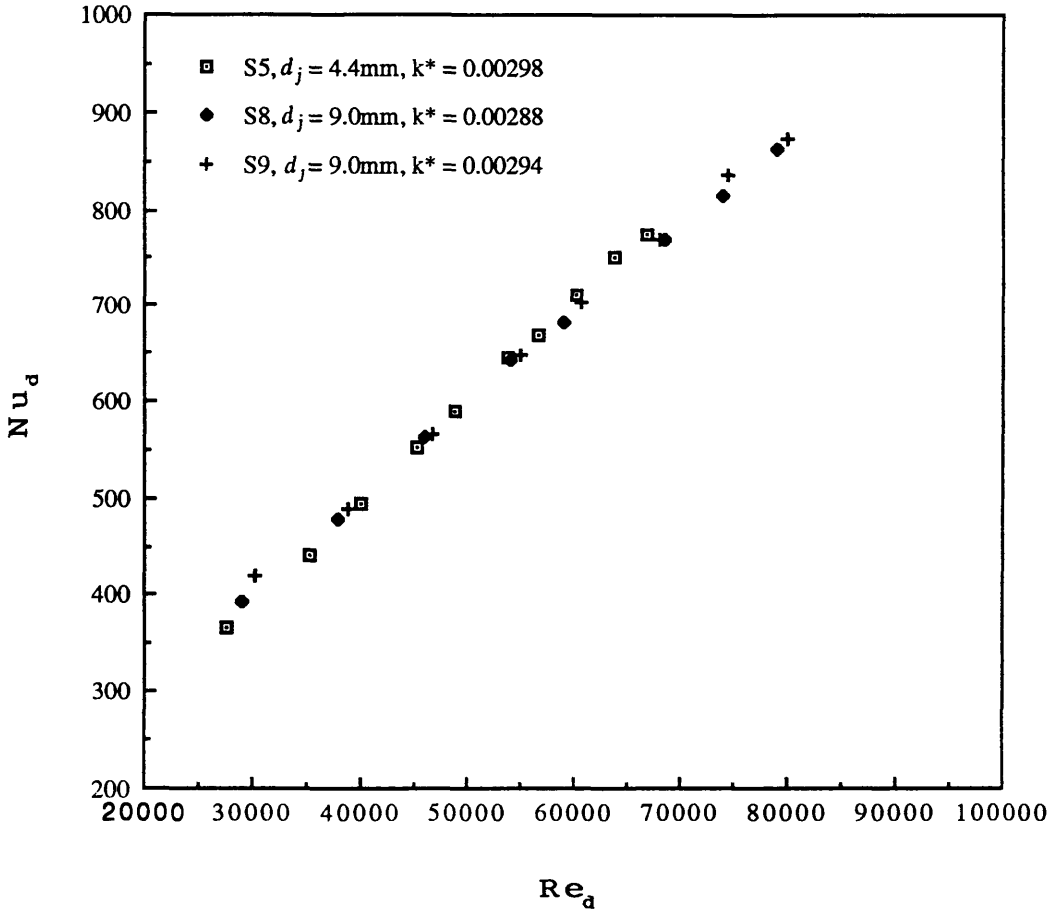

Figure 32: Stagnation-point Nusselt number for k^* = 0.00288 - 0.00298.

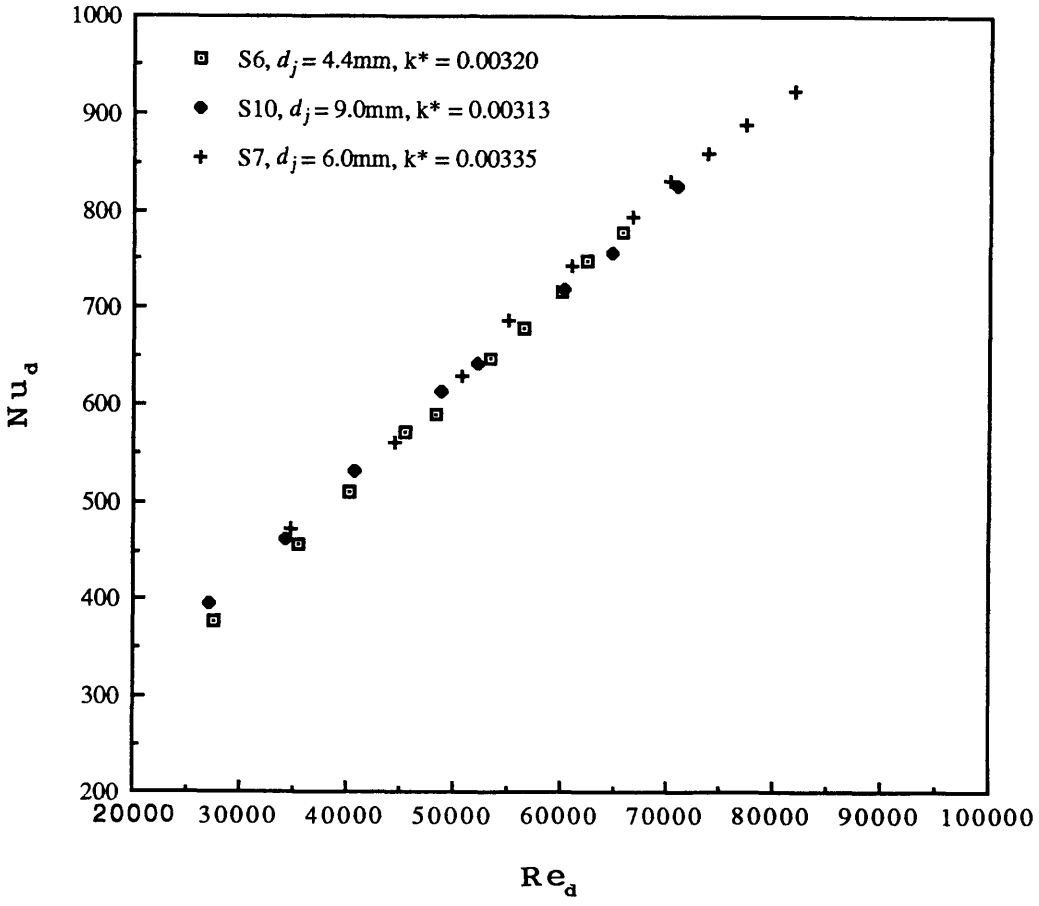

Figure 33: Stagnation-point Nusselt number for k^* = 0.00313 - 0.00335.

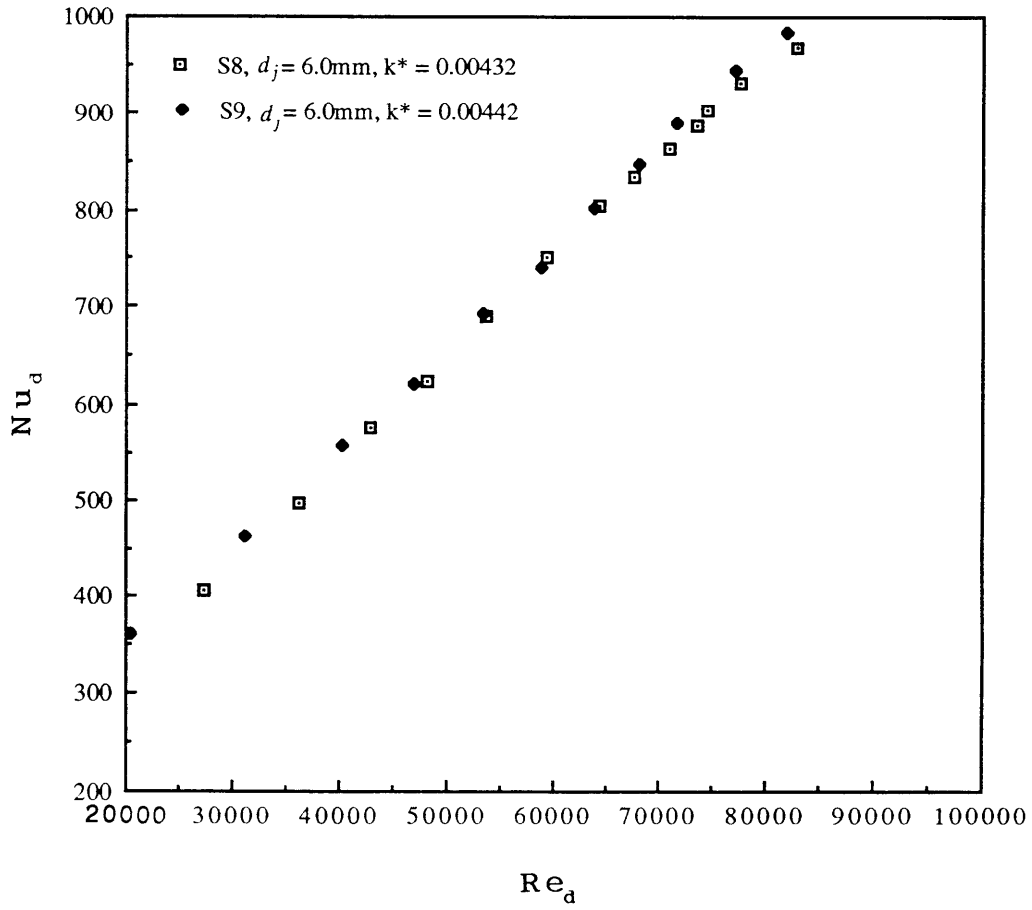

Figure 34: Stagnation-point Nusselt number for k^* = 0.00432 - 0.00442.

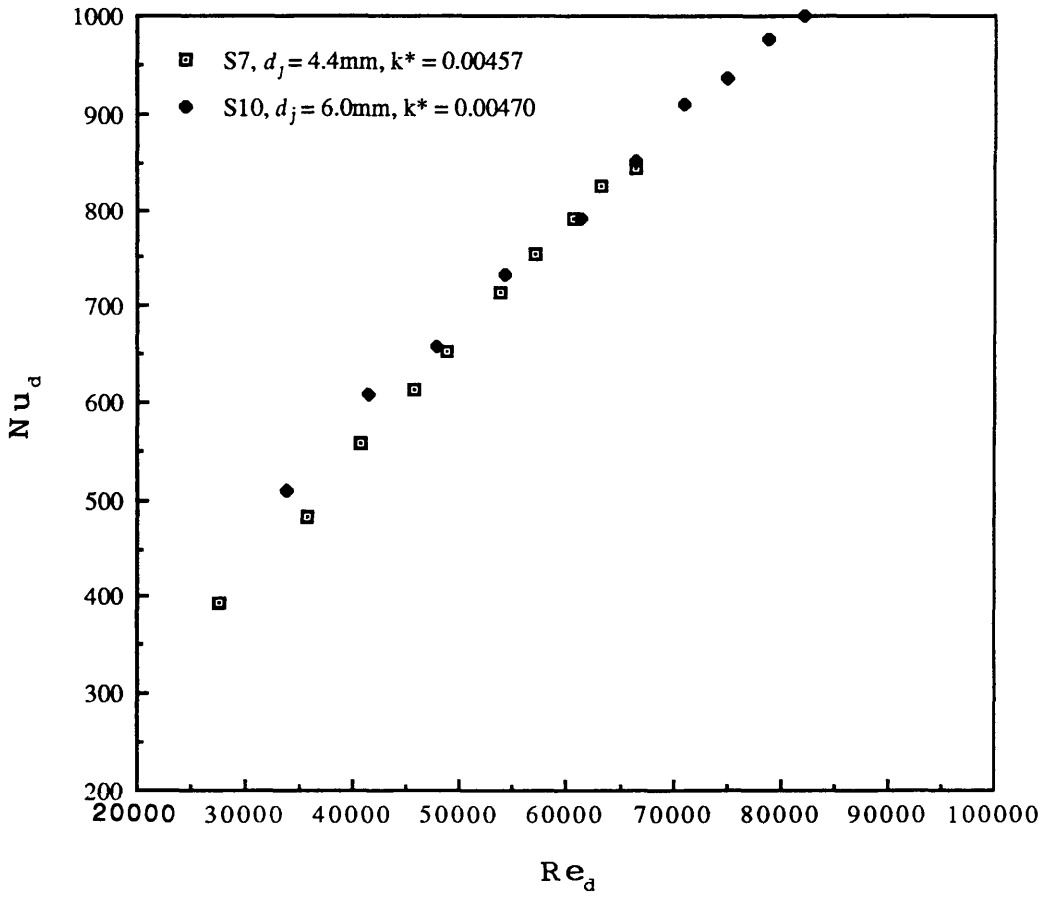

Figure 35: Stagnation-point Nusselt number for k^* = 0.00457 - 0.00470.

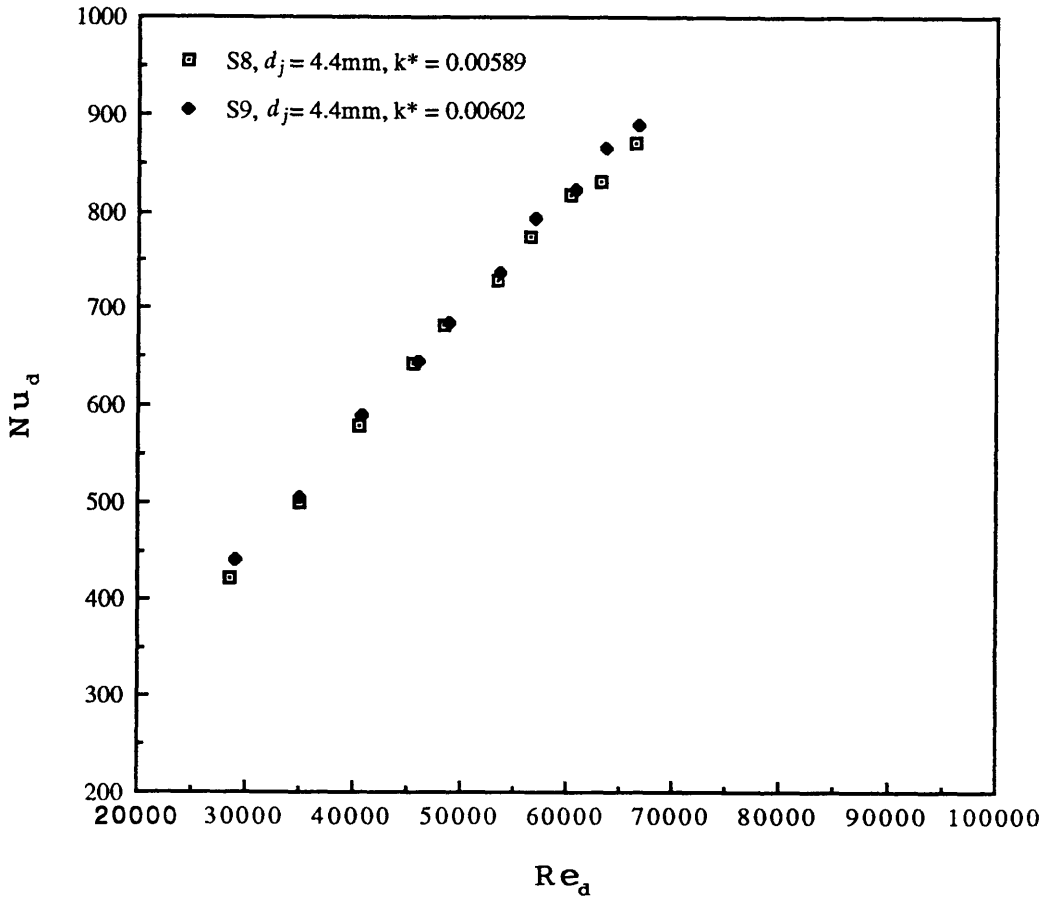

Figure 36: Stagnation-point Nusselt number for k^* = 0.00589 - 0.00602.

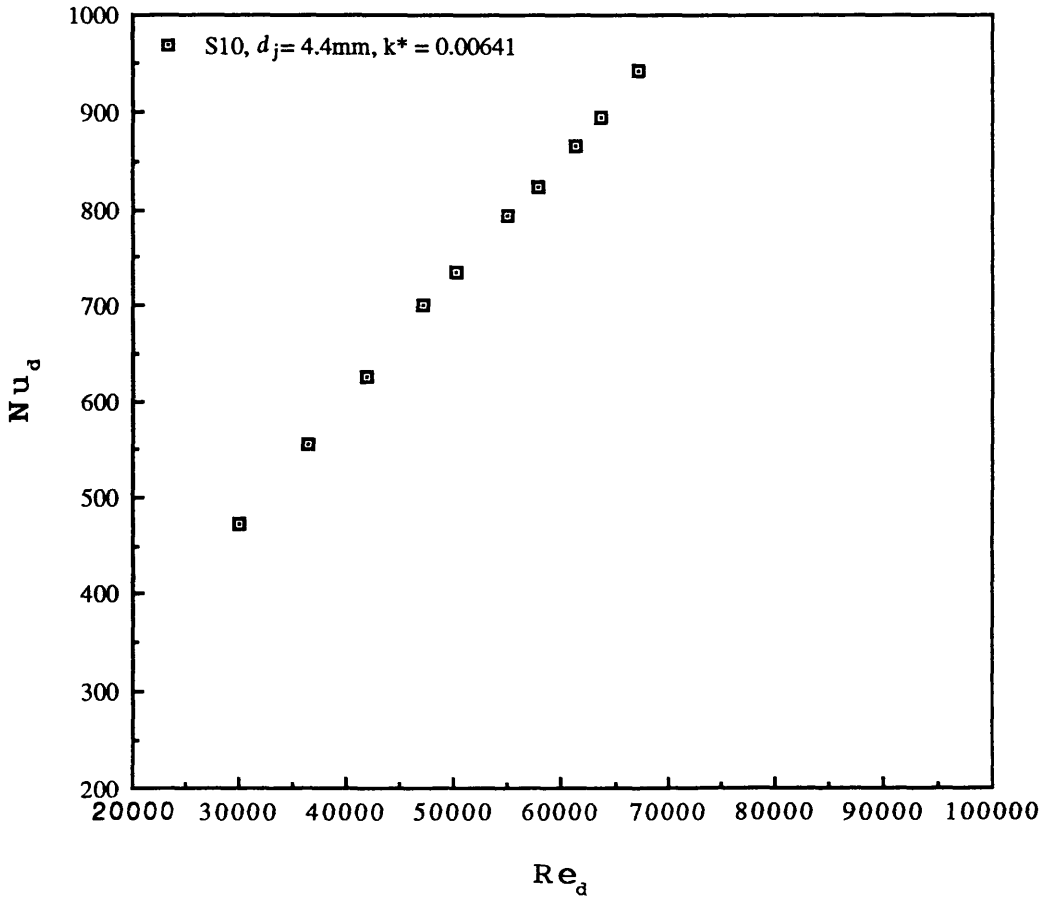

Figure 37: Stagnation-point Nusselt number for $k^* = 0.00641$.

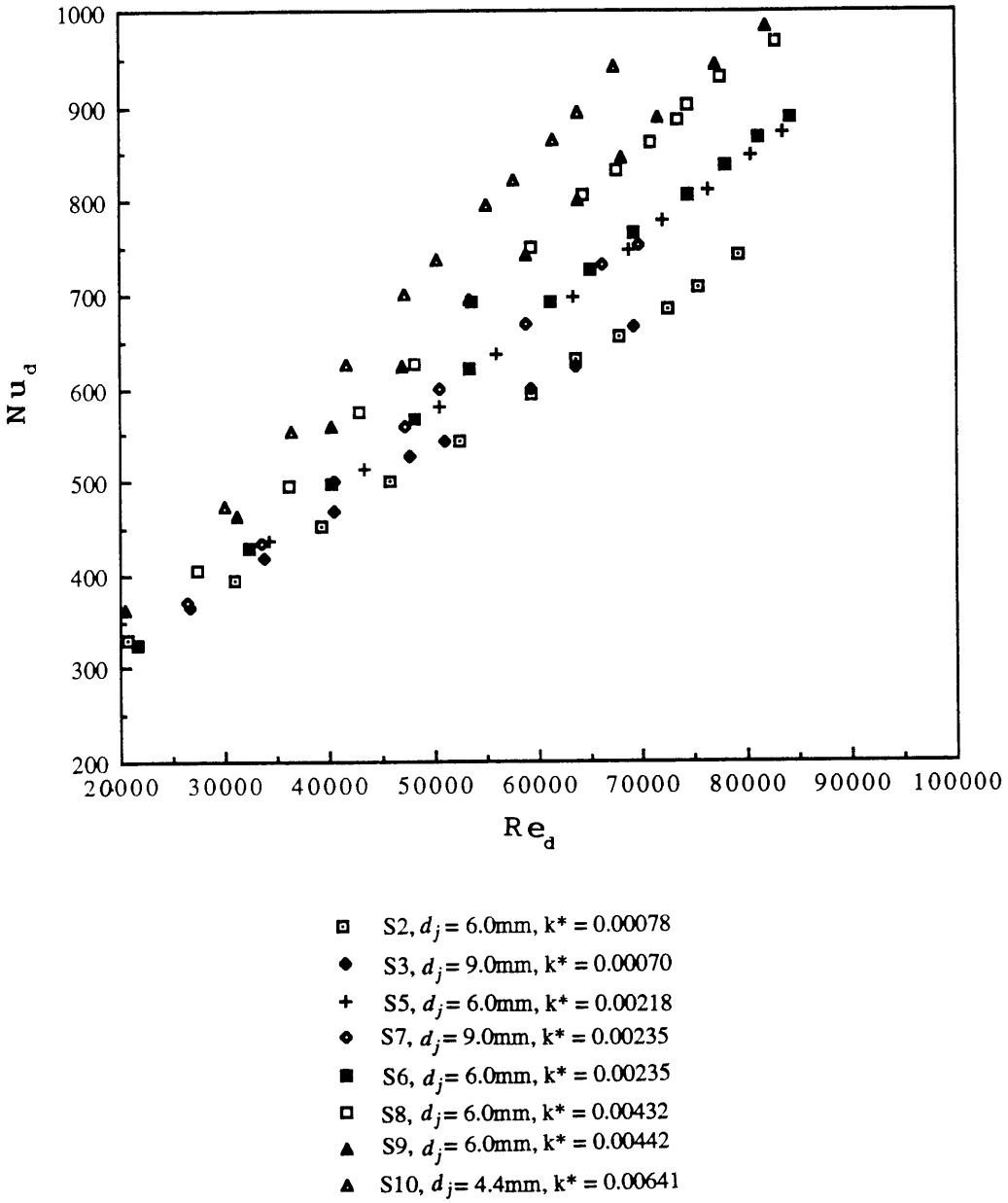

Figure 38: Stagnation-point Nusselt number for $k^* \approx 0.00074$, 0.00229, 0.00437, and 0.00641.

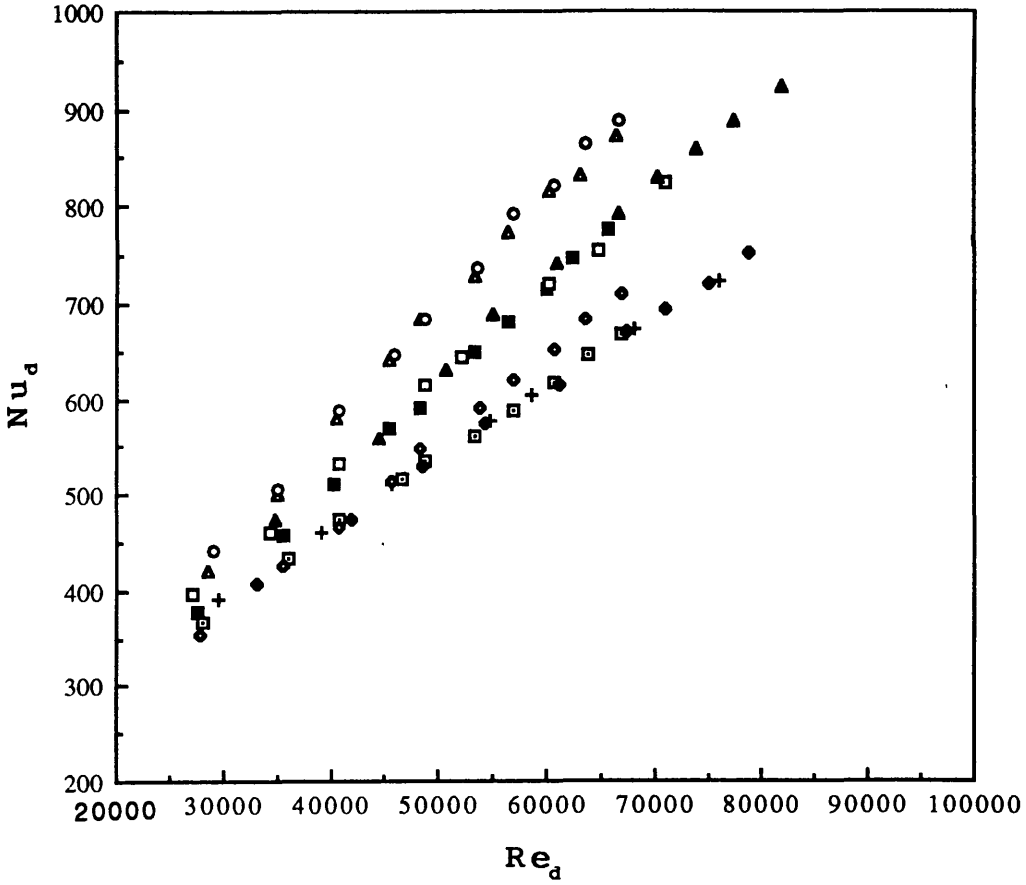

Figure 39: Stagnation-point Nusselt number for $k^* \approx 0.00103$, 0.00195, 0.00323, and 0.00596.

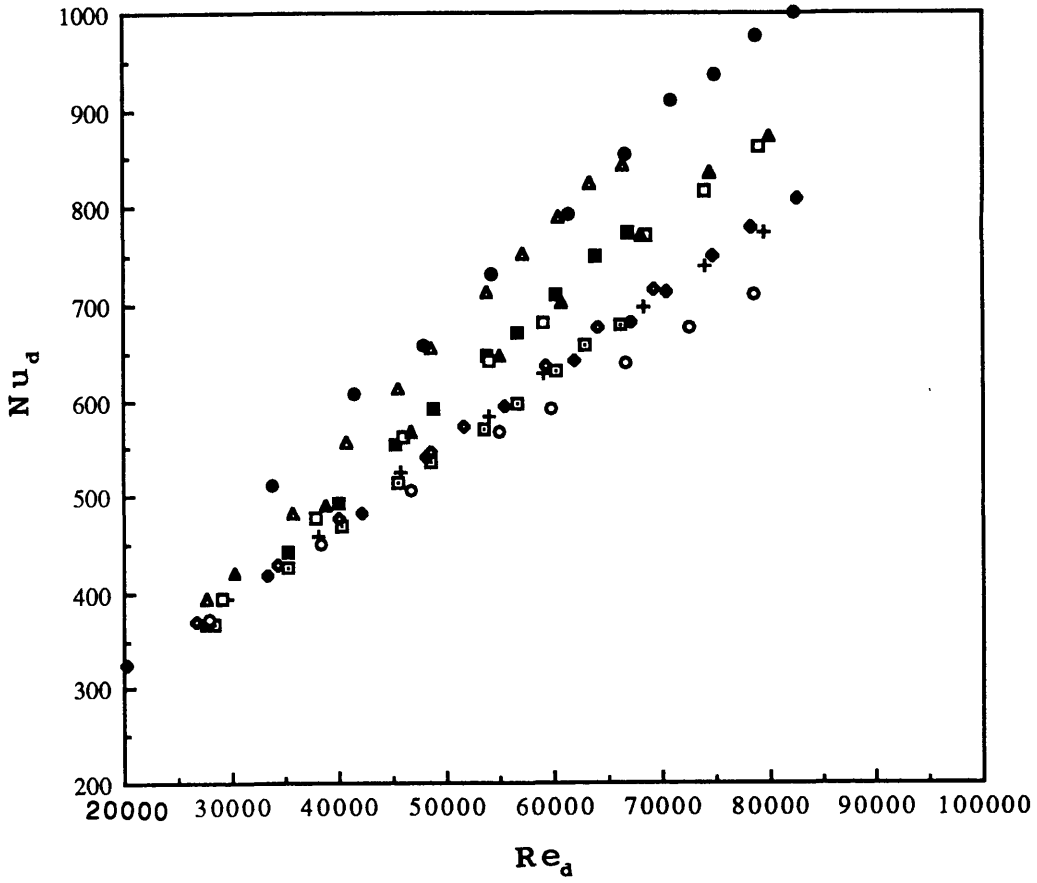

Figure 40: Stagnation-point Nusselt number for $k^* \approx 0.00052$, 0.00147, 0.00293, and 0.00464.

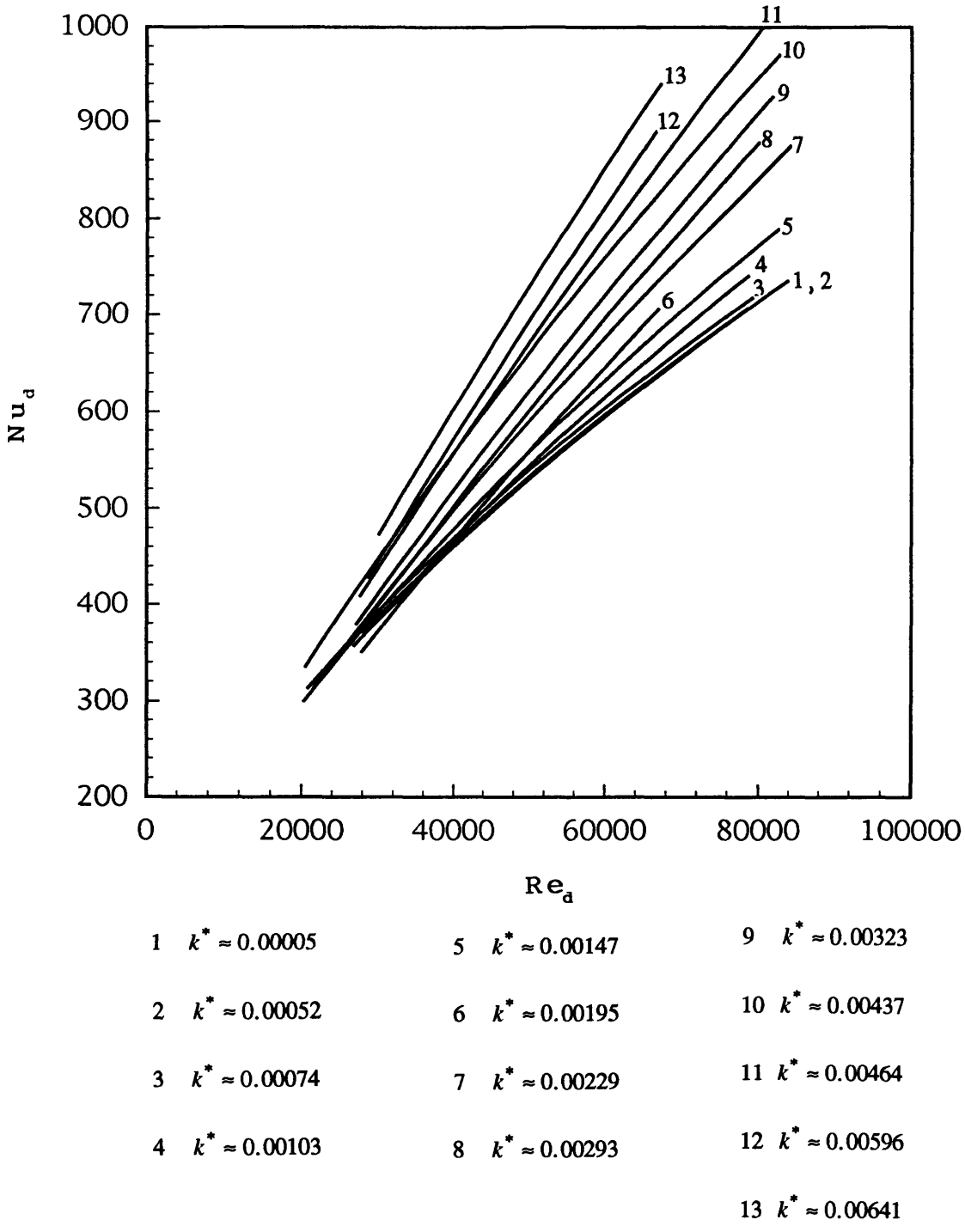

Figure 41: Stagnation-point Nusselt numbers for the full range of k^* investigated: k^* = 0.00052 - 0.00641. Individual data points are left out for clarity.

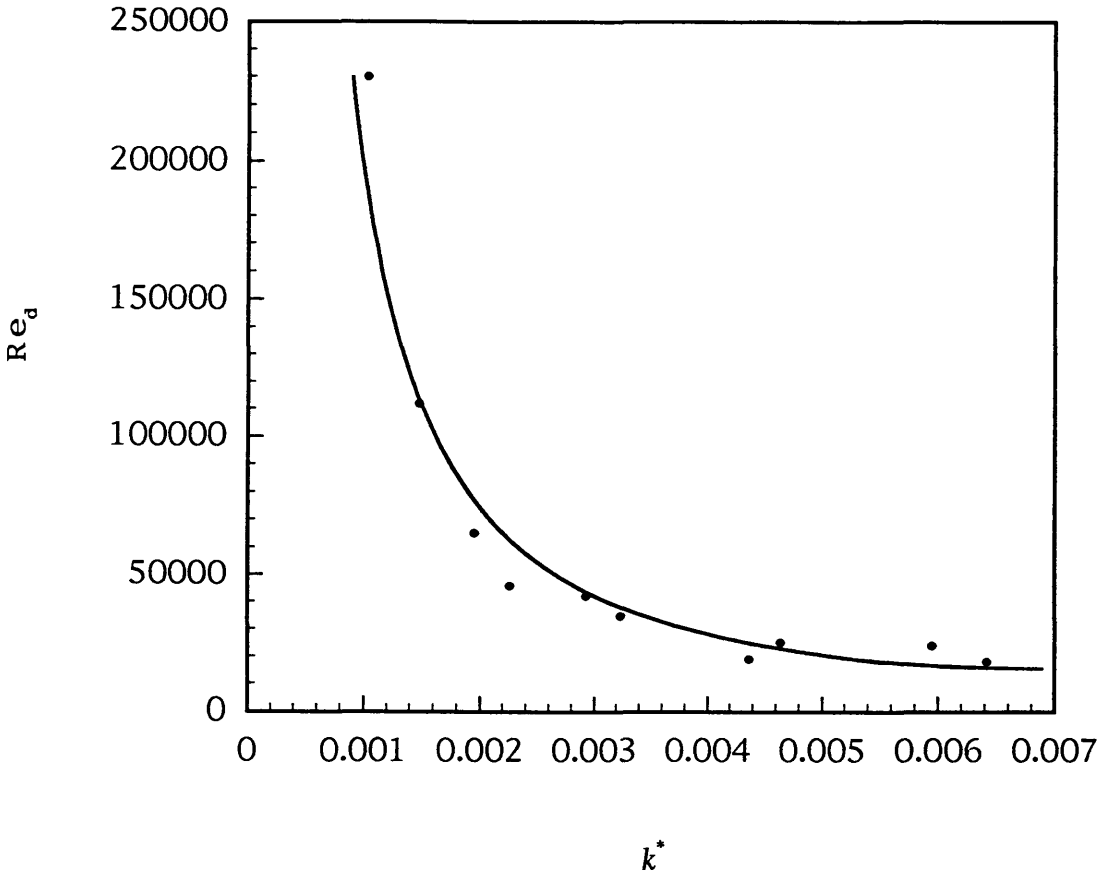

Figure 42: Departure from smooth wall behavior based on an increase of 10% in the Nusselt number, $\mathrm{Re}_d = 12.191 k^{*-1.402}$.

CHAPTER 4

CONCLUSIONS

Stagnation-point heat transfer to an unsubmerged turbulent liquid jet impinging on a rough surface was investigated. Experiments were performed to determine the local Nusselt number at the stagnation point beneath a fully-developed turbulent water jet impinging on a constant heat flux surface. The effects of nozzle-to-target spacing, Reynolds number, and wall roughness were examined. Results from nine well-defined rough surfaces were compared to smooth wall data taken under the same conditions.

The effect of nozzle-to-target separation on the stagnation-point Nusselt number for a smooth wall was found to be negligible over an l/d range of 0.9 - 19.8, with any variations falling within the experimental uncertainty of the data. Data for the stagnation-point Nusselt number did not correlate well with the standard $\mathrm{Re}_d^{1/2}$ scaling; rather, the smooth wall Nusselt number is well represented by $\mathrm{Nu}_d = 0.278\mathrm{Re}_d^{0.633}\mathrm{Pr}^{1/3}$ to an accuracy of ±3%.

Heat transfer can be significantly increased at the stagnation point by the presence of roughness elements. Roughness protrusions greater than a few microns in height can disrupt the thin thermal boundary layer at the stagnation point and increase the heat transfer. Heat transfer enhancement characteristics of a given roughness depend on how deeply the roughness elements protrude into the thermal sublayer. A thinner boundary layer allows roughness elements to protrude further, thereby increasing their

effect. Hence, heat transfer enhancement increases with increasing Reynolds number and decreasing jet diameter due to the corresponding thinning of the thermal boundary layer. Specifically, the Nusselt number was found to scale with k/d_j and Re_d. Increases in the Nusselt number over that of a smooth wall as large as 50% were obtained.

At low Reynolds number, the surfaces examined behave as if they were smooth. Departure from smooth wall behavior was defined by the Reynolds number at which the rough wall Nusselt number became 10% larger than the corresponding smooth wall Nusselt number. Based on this definition, the data show that for $\mathrm{Re}_d < 12.191 k^{*-1.402}$ the flow will remain in the hydrodynamically smooth regime, after which the flow may be considered transitionally rough. More data is needed for Reynolds numbers less than 20,000 and greater than 80,000, as well as for k/d_j less than 5 μm and greater than 30 μm, to examine the hydrodynamically smooth and fully rough regimes.

Since the Prandtl number was only varied over the narrow range of 8.2 - 9.1, its exact influence is not known. However, assuming the typical high Prandtl number exponent of 1/3, we believe that the wall will behave as if it were smooth for $k^{*}\mathrm{Re}_d^{0.713}\mathrm{Pr}^{1/3} < 12.050$. Further investigation of Prandtl number effects would be useful.

REFERENCES

American Society for Metals, 1983, *ASM Metal Reference Book*, 2nd ed., p. 210.

Bhunia, S. K., and Lienhard V, J. H., 1992, "Splattering of Turbulent Liquid Jets Impinging on Solid Targets: Parametric Studies," *General Papers in Heat Transfer*, ASME HTD, Vol. 204, pp. 165 - 171.

Blevins, R. D., 1984, *Applied Fluid Dynamics Handbook*, Van Nostrand Reinhold Company, Inc., NY, p. 73.

Coleman, H. W., 1976, "Momentum and Energy Transport in the Accelerated Fully Rough Turbulent Boundary Layer," Ph. D. Dissertation, Mechanical Engineering Department, Stanford University.

Cope, W. F., 1941, "The Friction and Heat Transmission Coefficients of Rough Pipes," *Proc. Inst. Mech. Engrs.*, Vol. 145, pp. 99 - 105.

Dipprey, D. F., and Sabersky, R. H., 1963, "Heat and Momentum Transfer in Smooth and Rough Tubes at Various Prandtl Numbers," *Int. J. Heat Mass Transfer*, Vol. 6, pp. 329-353.

Gabour, L. A., 1991, "Heat Transfer to Turbulent and Splattering Impinging Liquid Jets," S. B. Thesis in Mechanical Engineering, M.I.T.

Gowen, R. A., and Smith, J. W., 1968, "Turbulent Heat Transfer from Smooth and Rough Surfaces," *Int. J. Heat Mass Transfer*, Vol. 11, pp. 1657 - 1673.

Healzer, J. M., 1974, "The Turbulent Boundary Layer on a Rough, Porous Plate: Experimental Heat Transfer with Uniform Blowing," Ph.D. Dissertation, Mechanical Engineering Department, Stanford University.

Hosni, M. H., Coleman, H. W., and Taylor, R. P., 1990, "Heat Transfer Measurements and Calculations in Transitionally Rough Flow," ASME paper 90-GT-53.

Hosni, M. H., Coleman, H. W., and Taylor, R. P., 1991, "Measurements and Calculations of Rough-Wall Heat Transfer in the Turbulent Boundary Layer," *Int. J. Heat Mass Transfer*, Vol. 34, pp. 1067 - 1082.

Kalpakjian, S., 1985, *Manufacturing Processes for Engineering Materials*, Addison-Wesley Publishing Company, Inc., MA, pp. 180 - 194.

Lienhard, J. H., 1987, *A Heat Transfer Textbook*, 2nd ed., Prentice-Hall. Inc., NJ.

Lienhard V, J. H., Liu, X., and Gabour, L. A., 1992, "Splattering and Heat Transfer During Impingement of a Turbulent Liquid Jet," *Journal of Heat Transfer*, Vol. 114, pp. 362 - 372.

Ligrani, P. M., 1979, "The Thermal and Hydrodynamic Behavior of Thick, Rough-Wall, Turbulent Boundary Layers," Ph. D. Dissertation, Mechanical Engineering Department, Stanford University.

Liu, X., Gabour, L. A., and Lienhard V, J. H., 1992, "Stagnation Point Heat Transfer During Impingement of Laminar Liquid Jets: Analysis with Surface Tension Effects," *General Papers in Heat Transfer*, ASME HTD, Vol. 204, pp. 173 - 182.

Liu, X., Lienhard V, J. H., and Lombara, J. S., 1991, "Convective Heat Transfer by Impingement of Circular Liquid Jets," *Journal of Heat Transfer*, Vol. 113, pp. 571 - 582.

Mills, A. F., 1981, Lecture notes on convective heat transfer, UCLA.

Moffat, R. J., and Kays, W. M., 1984, "A Review of Turbulent-Boundary-Layer Heat Transfer Research at Stanford, 1958-1983," *Advances in Heat Transfer*, Vol. 16, pp. 241 - 365.

Nakoryakov, V. E., Pokusaev, B. G., and Troyan, E. N., 1978, "Impingement of an Axisymmetric Liquid Jet on a Barrier," *Int. J. Heat Mass Transfer*, Vol. 21, pp. 1175 - 1184.

Nikuradse, J., 1933, "Laws of Flow in Rough Pipes," *VDI Forschungsheft*, No. 361, Series B, Vol. 4, NACA TM 1292 (1950).

Nunner, W., 1956, "Heat Transfer and Pressure Drop in Rough Tubes," *VDI Forschungsheft*, No. 455, Series B, Vol. 22, pp. 5 - 39, A. E. R. E. Library/Transactions 786 (1958)

Omega Engineers, Inc., 1987, *Omega Temperature Measurement Handbook*, 2nd ed., p. T-12.

Pan, Y., Stevens, J., and Webb, B. W., 1992, "Effect of Nozzle Configuration on Transport in the Stagnation Zone of Axisymmetric, Impinging Free-Surface Liquid Jets: Part 2 - Local Heat Transfer," *Journal of Heat Transfer*, Vol. 114, pp. 880 - 886.

Pimenta, M. M., 1975, "The Turbulent Boundary Layer: An Experimental Study of the Transport of Momentum and Heat with the Effect of Roughness," Ph. D. Dissertation, Mechanical Engineering Department, Stanford University.

Scaggs, W. F., Taylor, R. P. and Coleman, H. W., 1988, "Measurement and Prediction of Rough Wall Effects on Friction Factor - Uniform Roughness Results", *Journal of Fluids Engineering*, Vol. 110, pp. 385 - 391.

Schlichting, 1979, *Boundary Layer Theory*, 7th ed., McGraw-Hill, NY.

Schlichting, H., 1936, "Experimental Investigation of the Problem of Surface Roughness," *Ingenieur-Archiv.*, Vol. 7, No. 1, pp. 1 - 34, NACA TM 832.

Stevens, J., Pan, Y., and Webb, B. W., 1992, "Effect of Nozzle Configuration on Transport in the Stagnation Zone of Axisymmetric, Impinging Free-Surface Liquid Jets: Part 1 - Turbulent Flow Structure," *Journal of Heat Transfer*, Vol. 114, pp. 874 - 879.

Stevens, J., and Webb, B. W., 1991, "Local Heat Transfer Coefficients Under an Axisymmetric, Single-Phase Liquid Jet," *Journal of Heat Transfer*, Vol. 113, pp. 71 - 78.

Sullivan, P. F., 1991, "Extended Surfaces for Use with Single Phase Jet Impingement Cooling of Discrete Heat Sources," M. S. Thesis, Purdue University.

Sullivan, P. F., Ramadhyani, S., and Incropera, F. P., 1992, "Use of Smooth and Roughened Spreader Plates to Enhance Impingement

Cooling of Small Heat Sources with Single Circular Liquid Jets", Session on Direct and Indirect Cooling Techniques in Electronic Packaging, 28th ASME/AIChE National Heat Transfer Conference, San Diego.

Taylor, R. P., 1989, "Surface Roughness Measurements on Gas Turbine Blades," ASME paper 89-GT-285.

Trabold, T. A., and Obot, N. T., 1987, "Impingement Heat Transfer Within Arrays of Circular Jets: Part II - Effects of Crossflow in the Presence of Roughness Elements," *Journal of Turbomachinery*, Vol. 109, pp. 594 - 601.

Touloukian, Y. S., 1970, *Thermophysical Properties of Matter,* Vol. 1, pp. 1182 - 1183; Vol. 3, p. 120; Vol. 11, p. 94.

Vasista, V. K., 1989, "Experimental Study of the Hydrodynamics of an Impinging Liquid Jet," S. B. Thesis in Mechanical Engineering, M.I.T.

Wassel, A. T., and Mills, A. F., 1979, "Calculation of Variable Property Turbulent Friction and Heat Transfer in Rough Pipes," *Journal of Heat Transfer*, Vol. 101, pp. 463 - 474.

White, F. M., 1974, *Viscous Fluid Flow*, McGraw-Hill, NY.

APPENDIX A: CALIBRATION

A.1 FLOW RATE

Flow rates less than 5 gpm were measured with an Omega FL-75A rotameter, while the larger flow rates were measured with an Omega FL-75C rotameter. Flow rates on the FL - 75A could be accurately read to ±0.05 gpm, while the FL - 75C could be accurately read to ±0.25 gpm. Primary calibration of the meters was performed by measuring the time required for a given volume of water to pass through the flow loop. This procedure has an estimated accuracy of ±2.5% due to resolution of the volume and time measurements. Figure 43 is the resulting calibration curve for the FL-75A rotameter, with the calibration equation:

$$Q_b = -9.8325 \times 10^{-2} + 0.97869 Q_m \tag{43}$$

where Q_b is the measured flow rate in gpm and Q_m is the flow rate read from the rotameter in gpm. The calibration curve for the FL-75C rotameter is shown in Figure 44 and its corresponding calibration equation is:

$$Q_b = 1.1219 + 1.0279 Q_m \tag{44}$$

where both flow rate readings are again in gpm.

Performance of the rotameters was checked by calculating the jet velocity, u_j, from the pressure in the plenum for a wide range of flow

rates. As discussed in Gabour (1991), entrance and frictional effects need to be considered when converting the pressure read from the pressure gauge at the top of the plenum to the pressure at the exit of the nozzle. Applying the energy equation over this region yields:

$$\left(p_g + \rho g H\right) = \left(1 + K + f\frac{L}{d}\right)\left(\frac{1}{2}\rho u_f^2\right) \tag{45}$$

where p_g is the gauge pressure, H is the distance from the top of the plenum to the outlet of the nozzle, and K is the loss coefficient associated with a reentrant pipe. The loss coefficients for the nozzles employed in this study are K = 0.5, 0.5, and 0.63 for the 4.4, 6.0, and 9.0 mm nozzles, respectively (Blevins, 1984). The friction factor is defined by the Darcy-Weisbach equation:

$$f\frac{L}{d} = \frac{2gh_L}{u_f^2} \tag{46}$$

where gh_L is the energy loss. Combining Equations (45) and (46) gives:

$$gh_L = \frac{\left(p_g + \rho g H\right) - (1+K)\left(\frac{1}{2}\rho u_f^2\right)}{\rho} \tag{47}$$

We define a new Reynolds number such that

$$R_f = \left[\frac{2(gh_L)d^3}{\nu^2 L}\right]^{0.5} = \sqrt{f}\,\mathrm{Re}_d \tag{48}$$

From the Colebrook formula,

$$f = \frac{0.25}{\left[\log\left(\frac{k/d}{3.7} + \frac{2.51}{R_f}\right)\right]} \tag{49}$$

which corrects a typographical error in Gabour (1991). For the smooth pipes used in this study, $k/d = 0$. Finally, this value for f is used in Equation (45) to determine the velocity by successive approximation. The flow rate is determined from the velocity and agreed with the rotameter readings to within ±3%.

A.2 TEMPERATURE

An Omega DP651 three-wire platinum resistance thermometer was used to monitor the temperature of the water in the plenum. It was carefully calibrated by comparison to a mercury-in-glass thermometer, and the resulting calibration curve is shown in Figure 45, with the following calibration equation:

$$T_{TH} = 0.10408 + 0.99419 T_{PRT} + 2.5323 \times 10^{-4} T_{PRT}^2 \tag{50}$$

where T_{TH} is the temperature reading of the thermometer and T_{PRT} is the corresponding platinum resistance thermometer reading. Both temperatures are read in degrees Celsius.

Thermocouple voltage is converted to temperature by:

$$T_{TC} = -0.48868252 + 19{,}873.14503x - 218{,}614.5353x^2 + 11{,}569{,}199.78x^3 - 264{,}917{,}531.4x^4 + 2{,}018{,}441{,}314x^5 \quad (51)$$

where T_{TC} is temperature in degrees Celsius and x is the thermocouple voltage in volts. Voltage readings from the three thermocouples were converted to temperature and the temperatures were averaged to obtain one value. The thermocouples were calibrated under the same conditions as the platinum resistance thermometer and their calibration curve is shown in Figure 46. The resulting calibration equation is:

$$T_{TH} = 6.4419 \times 10^{-2} + 0.99491 T_{TC} + 2.9139 \times 10^{-4} T_{TC}^2 \quad (52)$$

where both temperatures are measured in degrees Celsius.

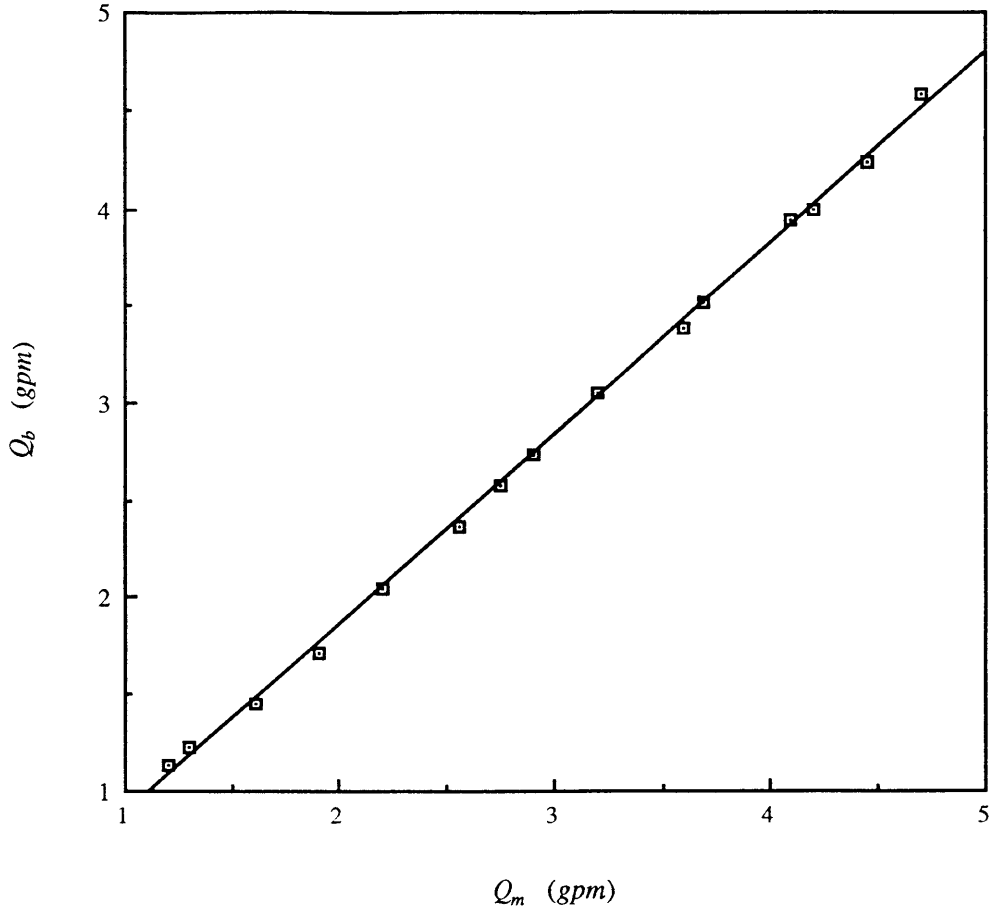

Figure 43: Calibration curve for Omega FL - 75A rotameter;
1 gpm = 6.3091 x 10^{-5} m^3/s.

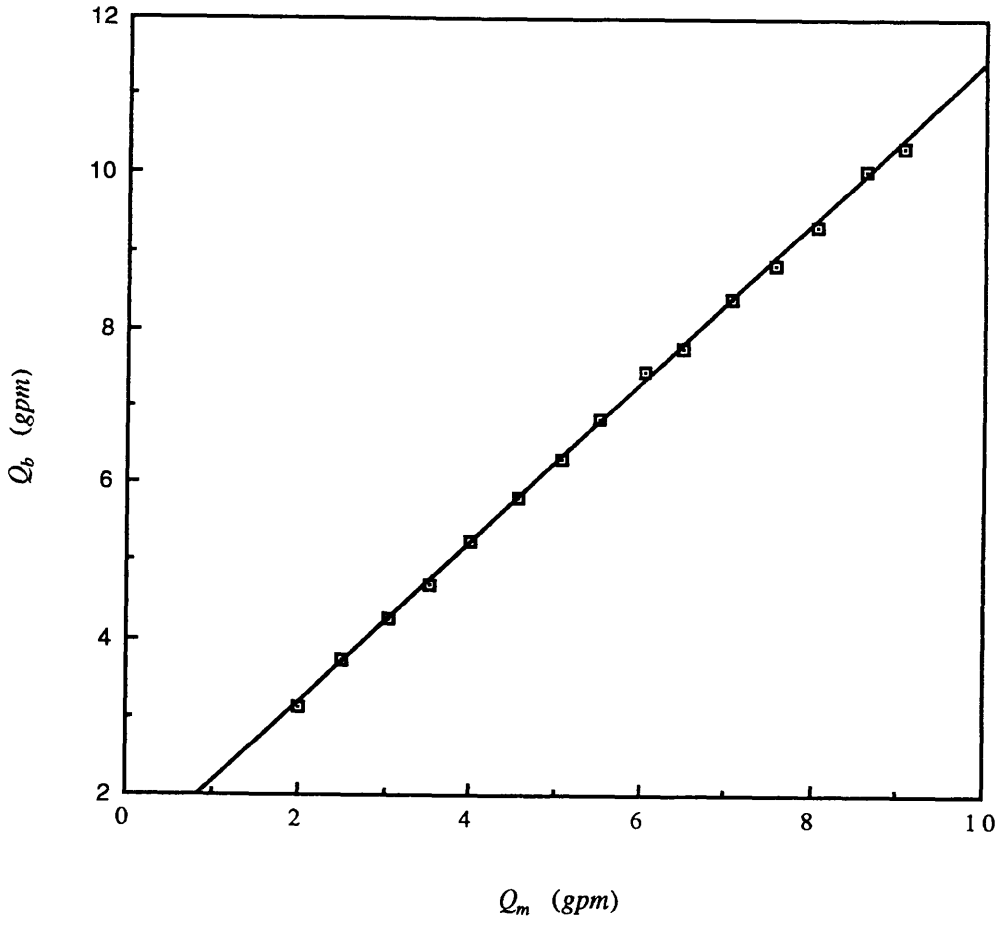

Figure 44: Calibration curve for Omega FL - 75C rotameter;
1 gpm = 6.3091 x 10^{-5} m^3/s.

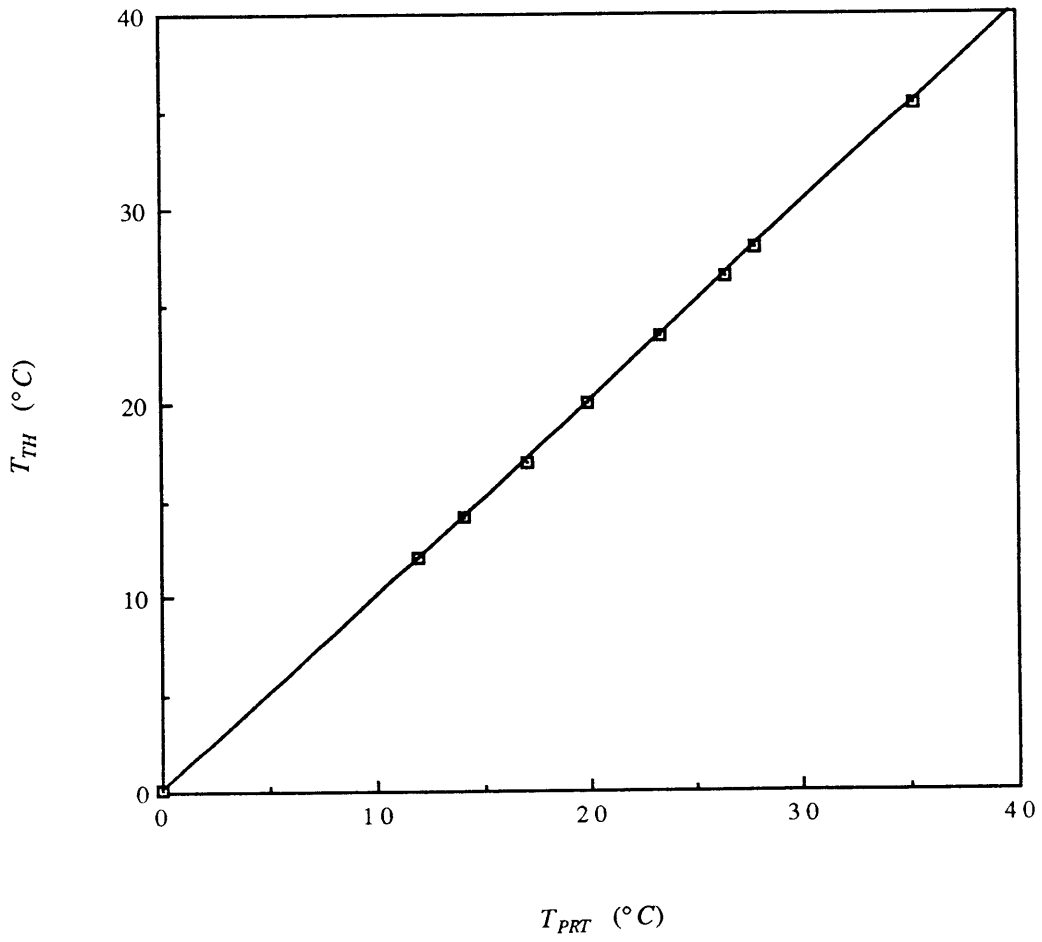

Figure 45: Calibration curve for the platinum resistance thermometer.

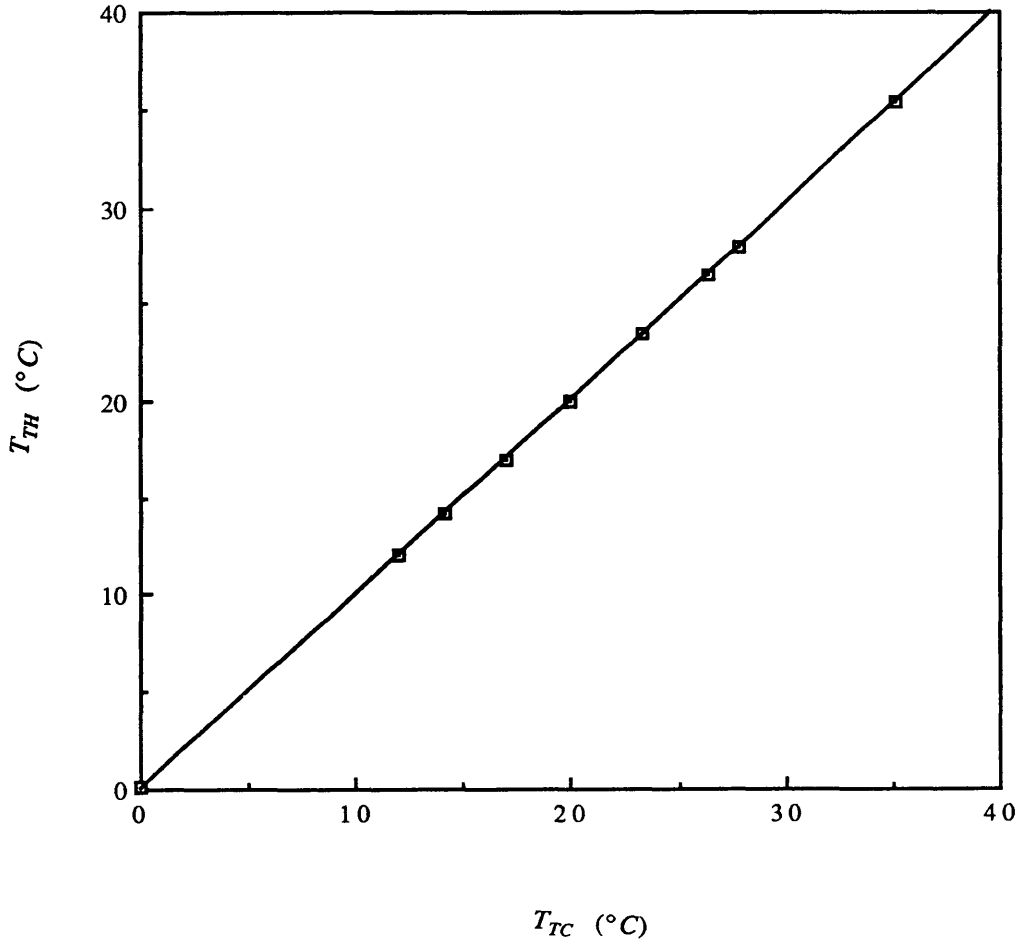

Figure 46: Calibration curve for the thermocouples.

APPENDIX B: UNCERTAINTY ESTIMATES

Experimental uncertainties are based on 95 percent confidence levels. Using Equation (27), uncertainty in the measured value of the Nusselt number is calculated from:

$$\left(\frac{u_{\mathrm{Nu}_m}}{\mathrm{Nu}_m}\right)^2 = \left(\frac{u_{q_w}}{q_w}\right)^2 + \left(\frac{u_{d_j}}{d_j}\right)^2 + \left(\frac{u_{k_f}}{k_f}\right)^2 + \left(\frac{u_{\Delta T}}{\Delta T}\right)^2 \tag{53}$$

where

$$\left(\frac{u_{q_w}}{q_w}\right)^2 = \left(\frac{u_R}{R}\right)^2 + \left(\frac{2u_I}{I}\right)^2 + \left(\frac{u_{l_h}}{l_h}\right)^2 + \left(\frac{u_{w_h}}{w_h}\right)^2 \tag{54}$$

Uncertainty in the resistance of the heater sheet is ±0.5%. The length and width of the heater have uncertainties of ±1.7% and ±3.3%, respectively. Uncertainty in the current is calculated for each heat flux used, and was always less than ±1%. Jet diameters were measured with precision calipers and have uncertainties of ±0.2%, ±0.7%, and ±0.5% for the 4.4, 6.0, and 9.0 mm nozzles, respectively. Uncertainty in the thermal conductivity of water is based on errors resulting from linear interpolation of tabulated data, and is estimated at ±0.6%. Uncertainty in ΔT is ±0.08°C.

From Equation (28), uncertainty in the true Nusselt number is calculated from:

$$\left(\frac{u_{\mathrm{Nu}_d}}{\mathrm{Nu}_d}\right)^2 = \left(\frac{u_\zeta}{\zeta}\right)^2 \left(\frac{\mathrm{Nu}_d}{2}\right)^2 \zeta^2 + \left(\frac{u_{\mathrm{Nu}_m}}{\mathrm{Nu}_m}\right)^2 \left(1 + \frac{\mathrm{Nu}_d \zeta}{2}\right)^2 \tag{55}$$

where

$$\left(\frac{u_\zeta}{\zeta}\right)^2 = \left(\frac{u_t}{t}\right)^2 + \left(\frac{u_{k_f}}{k_f}\right)^2 + \left(\frac{u_{k_w}}{k_w}\right)^2 + \left(\frac{u_{d_j}}{d_j}\right)^2 \tag{56}$$

from Equation (29).

The thickness of the heater sheet was measured with a micrometer and has an uncertainty of ±3%. Two sets of tabulated data on thermal conductivity of 1010 steel were compared (American Society for Metals, 1983; Touloukian, 1970), giving an uncertainty in the wall conductivity of ±2%, which accounts for linearly interpolating values. Uncertainty in ζ was calculated for each data point, and was always less than ±3.7%, resulting in a maximum uncertainty in the Nusselt number of ±10%.

Uncertainty in the Reynolds number is determined by:

$$\left(\frac{u_{\mathrm{Re}_d}}{\mathrm{Re}_d}\right)^2 = \left(\frac{u_Q}{Q}\right)^2 + \left(\frac{u_d}{d}\right)^2 + \left(\frac{u_\nu}{\nu}\right)^2 \tag{57}$$

Uncertainty in the volumetric flow rate reached a maximum of ±3.2%. Uncertainty in the kinematic viscosity was estimated at 3.6% to account for errors from linearly interpolating tabulated data. This resulted in an uncertainty of less than ±5% in the Reynolds number.

The RMS roughness height, k, was calculated by averaging the squared RMS values, k^2, where we calculate uncertainty in k^2 from:

$$u_{k^2} = \sqrt{u_{B_{k^2}}^2 + u_{P_{k^2}}^2} \tag{58}$$

where $u_{B_{k^2}}$ is a bias uncertainty based on the calibration uncertainty of the DEKTAK and $u_{P_{k^2}}$ is the precision uncertainty of the measurement. Assuming a Gaussian distribution of the errors in successive measurements of k^2 and using a t-statistic with a two sided 95% confidence interval due to the small sample size, the precision uncertainty is calculated from:

$$u_{P_{k^2}} = t_{0.025,9} \frac{S_{k^2}}{\sqrt{10}} \tag{59}$$

where S_{k^2} is the standard deviation of the measured k^2 values and $t_{0.025,9}$= 2.262. Compared to the precision uncertainty, the bias uncertainty was negligible. This resulted in uncertainties in the RMS heights ranging from ±4.5 - ±9%.

APPENDIX C: EXPERIMENTAL DATA

Re_d	Nu_d
27320	361.72
35035	418.26
39950	457.19
45365	495.93
48230	513.72
53120	545.16
56190	565.16
59920	598.69
63630	617.69
65960	638.47

Table 2: Surface S1, smooth, d_j = 4.4 mm.

Re_d	Nu_d
28140	368.52
35895	434.39
40675	474.75
46590	516.32
48925	533.56
53225	561.67
56905	586.80
60690	616.72
63850	647.30
66865	668.55

Table 3: Surface S2, k = 4.7μm, d_j = 4.4 mm.

Re_d	Nu_d
28415	366.24
35325	426.62
40255	467.76
45365	514.79
48525	533.77
53555	569.30
56595	595.69
60205	631.82
62935	656.03
66210	677.43

Table 4: Surface S3, k=6.3μm, d_j = 4.4 mm.

Re_d	Nu_d
27795	355.47
35485	425.45
40670	465.32
45785	514.56
48355	548.87
53715	589.98
56895	619.05
60690	653.04
63490	684.18
66985	709.85

Table 5: Surface S4, k=8.6μm, d_j = 4.4 mm.

Re_d	Nu_d
27715	367.33
35250	440.76
40035	493.07
45335	552.89
48755	589.41
53750	645.43
56750	669.63
60260	709.96
63790	751.18
66895	774.11

Table 6: Surface S5, k=13.1μm, d_j = 4.4 mm.

Re_d	Nu_d
27690	377.90
35525	457.44
40145	510.23
45405	569.66
48315	590.68
53230	647.96
56345	680.11
60040	716.78
62430	747.74
65805	776.58

Table 7: Surface S6, k=14.1μm, d_j = 4.4 mm.

Re_d	Nu_d
27560	393.60
35725	482.36
40630	557.12
45585	612.66
48690	653.21
53750	712.75
57125	752.63
60570	790.79
63275	825.65
66450	843.87

Table 8: Surface S7, k=20.1μm, d_j = 4.4 mm.

Re_d	Nu_d
28605	421.45
34975	500.48
40570	579.75
45395	641.66
48445	683.02
53410	730.08
56455	773.76
60125	817.63
63160	831.54
66450	871.14

Table 9: Surface S8, k=25.9μm, d_j = 4.4 mm.

Re_d	Nu_d
29040	441.37
35110	505.63
40675	588.21
45870	646.02
48890	683.48
53665	737.48
56955	793.47
60610	823.03
63500	864.80
66760	887.79

Table 10: Surface S9, k=26.5μm, d_j = 4.4 mm.

Re_d	Nu_d
30035	472.77
36390	553.75
41745	625.32
47055	700.18
50130	735.70
54895	794.51
57685	822.22
61415	865.19
63790	894.93
67350	941.64

Table 11: Surface S10, k=28.2μm, d_j = 4.4 mm.

Re_d	Nu_d
33380	408.88
42915	472.38
49745	522.84
57240	568.86
63895	608.20
68020	638.51
72090	671.53
76170	698.90
80345	718.32
83850	743.56

Table 12: Surface S1, smooth, d_j = 6.0 mm.

Re_d	Nu_d
20735	330.89
30925	393.85
39175	452.46
45770	500.81
52285	542.47
59335	593.88
63475	629.62
67760	653.34
72545	683.97
75510	708.86
79230	741.18

Table 13: Surface S2, k=4.7μm, d_j = 6.0 mm.

Re_d	Nu_d
33110	407.27
41790	474.52
48675	529.44
54370	575.83
61295	615.06
67410	669.36
70900	695.61
75095	719.85
78695	753.40

Table 14: Surface S3, k=6.3μm, d_j = 6.0 mm.

Re_d	Nu_d
20240	324.85
33420	418.12
42260	482.85
48085	541.46
55530	593.26
61795	641.31
67055	682.32
70405	713.78
74775	748.99
78395	779.78
82630	809.71

Table 15: Surface S4, k=8.6μm, d_j = 6.0 mm.

Re_d	Nu_d
34275	436.70
43300	514.73
50545	579.24
56025	635.19
63430	696.45
68830	746.25
72220	779.05
76455	811.94
80475	848.05
83650	873.23

Table 16: Surface S5, k=13.1μm, d_j = 6.0 mm.

Re_d	Nu_d
21560	325.85
32440	429.39
40175	498.97
48105	566.82
53260	620.50
61255	692.51
65115	725.68
69385	764.95
74525	806.63
77990	836.80
81165	868.07
84255	887.68

Table 17: Surface S6, k=14.1μm, d_j = 6.0 mm.

Re_d	Nu_d
34785	472.67
44435	559.25
50780	630.37
54980	688.13
60835	741.82
66610	792.10
70170	829.46
73725	859.95
77300	888.32
81940	922.22

Table 18: Surface S7, k=20.1μm, d_j = 6.0 mm.

Re_d	Nu_d
27370	405.44
36260	496.13
42820	575.02
48040	624.60
53620	691.11
59310	750.56
64380	804.88
67530	833.26
70960	861.15
73560	885.22
74540	901.34
77550	930.30
82800	966.93

Table 19: Surface S8, k=25.9μm, d_j = 6.0 mm.

Re_d	Nu_d
20415	361.61
31225	463.46
40325	557.90
46845	622.38
53420	693.19
58905	741.70
63890	800.38
68140	846.06
71560	888.84
77080	944.64
81830	985.24

Table 20: Surface S9, k=26.5μm, d_j = 6.0 mm.

Re_d	Nu_d
33800	510.19
41415	607.92
47860	658.39
54290	731.71
61385	791.74
66630	852.87
71035	908.83
75060	936.86
78790	974.93
82310	999.12

Table 21: Surface S10, k=28.2μm, d_j = 6.0 mm.

Re_d	Nu_d
26755	365.96
33935	418.60
41760	476.70
47675	516.46
50955	543.16
59610	590.98
64630	632.27
69425	657.54

Table 22: Surface S1, smooth, d_j = 9.0 mm.

Re_d	Nu_d
27925	373.38
38300	449.80
46595	505.94
55100	565.96
59685	591.43
66760	638.93
72615	675.23
78565	711.50

Table 23: Surface S2, k=4.7μm, d_j = 9.0 mm.

Re_d	Nu_d
26770	364.93
33820	416.99
40565	469.38
47570	527.95
50955	543.80
59310	597.37
63675	622.46
69170	665.63

Table 24: Surface S3, k=6.3μm, d_j = 9.0 mm.

Re_d	Nu_d
29620	391.86
39040	460.96
45770	511.77
54855	57615
58620	604.93
67995	673.53
76000	722.99

Table 25: Surface S4, k=8.6μm, d_j = 9.0 mm.

Re_d	Nu_d
29455	394.72
38090	459.07
45730	524.01
53935	583.51
58970	626.59
68285	697.54
74030	738.71
79500	774.99

Table 26: Surface S5, k=13.1μm, d_j = 9.0 mm.

Re_d	Nu_d
26620	371.16
34205	428.60
39885	476.14
48460	546.67
51590	573.34
59210	636.30
64160	675.85
69335	715.52

Table 27: Surface S6, k=14.1μm, d_j = 9.0 mm.

Re_d	Nu_d
26455	370.14
33670	433.53
40505	499.19
47215	557.79
50520	598.91
58700	666.91
66240	731.38
69705	752.97

Table 28: Surface S7, k=20.1μm, d_j = 9.0 mm.

Re_d	Nu_d
28940	393.26
37895	477.36
45975	561.71
53935	641.32
59045	681.92
68525	770.77
73960	815.75
79155	861.72

Table 29: Surface S8, k=25.9μm, d_j = 9.0 mm.

Re_d	Nu_d
30225	419.66
38870	488.42
46670	566.00
54975	647.06
60775	703.51
68160	770.86
74620	834.77
80065	873.62

Table 30: Surface S9, k=26.5μm, d_j = 9.0 mm.

Re_d	Nu_d
27050	397.22
34330	461.31
40725	531.37
48730	613.67
52195	642.80
60315	720.17
64660	755.05
71015	824.37

Table 31: Surface S10, k=28.2μm, d_j = 9.0 mm.